

UNIVERSIDADE ESTADUAL DE PONTA GROSSA
SETOR DE CIÊNCIAS EXATAS E NATURAIS
PROGRAMA DE PÓS-GRADUAÇÃO EM CIÊNCIAS

MATHEUS ROLIM SALES

DYNAMICAL ASPECTS OF HAMILTONIAN SYSTEMS: CHAOS, STICKINESS, AND
RECURRENCE PLOTS
ASPECTOS DINÂMICOS DE SISTEMAS HAMILTONIANOS: CAOS, *STICKINESS*, E
GRÁFICOS DE RECORRÊNCIA

PONTA GROSSA
2023

MATHEUS ROLIM SALES

DYNAMICAL ASPECTS OF HAMILTONIAN SYSTEMS: CHAOS, STICKINESS, AND
RECURRENCE PLOTS
ASPECTOS DINÂMICOS DE SISTEMAS HAMILTONIANOS: CAOS, *STICKINESS*, E
GRÁFICOS DE RECORRÊNCIA

Thesis presented to the Graduate Program in Sciences, concentration area Physics, of the Universidade Estadual de Ponta Grossa, in partial fulfillment of the requirements for the degree of Doctor in Science.

Advisor: Prof. Dr. José Danilo Szezech Junior

PONTA GROSSA
2023

S163 Sales, Matheus Rolim
Dynamical aspects of Hamiltonian systems: chaos, stickiness, and recurrence plots / Matheus Rolim Sales. Ponta Grossa, 2023.
115 f.

Tese (Doutorado em Ciências - Área de Concentração: Física), Universidade Estadual de Ponta Grossa.

Orientador: Prof. Dr. José Danilo Szezech Junior.

1. Quasi-integrable hamiltonian systems. 2. Stickiness effect. 3. Weighted birkhoff average. 4. Recurrence plots. 5. Recurrence time entropy. I. Szezech Junior, José Danilo. II. Universidade Estadual de Ponta Grossa. Física. III.T.

CDD: 530.1

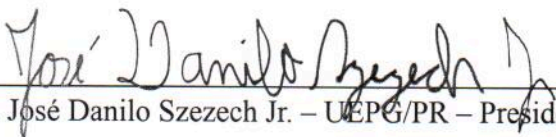
TERMO DE APROVAÇÃO

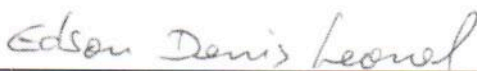
MATHEUS ROLIM SALES

DYNAMICAL ASPECTS OF HAMILTONIAN SYSTEMS: CHAOS, STICKINESS AND
RECURRENCE PLOTS

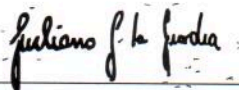
Tese aprovada como requisito parcial para obtenção do grau de Doutor em Ciências, no Programa de Pós-Graduação em Ciências, Área de Concentração Física, da Universidade Estadual de Ponta Grossa, pela seguinte banca examinadora:

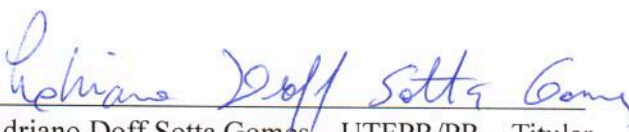
Orientador


Dr. José Danilo Szezech Jr. – UEPG/PR – Presidente


Dr. Edson Denis Leonel – UNESP/SP – Titular


Dr. Silvo Luiz Thomaz de Souza – UFSJ/MG – Titular


Dr. Giuliano Gadioli La Guardia – UEPG/PR – Titular


Dr. Adriano Doff Sotta Gomes – UTFPR/PR – Titular

Ponta Grossa, 23 de outubro de 2023.

ACKNOWLEDGEMENTS

First and foremost, I wish to express my deepest gratitude to my mother, whose love, care, dedication, and unconditional support have shaped the 28 years of my life. Without her, I would not have gotten this far or become the person I am today.

Secondly, I would like to share a story. In our field, we often talk about sensitivity to initial conditions, popularly known as the butterfly effect. By the end of 2019, I found myself at a crossroads, deciding whether to continue with my academic career or not. It was when I casually suggested to Prof. Fabio, my then-advisor, that Prof. José Danilo be present on my Master's examination committee that my future began to take shape. After the defense, Prof. Danilo informed me about the possibility of a doctoral scholarship at the Universidade Estadual de Ponta Grossa (UEPG), and he expressed his willingness to be my supervisor if the scholarship were approved. I want to express my deep gratitude to Prof. Danilo for the invitation to be my advisor. I also thank him for his excellent guidance, for always finding time to address my doubts, for his patience, and for the pieces of advice and encouragement that I will carry throughout my entire academic career.

At UEPG, I was warmly welcomed by the 105 Group Science, where I found a community that went beyond the academic environment. I would like to thank all the members of the group for the conversations, companionship, and support. In particular, I want to thank Diogo Ricardo Costa for the assistance during the early stages of my doctoral research, and for sharing the codes that enabled the progress of my research.

To my friends, especially Alysson, Ivonete, and Marcos Eduardo, I want to express my gratitude for the conversations and advice, for the moments of relaxation, and for the support during this long journey that began in 2013.

To Bárbara, I thank you for showing up in my life at such an important moment and for being a little bit of order in this chaotic world. Your presence has made everything lighter and easier to bear, and for that, I am immensely grateful.

I cannot forget to thank Serhiy Yanchuk and Jürgen Kurths for graciously hosting me during my doctoral period in Germany. Each piece of knowledge shared during this short but invaluable time broadened my academic horizons. I would also like to express my gratitude to Humboldt-Universität zu Berlin and to Potsdam-Institut für Klimafolgenforschung, as well as all their members, whether researchers or administrative staff.

Last but by no means least, I thank the Coordination of Superior Level Staff Improvement (CAPES) for the financial support that made this research possible, both in Brazil, process number 88887.485462/2020-00, and abroad, through the *Programa de Doutorado Sanduíche no Exterior*, process number 88881.689932/2022-01.

Teach the ignorant as much as you can; society is culpable in not providing a free education for all and it must answer for the night which it produces. If the soul is left in darkness, sins will be committed. The guilty one is not he who commits the sin, but he who causes the darkness.

Victor Hugo

ABSTRACT

Hamiltonian systems represent a vast class of dynamical systems that have the special feature of preserving volume in phase space. The phase space of a typical Hamiltonian system is neither integrable nor uniformly hyperbolic. It exhibits both regular and chaotic components. For two-dimensional quasi-integrable systems with a hierarchical phase space, chaotic orbits can spend an arbitrarily long time around islands of stability, in which they behave similarly to quasiperiodic orbits. This phenomenon is called stickiness and is one of the main consequences of the complex hierarchical structure of islands-around-islands embedded in the chaotic sea. Stickiness affects the global transport properties of the system and the convergence of the Lyapunov exponents. In this thesis, we analyze nonstandard dynamical measures for the quantification of chaotic motion and the detection of the stickiness effect in Hamiltonian systems. Initially, we consider the standard map, which is a simple, paradigmatic system that displays all the features of quasi-integrable Hamiltonian systems. First, we introduce a recently proposed dynamical measure based on ergodic theory and a weighted Birkhoff average. By using this measure, we successfully distinguish chaos and regularity for different values of the standard map's non-linearity parameter k , and we apply it together with the uncertainty fraction method to determine the fractal dimension of the islands' boundary for a special value of k , namely, $k = 6.908745$. For this value, the standard map's phase space is composed of a self-similar hierarchical structure of islands within the chaotic sea, and we show that the deeper we go into this structure, the longer it takes for the orbits to escape the trapping region, and the higher the boundary dimension becomes. Additionally, the dimension depends on the position in phase space as well as on the scale of the initial condition uncertainty, which implies the existence of an effective fractal dimension. As a further measure, we propose the use of an entropy-based measure of the recurrence plots (RPs). We estimate the recurrence times of an orbit from the RP and calculate the Shannon entropy of its distribution, known as the recurrence time entropy (RTE). We find that the RTE is an alternative way of detecting chaotic orbits and sticky regions. We show that the largest Lyapunov exponent and the RTE exhibit a high correlation coefficient even when considering relatively small time series (5000 data points). By computing the RTE in smaller time windows along the evolution of a single chaotic orbit, we find the finite-time RTE distribution to be multi-modal when sticky regions are present in phase space, and we successfully identify the specific areas in phase space that correspond to each mode. We also quantify the duration of each stickiness regime and find that the cumulative distribution of trapping times in the sticky regions follows a power law tail, while the distribution when the orbit wanders in the chaotic sea displays an exponential decay. Seeking a more robust analysis of the aforementioned dynamical measures, we consider another two-dimensional Hamiltonian system with a hierarchical divided phase space: the billiard system. We demonstrate that these measures characterize all dynamical behavior of such a system, with the advantage of not relying on the Jacobian matrix for their calculation, unlike the Lyapunov exponents.

Keywords: quasi-integrable Hamiltonian systems, stickiness effect, weighted Birkhoff average, recurrence plots, recurrence time entropy.

RESUMO

Sistemas Hamiltonianos representam uma vasta classe de sistemas dinâmicos que possuem a característica especial de preservar o volume no espaço de fase. O espaço de fase de um típico sistema Hamiltoniano não é integrável nem uniformemente hiperbólico. Ele exibe componentes tanto regulares quanto caóticas. Para sistemas bidimensionais quase-integráveis com um espaço de fase hierárquico, órbitas caóticas podem passar um tempo arbitrariamente longo ao redor de ilhas de estabilidade, nas quais se comportam de maneira similar a órbitas quase-periódicas. Esse fenômeno é chamado de “stickiness” e é uma das principais consequências da complexa estrutura hierárquica de ilhas ao redor de ilhas no mar caótico. O *stickiness* afeta as propriedades globais de transporte do sistema e a convergência dos expoentes de Lyapunov. Nesta tese, analisamos medidas dinâmicas alternativas para a quantificação do movimento caótico e a detecção do efeito de *stickiness* em sistemas Hamiltonianos. Inicialmente, consideramos o mapa padrão, que é um sistema simples e paradigmático que exibe todas as características de sistemas Hamiltonianos quase-integráveis. Primeiro, introduzimos uma medida dinâmica proposta recentemente baseada na teoria ergódica e uma média ponderada de Birkhoff. Ao usar essa medida, distinguimos com sucesso caos e regularidade para diferentes valores do parâmetro de não linearidade k do mapa padrão, e aplicamos essa medida em conjunto com o método de fração de incerteza para determinar a dimensão fractal da fronteira das ilhas para um valor especial de k , a saber, $k = 6.908745$. Para esse valor, o espaço de fase do mapa padrão é composto por uma estrutura hierárquica auto-similar de ilhas dentro do mar caótico, e mostramos que quanto mais fundo entramos nessa estrutura, mais tempo leva para as órbitas escaparem da região de aprisionamento, e maior se torna a dimensão da fronteira. Além disso, a dimensão depende da posição no espaço de fase, bem como da escala da incerteza da condição inicial, o que implica na existência de uma dimensão fractal efetiva. Como medida adicional, propomos o uso de uma medida baseada na entropia dos plots de recorrência (RPs). Estimamos os tempos de recorrência de uma órbita a partir do RP e calculamos a entropia de Shannon de sua distribuição, conhecida como entropia dos tempos de recorrência (RTE). Descobrimos que a RTE é uma maneira alternativa de detectar órbitas caóticas e regiões de *stickiness*. Mostramos que o maior expoente de Lyapunov e a RTE exibem um coeficiente de correlação elevado, mesmo ao considerar séries temporais relativamente pequenas (5000 pontos). Ao calcular a RTE em janelas de tempo menores ao longo da evolução de uma única órbita caótica, descobrimos que a distribuição da RTE a tempo finito possui vários modos quando regiões de *stickiness* estão presentes no espaço de fase, e identificamos, com sucesso, as regiões específicas no espaço de fase que correspondem a cada modo. Também quantificamos a duração de cada regime de *stickiness* e descobrimos que a distribuição cumulativa de tempos de aprisionamento nas regiões de *stickiness* exibe uma cauda de lei de potência, enquanto a distribuição quando a órbita vagueia no mar caótico exibe um decaimento exponencial. Procurando-se uma análise mais robusta das medidas dinâmicas mencionadas anteriormente, consideramos outro sistema Hamiltoniano bidimensional com um espaço de fase hierárquico: o sistema de bilhar. Verificamos que essas medidas caracterizam todo o comportamento dinâmico de tal sistema, com a vantagem de não dependerem da matriz Jacobiana para o seu cálculo, ao contrário dos expoentes de Lyapunov.

Palavras-chave: sistemas Hamiltonianos quase-integráveis, efeito de *stickiness*, média ponderada de Birkhoff, gráficos de recorrência, entropia dos tempos de recorrência.

LIST OF FIGURES

Figure 2.1 – Time evolution of the phase space volume Γ_1 to Γ_2 . Liouville’s theorem states that $\Gamma_1 = \Gamma_2 = \text{const.}$	23
Figure 2.2 – Schematic representation of a two-dimensional <i>torus</i>	26
Figure 2.3 – Time evolution of a trajectory in phase space and its successive intersection with the Poincaré section Ω	31
Figure 2.4 – The neighborhood of a resonant <i>torus</i> . (a) Illustration of an integrable system, where the middle curve represents the rational <i>torus</i> with rotation number $\nu = r/s$ ($s = 2$ in this illustration). The inner and outer curves represent the irrational <i>tori</i> . (b) Illustration of the perturbed system. The intersections between the dashed and full lines are the fixed points of the s -fold iterated Poincaré map. The inner and outer curves represent the irrational <i>tori</i> that survive the perturbation.	33
Figure 2.5 – Neighborhood of an elliptic point (on the left) and a hyperbolic point (on the right). The orbits that circle about the elliptic point in elliptical trajectories are called elliptical orbits. The thinner lines in the figure on the right represent hyperbolic orbits that move away from the hyperbolic point in all directions. The thicker lines are the asymptotes (stable and unstable directions) of the hyperbolic point.	34
Figure 2.6 – Schematic representation of the phase space of a two-dimensional Hamiltonian system, where the chaotic sea is depicted in gray and the regular island in white. Within this island, there exist KAM <i>tori</i> , and surrounding the island are the remnants of a destroyed KAM <i>torus</i> , known as the <i>cantorus</i>	35
Figure 3.1 – The phase space of the standard map for 100 randomly chosen initial conditions iterated for $N = 1.5 \times 10^4$ times with (a) $k = 0.0$, (b) $k = 0.9$, (c) $k = 1.5$, (d) $k = 3.63$, (e) $k = 5.3$, and (f) $k = 9.0$	37
Figure 3.2 – Temporal evolution of a two-dimensional sphere of initial conditions around the point \mathbf{x}_0 , where $\epsilon_i(t)$ denotes the length of its i th axis at time t	40
Figure 3.3 – The Lyapunov exponents time series of the standard map (3.3) with $k = 1.5$ and initial condition $(\theta_0, p_0) = (3.0, 0.0)$. In blue is the largest Lyapunov exponent, λ_1 , and in red the smallest Lyapunov exponent, λ_2 . As has been stated in the text, due preservation of phase space volume, the sum of all Lyapunov exponents must be zero, which is verified by the black curve, $\lambda_1 + \lambda_2$	43

- Figure 3.4 – The phase space and the largest Lyapunov exponent time series of the standard map with (a) $k = 0.9$ and initial conditions (black) $(\theta_0, p_0) = (3.0, 0.0)$, (red) $(\theta_0, p_0) = (\pi, -\pi/2 - 0.12)$, (blue) $(\theta_0, p_0) = (\pi, -2.55)$, and (green) $(\theta_0, p_0) = (\pi, \pi/2 + 0.11)$, and with (b) $k = 1.5$ and initial conditions (black) $(\theta_0, p_0) = (3.0, 0.0)$, (red) $(\theta_0, p_0) = (2.87, 0.0)$, (blue) $(\theta_0, p_0) = (-\pi, -2.0)$, and (green) $(\theta_0, p_0) = (3\pi/2, -\pi)$ 43
- Figure 3.5 – (a) The FTLE “time series” and (b) the FTLE probability distribution of the standard map with $k = 1.5$ and initial conditions (black) $(\theta_0, p_0) = (3.0, 0.0)$, (red) $(\theta_0, p_0) = (2.87, 0.0)$, (blue) $(\theta_0, p_0) = (-\pi, -2.0)$, and (green) $(\theta_0, p_0) = (3\pi/2, -\pi)$ 44
- Figure 3.6 – (a) The phase space and (b) the largest Lyapunov exponent time series of the standard map for $k = 1.5$ and $T = 2 \times 10^6$ with initial condition (red) $(\theta_0, p_0) = (3.0, 0.0)$, (blue) $(\theta_0, p_0) = (0.0, 0.0)$, (green) $(\theta_0, p_0) = (0.25, 0.0)$, (purple) $(\theta_0, p_0) = (0.5, 0.0)$, (yellow) $(\theta_0, p_0) = (0.75, 0.0)$, and (cyan) $(\theta_0, p_0) = (1.25, 0.0)$. The convergence rate of λ_1 towards zero is different for different initial conditions, where the fastest convergence rate is for the fixed point itself (red curve). 45
- Figure 3.7 – The largest Lyapunov exponent for a 1000×1000 grid of uniformly chosen values of (a) (k, θ_0) with $p_0 = 0$, and (b) (k, p_0) with $\theta_0 = 0$ and $T = 1.0 \times 10^4$. 45
- Figure 3.8 – The diffusion coefficient, Eq. (3.45), for the standard map as a function of the nonlinearity parameter, with $\Delta k = 0.025$ for (green) $n = 1.0 \times 10^3$, (blue) $n = 5.0 \times 10^3$, and (red) $n = 1.0 \times 10^4$. In black dashed line is the theoretical value for the standard map as predicted in (3.44). We considered 100×100 initial conditions uniformly distributed in a grid on the entire phase space $[0, 2\pi] \times [0, 2\pi]$. Inset: magnification on the interval $k \in [6, 8]$ that shows the groups II and III of accelerator mode islands. We observe a deviation of the numerically calculated diffusion coefficient from its theoretical value. 51
- Figure 3.9 – The variance of the momentum, $\langle (p - p_0)^2 \rangle$, as a function of the number of iterations n for (red) $k = 6.0$, (blue) $k = 6.25$, (green) $k = 6.5$, (cyan) $k = 6.625$, (brown) $k = 6.75$, and (yellow) $k = 7.0$. The black dashed (dotted) line indicates the slope of $\mu = 1$ ($\mu = 2$). We considered 30×30 initial conditions uniformly distributed in a grid on the entire phase space $[0, 2\pi] \times [0, 2\pi]$ 52

Figure 4.1 – The number of zeros after the decimal point of the convergence of the weighted Birkhoff average, dig [Eq. (4.5)], for a grid of 1000×1000 uniformly distributed initial conditions in the phase space region depicted of the standard map (3.3), with (a) $k = 0.9$, (b) $k = 1.5$, (c) $k = 3.93$, (d) $k = 4.0$, (e) $k = 5.3$, and (f) $k = 6.908745$. The total iteration time is $2N = 2.0 \times 10^6$, and $h(\theta, p) = \cos \theta$. The regular regions are characterized by high values of dig (red), while the chaotic ones by small values of dig (blue).	56
Figure 4.2 – Histograms of the values of dig shown in Figure 4.1. There are mainly two peaks, each one characterizing one dynamical regime. The peak for small values of dig corresponds to chaotic orbits, while the peak for larger values of dig to regular orbits. There are orbits with an intermediate value of dig , and they are trapped orbits whose value of dig has yet not converged its asymptotic value. We note that as k increases, the proportion of regular orbits diminishes, as expected.	57
Figure 4.3 – The normalized proportion of regular orbits as a function of the cutoff value dig_c for the data in Figures 4.1 and 4.2. For small and large values of dig , the proportion changes significantly, however, there is an interval around $\text{dig}_c \in [5, 12]$ in which the proportion is almost constant.	57
Figure 4.4 – A region in phase space with two different final states, A and B, divided by the boundary. A and B can represent either two different attractors or the boundary of an island. Points 1 and 2 are initial conditions with uncertainty ϵ	58
Figure 4.5 – The uncertainty fraction as a function of ϵ for the phase space region depicted in Figure 4.1(d) with $k = 4.0$. We observe a power law dependence with exponent $\alpha = 0.371 \pm 0.009$. We chose 5.0×10^4 random initial conditions for each value of ϵ , and we performed this simulation ten times. We computed the uncertainty exponent for each one of the ten simulations and took its mean and standard deviation: $\alpha = \bar{\alpha} \pm \sigma_\alpha$	60
Figure 4.6 – The phase space of the standard map with $k = 6.908745$ for 100 randomly chosen initial conditions distributed (a) in the entire phase space $[-\pi, \pi] \times [-\pi, \pi]$ and (b)-(f) in the regions delimited by the first five rows of Table 4.1. Figures (b)-(f) are magnifications around the islands marked by a red box.	61
Figure 4.7 – The escape time for a grid of 1000×1000 uniformly distributed initial conditions in the regions given in Table 4.1 for the standard map with $k = 6.908745$. Figures (b)-(e) are magnifications around the indicated islands and the color bar is in logarithmic scale.	62

Figure 4.8 – The uncertainty fraction as a function of ε for (a)-(e) the phase space regions shown in Figure 4.7 and given by Table 4.1 and (f) for the region around the central island in Figure 4.7(a) given by the last row of Table 4.1. We observe a power law dependence, however, now it is possible to associate different exponents with different intervals of ε . We choose 5.0×10^4 random initial conditions for each value of ε , and we perform these simulations twenty-five times for (a) and (b) and ten times for (c)-(f). We compute the uncertainty exponent for each one of these simulations and take its mean and standard deviation: $\alpha = \bar{\alpha} \pm \sigma_\alpha$ 63

Figure 5.1 – Examples of recurrence matrix for different dynamical processes. (a) Uniformly distributed white noise, generated using the Numpy (123) function *random.normal* with zero mean and standard deviation equals to unity, (b) periodic dynamics, generated using a sine wave $x(t) = \sin(t)$, for $t \in [0, 50]$, (c) quasiperiodic dynamics ($\lambda_1 = 0.00014$), generated using the standard map (3.3) with $k = 1.5$, and initial condition $(\theta_0, p_0) = (1.0, 0.0)$, (d) chaotic dynamics ($\lambda_1 = 0.43214$), generated using the standard map (3.3) with $k = 1.5$ and initial condition $(\theta_0, p_0) = (2.85, 0.0)$, (e) chaotic dynamics ($\lambda_1 = 0.33276$), generated using the standard map (3.3) with $k = 1.5$ and initial condition $(\theta_0, p_0) = (1.6, 0.0)$, and (f) chaotic dynamics ($\lambda_1 = 2.18496$), generated using the standard map (3.3) with $k = 9.0$ and initial condition $(\theta_0, p_0) = (3.0, 0.0)$. The threshold is $\varepsilon = \sigma/100$ in (a) and $\varepsilon = \sigma/10$ for (b)-(f), where σ is the standard deviation of the time series. The Lyapunov exponent of (c)-(f) have been calculated considering 1.0×10^5 iterations. 70

Figure 5.2 – The number of unique recurrence times, \mathcal{N}_τ^* , for 1000×1000 uniformly distributed initial conditions in a grid on the entire phase space $[-\pi, \pi] \times [-\pi, \pi]$ for $k = 1.5$. Each initial condition is chosen as the center of the recurrence region, with size $\varepsilon = \sigma/10$, where σ is the standard deviation of the time series generated by it. We iterate each initial condition for 2×10^6 times. 74

Figure 5.3 – (a) The largest Lyapunov exponent, (b) the recurrence rate, the RQA measures (c)-(g) based on diagonal lines, given by Eqs. (5.12)-(5.16), respectively, and (h)-(k) based on vertical lines, given by Eqs. (5.18)-(5.21), respectively, and (l) the recurrence time entropy [Eq. (5.23)] as a function of the nonlinearity parameter k , with a step of $\Delta k = 0.001$. The length of the time series is $N = 5000$, and for each parameter value, we choose a fixed initial condition of $(\theta_0, p_0) = (0.0, 1.3)$ 75

Figure 5.4 – (a)-(c) The largest Lyapunov exponent, λ_1 , and (d)-(f) the recurrence time entropy, RTE, for a 1000×1000 uniformly distributed initial conditions in a grid in phase space with $k = 1.5$, for (a), (b), (d), and (e) and in parameter space (k, p) , with $\theta_0 = 0.0$ for (c) and (f). Panels (b) and (e) are magnifications of the white boxes in (a) and (d), respectively, and the dotted white line in (c) and (f) represents the initial condition used in Figure 5.3.	77
Figure 5.5 – The RTE for a grid of 1000×1000 uniformly distributed initial conditions in the depicted phase space regions of the standard map (3.3), with (a) $k = 0.9$, (b) $k = 1.5$, (c) $k = 3.93$, (d) $k = 4.0$, (e) $k = 5.3$, and $k = 6.908745$. For each initial condition, we use a time series of length $N = 5000$. The regular orbits are characterized by small values of RTE (black to blue) while the chaotic orbits by a large value of RTE (green to red). The black points correspond to orbits for which none, or only one return time has been found. Increasing the length of the time series should decrease the size of the black regions. These regions also indicate the position of the elliptic points.	78
Figure 5.6 – (a) The finite-time RTE probability distribution for a single chaotic orbit with $n = 200$, $N = 1.0 \times 10^{10}$, $k = 1.5$, and $(\theta_0, p_0) = (-3.0, 0.0)$. (b) The finite-time RTE “time series” for the interval $[40000, 70000]$. The transitions between different regimes within the orbit’s dynamics are clear. Panel (c) is the phase space points that generate the minor maxima in (a) and (d) is a magnification of one of the period-6 satellite islands of (b) indicated by the red box.	80
Figure 5.7 – (a) The phase space points that generate the larger peak for high values of RTE in Figure 5.6(a) and (b) the log-log plot of the cumulative distribution of trapping times, $Q(\tau)$, for each sticky region identified in Figure 5.6(a) with $N = 10^{11}$ and $n = 200$ (colored dots). The inset is the log-lin plot of $Q(\tau)$ of the phase space points shown in (a). The colors of the dots in (b) match the colors of Figure 5.6(a).	81
Figure 5.8 – (a) The standard deviation, σ , as a function of k for the orbit with initial condition $(\theta_0, p_0) = (1.3, 0.0)$ iterated for 5000 times, using the (black) concatenation approach and the (red and blue) norm approach, considering the maximum and Euclidean norms, respectively, and (b) the correlation coefficient between λ_1 and RTE, both evaluated in the interval $k \in [0, 5]$, as a function of the threshold ε in units of the percentage of σ	82
Figure 6.1 – The billiard boundary for (a) $\gamma = 1$, (b) $\gamma = 2$, (c) $\gamma = 3$, (d) $\gamma = 4$, (e) $\gamma = 5$, and (f) $\gamma = 6$ with different values of ξ , namely, (black) $\xi = 0.0$, (red) $\xi = 0.15$, (blue) $\xi = 0.30$, (green) $\xi = 0.75$, (cyan) $\xi = 0.90$, and (purple) $\xi = 0.99999$	85

Figure 6.2 – (a) Illustration of two collisions on the billiard boundary and the angles used in the billiard map. Panels (b) and (c) illustrate the algorithm for finding the next collision point, discussed in the text.	87
Figure 6.3 – The phase space of the billiard map (6.11) with the boundary implicitly defined by Eq. (6.4) for 75 randomly chosen initial conditions iterated for $N = 3.0 \times 10^3$ times with (a)-(d) $\gamma = 1$, (e)-(h) $\gamma = 2$, and (i)-(l) $\gamma = 3$. Each column corresponds to different values of ξ , namely, (a), (e), (i) $\xi = 0.4$, (b)(f)(j) $\xi = 0.6$, (c)(g)(k) $\xi = 0.8$, and (d)(h)(l) $\xi = 0.99999$	89
Figure 6.4 – The configuration space of the billiard map for four different initial conditions with (a)-(d) $\gamma = 1$, (e)-(h) $\gamma = 2$, and (i)-(l) $\gamma = 3$. Each column corresponds to different values of ξ , namely, (a), (e), (i) $\xi = 0.4$, (b)(f)(j) $\xi = 0.6$, (c)(g)(k) $\xi = 0.8$, and (d)(h)(l) $\xi = 0.99999$. The respective orbit in phase space is shown as colored lines in Figure 6.3.	90
Figure 6.5 – The determinant of the Jacobian matrix in terms of (black) (θ, α) and in terms of (red) the Birkhoff coordinates (s, p) for $\gamma = 1$ and $\xi = 0.6$ with $(\theta_0, \alpha_0) = (\pi, \pi/2)$	92
Figure 6.6 – The largest Lyapunov exponent as a function of the parameter ξ for $\Delta\xi = 0.001$ with (black) $\gamma = 1$ and $(\theta_0, \alpha_0) = (\pi, \pi/2)$, (red) $\gamma = 2$ and $(\theta_0, \alpha_0) = (\pi/2, \pi/2)$, and (blue) $\gamma = 3$ and $(\theta_0, \alpha_0) = (\pi, 1.08)$. For each value of ξ , we consider $N = 1.0 \times 10^8$ collisions. The vertical dashed lines indicates the values of ξ of Figure 6.7.	93
Figure 6.7 – (a)-(c) The phase space of a single chaotic orbit with initial conditions (a) $(\theta_0, \alpha_0) = (\pi, \pi/2)$, (b) $(\theta_0, \alpha_0) = (\pi/2, \pi/2)$, and (c) $(\theta_0, \alpha_0) = (\pi, 1.08)$ for $N = 2 \times 10^6$ collisions. (d)-(f) The largest Lyapunov exponent, λ_1 [Eq. (3.20)], (g)-(i) dig quantity [Eq. (4.5)], and (j)-(l) the recurrence time entropy, RTE [Eq. (5.23)], for 1000×1000 initial conditions uniformly distributed in a grid on the entire phase space. Each column corresponds to specific values of γ and ξ [dashed vertical lines in Figure 6.6]: (left column) $\gamma = 1$ and $\xi = 0.785$, (middle column) $\gamma = 2$ and $\xi = 0.549$, and (right column) $\gamma = 3$ and $\xi = 0.375$	94

LIST OF TABLES

Table 4.1 – The first five rows corresponds to the phase space regions shown in Figures 4.6(b)-(f) and 4.7 given by $\{\theta, p \mid \theta_0 \geq \theta \geq \theta_1, p_0 \geq p \geq p_1\}$. The last row corresponds to the phase space region around the central island in 4.6(b) and 4.7(a).	62
Table 4.2 – The uncertainty exponent α , the dimension d , and the mean escape time $\langle T_{\text{esc}} \rangle$ of the phase space regions shown in Figure 4.7 and given by Table 4.1.	64
Table 5.1 – The correlation coefficient, ρ [Eq. (5.24)], between λ_1 and each one of the corresponding RQA measures for the standard map (3.3) in the interval $k \in [0, 5]$ (Figure 5.3) with a time series of length $N = 5000$ and initial condition $(\theta_0, p_0) = (0.0, 1.3)$ for each parameter value.	76

CONTENTS

1 INTRODUCTION	15
2 HAMILTONIAN SYSTEMS	22
2.1 HAMILTONIAN SYSTEMS	22
2.2 INTEGRABLE SYSTEMS	25
2.3 QUASI-INTEGRABLE SYSTEMS	27
2.4 THE KAM THEOREM	29
2.5 POINCARÉ SECTION	31
2.6 THE POINCARÉ-BIRKHOFF THEOREM	32
3 THE STANDARD MAP – A BRIEF SURVEY	36
3.1 THE KICKED ROTOR – THE STANDARD MAP	36
3.2 LYAPUNOV EXPONENTS	39
3.3 DIFFUSION	46
3.3.1 The Fokker-Plank-Kolmogorov Equation	46
3.3.2 Normal Transport	49
3.3.3 Anomalous Transport	52
4 EFFECTIVE FRACTAL DIMENSION AND STICKINESS	54
4.1 WEIGHTED BIRKHOFF AVERAGE	54
4.2 FRACTAL DIMENSION AND UNCERTAINTY EXPONENT	58
4.3 EFFECTIVE FRACTAL DIMENSION	60
5 CHARACTERIZATION OF STICKINESS USING RECURRENCE PLOTS	66
5.1 RECURRENCE PLOT	66
5.1.1 Definition	66
5.1.2 Structures in a Recurrence Plot	68
5.1.3 Recurrence Quantification Analysis	70
5.1.4 RQA Measures for the Standard Map	74
5.2 RECURRENCE TIME ENTROPY	76
5.3 THE EFFECT OF THE THRESHOLD ON THE RTE	81
6 DYNAMICAL PROPERTIES OF A BILLIARD MODEL	83
6.1 BILLIARD DEFINITION	83
6.2 MODEL AND MAPPING	84
6.3 NUMERICAL RESULTS	88
7 FINAL REMARKS	96
REFERENCES	99
APPENDIX A – PUBLISHED PAPERS	111

1 INTRODUCTION

The ancient Greek philosophers were pioneers in suggesting that abstract principles govern nature, and the earliest formal exploration of mechanics can be attributed to the era of Aristotle (384 – 322 B. C.). During the ancient Greek period, the prevailing belief was that physical entities were subject to changes, while celestial entities such as the Sun and stars remained unchanged. In his seminal work *Physics*, Aristotle established principles of change that govern all natural bodies. He categorized these changes into four distinct types: (i) change of place (motion), (ii) changes of substance (such as the transformation of the elements earth, water, air, and fire into each other, “coming to be”, and as well as “passing away”), (iii) change in quantity (size or number), and (iv) change in quality or alteration (*e.g.* a hot object becomes a cold object) (1, 2).

Aristotle introduced a dichotomy between natural and violent change (1, 2). Natural entities, composed of the four elements, exhibit inherent natural motion: those composed of earth and water possess a tendency to fall, seeking their place at the center of the Earth (and the Universe), while those composed of air and fire display a tendency to rise. Violent change, on the other hand, refers to any externally imposed motion on an object, and once the external force ceases, the object comes to rest.

An additional work from Aristotle’s era is the pseudo-Aristotelian *Problems of Mechanics*, which is considered to be one of the first surviving ancient Greek texts on mechanics (3, 4). The actual authorship of this book, whether it originated from Aristotle himself or a successor, remains uncertain, hence the prefix “pseudo”. This work delved into practical mechanical problems, primarily concerning simple machines. In the introduction, the author posed 35 questions, primarily centered around the principle of the lever, which played a seminal role in shaping mechanics throughout the ancient Greek period and well into the Medieval Age.

Today many of Aristotle’s principles have been proved wrong. However, it is important to understand that this was just the beginning of scientific knowledge. Aristotle’s contributions built the foundations to the development of science and he started a tradition of systematic and logical thinking to comprehend dynamics and nature, thereby providing a cornerstone upon which subsequent thinkers would build and refine their understanding.

The Aristotelian ideas of motion lasted for almost two millennia. It was only during the Middle Ages that his theory of motion came under criticism from scholars like John Philoponus (490 – 570 A. D.) and Ibn Sina, commonly known in the West as Avicenna (980 – 1037 A. D.). The central problem was the projectile motion, *i.e.*, why does a pebble continue to move after it has been thrown? Aristotle failed to answer this question and his idea of violent motion led Avicenna to introduce the concept of impetus (1) in *The Book of Healing* (1020) (5). In his book, Avicenna challenged Aristotelian mechanics and engaged in debates about the nature of motion, force, and the relationship between philosophy and science. These debates set the stage

for the gradual departure from pure philosophical reasoning and the incorporation of empirical observations and experimentation.

It was not until the experimental work and observations of Nicolaus Copernicus (1473 – 1543), Tycho Brahe (1546 – 1601), Johannes Kepler (1571 – 1630), and René Descartes (1596 – 1650) that the Aristotelian mechanics was abandoned altogether. However, the ones who in fact put an end to the reign of Aristotle’s ideas were Galileo Galilei (1564 – 1642) and Isaac Newton (1642 – 1727). Galileo is considered by many the father of modern science. He developed the telescope and his observations that the heavens may not be as perfect as Aristotle had thought was the first convincingly study to discredit Aristotle’s ideas. He also was the first to develop mechanics and kinematics in the way we know today. And even though it is highly debatable whether the famous Tower of Pisa experiment in fact happened or not, Galileo did carry out experiments with rolling balls on an inclined plane (6) and he correctly predicted that all objects fall at the same rate regardless of their mass. He was the first to state that uniform motion is indistinguishable from rest, laying the basis of the theory of relativity, and he also formulated the law of inertia, although today it is known as Newton’s first law.

In 1687, Newton published his pioneering book *Philosophiæ Naturalis Principia Mathematica* (Mathematical Principles of Natural Philosophy), popularly known as Principia. He defined for the first time concepts of space, mass, and quantity of motion (momentum), and most importantly, he provided a detailed mathematical description of mechanics using the newly developed mathematics of calculus, also invented by himself. He stated three laws which we know today as Newton’s law of motion laying the ground for Newtonian mechanics. These laws can be stated as follows:

1. Every body perseveres in its state of rest, or of uniform motion in a right line unless it is compelled to change that state by forces impressed thereon.
2. The alteration of motion is ever proportional to the motive force impressed; and is made in the direction of the right line in which that force is impressed.
3. To every action there is always opposed an equal reaction: or the mutual action of two bodies upon each other are always equal, and directed to contrary parts.

The first law is essentially Galileo’s law of inertia and it defines the term force. The second law relates force to mass and acceleration

$$\mathbf{F} = \frac{d\mathbf{p}}{dt} = m \frac{d^2\mathbf{x}}{dt^2},$$

where the right-hand side is obtained given a constant mass, *i.e.*, $m(t) \equiv m = \text{const}$. And even though the third law can be derived from the second law for rigid bodies (7, 8), it is, in general, an independent law. These laws are based on experiments and, therefore, cannot be derived from some other law.

Another of Newton's astonishing accomplishment was the derivation of the universal law of gravitation which states that every object of matter in the Universe attracts every other object with a force that is directly proportional to the product of their masses and inversely proportional to the square of the distance between their centers along the line of the centers of the two objects. This law correctly predicts planetary motion, although it has some flaws. The orbit followed by Mercury, for instance, is not the one predicted by Newton's law. However, it is important to understand the impact all these laws had on the scientific society at the time. From this point in History on, it was possible to use these mathematical tools to predict, in principle, the state of any object in the Universe given the forces that act upon it. This idea is what call today Newton's deterministic principle (8, 9), *i.e.*, the state of a system is given by the positions and velocities of the system's particles in a given instant of time, and the forces acting upon them uniquely determine the system's motion. This led Pierre-Simon Laplace (1749 – 1827) to state in his book *Essai philosophique sur les probabilités* (A philosophical essay on probabilities) (10) the following:

We may regard the present state of the universe as the effect of its past and the cause of its future. An intellect that at a certain moment would know all forces that set nature in motion, and all positions of all items of which nature is composed, if this intellect were also vast enough to submit these data to analysis, it would embrace in a single formula the movements of the greatest bodies of the universe and those of the tiniest atom; for such an intellect nothing would be uncertain and the future just like the past could be present before its eyes.

This statement, however, has been proved wrong even in the realm of classical mechanics (without even talking about quantum or relativistic mechanics) due to the existence of chaotic motion, which we will discuss shortly.

During the time of Newton, given the success of his theory of mechanics and the invention of calculus, scientists began to propose challenging problems worth solving. One such problem was the problem of the brachistochrone (shortest time). Johann Bernoulli (1667 – 1748) posed the following problem:

Given two points A and B in a vertical plane, what is the curve traced out by a point acted on only by gravity, which starts at A and reaches B in the shortest time?

According to legend, Newton managed to solve this problem shortly after first encountering it. This particular problem played a significant role in the development of the calculus of variations (7). The calculus of variations focuses on determining the extrema (either maximum or minimum) of functionals, which are often integrals involving functions and their derivatives. Several authors have contributed to this field, however, it was Leonhard Euler (1707 – 1783) the first to elaborate on the subject. Inspired by Euler's work, Joseph-Louis Lagrange (1736 – 1813) introduced an alternate formulation of mechanics, based on the system's energy rather than the individual forces that act upon it. The result of both the calculus of variation and Lagrange's

new formulation of mechanics came to be known as the Euler-Lagrange equation, given by

$$\frac{\partial \mathcal{L}}{\partial q} - \frac{d}{dt} \frac{\partial \mathcal{L}}{\partial \dot{q}} = 0,$$

where q and $\dot{q}(t) = dq/dt$, in the context of mechanics, are the independent generalized coordinate and velocity, respectively, and $\mathcal{L} \equiv \mathcal{L}(t, q, \dot{q})$ is the function which makes the functional

$$S[\mathcal{L}] = \int_{t_1}^{t_2} \mathcal{L}(t, q(t), \dot{q}(t)) dt$$

an extreme (either maxima or minima) with constant t_1 and t_2 . Lagrange's greatest contribution was realizing that by defining \mathcal{L} , the Lagrangian function, as the difference between the kinetic energy and the potential energy of the system, $\mathcal{L} = T - V$, and by defining the functional $S[\mathcal{L}]$ as the action of a mechanical system, one recovers the equations of motion when solving the Euler-Lagrange equation for conservative systems. This is based on the principle of least action, also known as Hamilton's principle, which states that the path taken by a physical system between two points in time is the one for which the action is minimized or stationary (7).

In 1833 the most important step in classical mechanics was taken with the work of William Rowan Hamilton (1805 – 1865). He reformulated the Lagrangian mechanics by defining a Legendre transformation (11) of \mathcal{L} with $(q, \dot{q}) \rightarrow (p, q)$, where he defined $p = \partial \mathcal{L} / \partial \dot{q}$ as the generalized (also conjugated or canonical) momentum. This transformation is assumed to have an inverse $(p, q) \rightarrow (q, \dot{q})$. Hamilton then introduced the Hamiltonian function, $\mathcal{H}(p, q, t)$, in terms of the Lagrangian as

$$\mathcal{H}(p, q, t) = p\dot{q} - \mathcal{L}(q, \dot{q}, t).$$

The Hamiltonian function is often called the energy function as when certain conditions are satisfied, \mathcal{H} equals the total mechanical energy of the system, *i.e.*, $\mathcal{H} = T + V$.

Lagrange's and Hamilton's formalisms of mechanics both have their individual advantages. For instance, it is possible to modify the Euler-Lagrange equation to include the Lagrange multipliers, which yield information about the constraint forces. Hamiltonian mechanics, on the other hand, provides a direct link between classical and quantum mechanics. The scope of this thesis relies on Hamiltonian systems, which, in simple terms (more details on Chapter 2), are any system where its dynamics is completely described by the Hamiltonian function. Examples of Hamiltonian systems are the motion of the planets and astronomical objects, the motion of ideal fluids or vortices, and the motion of a charged particle on a magnetic field, which can be used to confine plasma particles, to cite a few.

Up to this point in History, it was believed in a deterministic Universe, as we have mentioned. This perception was challenged when Jules Henri Poincaré (1854 – 1912) was trying to solve whether the solar system was stable or not. To simplify the problem, he considered the gravitational interaction of only three objects, and he demonstrated that given an arbitrary initial condition, it was not possible to obtain an analytical solution even for this simple system (12).

Only a few particular initial conditions result in exact solutions and he demonstrated that small changes in the initial conditions lead to a significant difference in the final state of the system, *i.e.*, the system is unpredictable. However, this unpredictability comes from the fact that it is impossible to know the exact value of the initial conditions. If one were to know the particles' positions and velocities with an infinite precision, then one would know for certain the future state of any system. Nevertheless, the measurement devices and numerical simulations have an intrinsic uncertainty (either the device's precision or the number of digits in the simulation), which leads to a rapidly divergence. This fast loss of information is the so-called deterministic chaos, or simply chaos.

Until Poincaré's work, it was believed that Hamiltonian systems could exhibit only regular solutions, *i.e.*, periodic or quasiperiodic solutions. After Poincaré's breakthrough, the interest in studying Hamiltonian systems that exhibit such a behavior grew fast and the question regarding the source of non-integrability arose. Given an integrable Hamiltonian system, how strong must a perturbation be so that the system is no longer integrable? In other words, how robust is the integrability when the Hamiltonian is slightly perturbed? It was only in the middle of the 20th century that this question began to be answered when Andrey Nikolaevich Kolmogorov (1903 – 1987) demonstrated that most of the quasiperiodic solutions (nonresonant *tori*) survive for small perturbations (13). Only the periodic orbits (resonant *tori*) and their neighborhood are destroyed. Almost a decade later, Jürgen Kurt Moser (1928 – 1999) rigorously proved Kolmogorov's conjecture for discrete area-preserving maps of an annulus (14) and Kolmogorov's student, Vladimir Igorevich Arnold (1937 – 2010), proved the conjecture for an analytical Hamiltonian (15). This result came to be known as the Kolmogorov-Arnold-Moser (KAM) theorem and it is the greatest contribution to classical mechanics of the 20th century.

Although there is no mathematical proof, it is believed that a typical Hamiltonian system exhibits both regular (periodic or quasiperiodic orbits) and chaotic components. Extensive numerical data indicates that this is true and these systems are referred to as quasi-integrable systems or systems with divided phase space. We can construct such a system by perturbing an integrable Hamiltonian and the remnants of the destroyed resonant *tori* form a chain of stable and unstable periodic orbits, as stated by another theorem of paramount importance: the Poincaré-Birkhoff theorem. The regular islands are located around the stable orbits and it is the instability of the unstable orbits the source of chaotic behavior. The coexistence of regular and chaotic domains is the origin of nonergodicity. A system in which almost all initial conditions (the exceptions have zero measure) produce chaotic solutions is called fully chaotic and a system where all of the phase space belongs to the same chaotic component is called ergodic (16).

In two-dimensional Hamiltonian systems, the *tori* that survive the perturbation, which are called KAM *tori*, form impenetrable barriers to the transport of chaotic orbits, *i.e.*, a chaotic orbit will never cross an island, and an originally regular orbit will never reach the chaotic sea. In higher dimensional systems, the codimension between the KAM *tori* and the phase space is greater than 1, and the *tori* do not separate the phase space into distinct and disconnected

domains. In this case global transport occurs, which is called Arnold diffusion (17). As the perturbation grows stronger, the nonresonant *tori* are destroyed and their remnants form Cantor sets (18) named *cantori* (19, 20). Even though the KAM theorem is only valid for sufficiently smooth and weak perturbations, this scenario of the destruction of invariant *tori* is observed in a broader context. The phase space of a typical Hamiltonian system consists of an infinite hierarchical structure of islands-around-islands embedded in the chaotic sea. The latter constitutes a fat fractal (21), which is a fractal set with an invariant measure (volume of the islands) greater than zero. Therefore, the exact boundary between the islands and the chaotic sea is extremely difficult to determine.

For the special case of two-dimensional systems, while the KAM *tori* are impenetrable barriers, the *cantori* form partial barriers to the transport in phase space as the chaotic orbits may still pass through one of the gaps in the *cantori*. This allows chaotic orbits to become trapped inside the region bounded by the *cantori* for long but finite periods of time. While trapped, a chaotic orbit behaves similarly to a quasiperiodic orbit and this leads to long periods of intermittency in the orbit's dynamics. This phenomenon is known as stickiness (22–33), and these successive trappings affect transport properties of the system such as the decay of temporal correlations, leading to non-standard statistical properties. Fully chaotic systems display rapidly decaying (exponential) temporal correlations (34, 35). The tent map (36) and Arnold's cat map (37) are examples of such systems, and we classify them as strongly chaotic systems since there are no regular structures in their phase space. For systems with divided phase space, the phenomenon of stickiness emerges and it causes a slower algebraic decay of temporal correlations and it affects the recurrence times statistics as well (27, 28, 38–45). The stickiness effect also leads to anomalous transport (27, 46–50). These systems are often referred to as weakly chaotic systems.

The importance of the phenomenon of stickiness was first noted by Contopoulos (22) in the context of celestial mechanics. Altmann *et al.* (31, 32) demonstrated that stickiness in a two-dimensional Hamiltonian system with non-hierarchical phase space is due to a family of marginally unstable periodic orbits (MUPOs) (38). Cristadoro and Ketzmerick (28) described the generation of stickiness in two-dimensional Hamiltonian systems with a mixed and hierarchical phase space, where they conjectured a universal power law decay of correlations. Contopoulos and Harsoula (29, 30) demonstrated that in addition to the stickiness due to the *cantori* that surround regular islands, there is another type of stickiness caused by the unstable asymptotic curves of unstable periodic orbits. They also established a relationship between the escape time through a *cantorus* with the largest eigenvalue of the unstable periodic orbit, with the size of the opening in the *cantorus*, and with the distance of the initial condition from the *cantorus*.

As for the quantification of the stickiness effect, the Lyapunov exponents (51–53) have been extensively used for such a task (54, 55). The Lyapunov exponents are a mathematical tool for quantifying chaotic behavior and they are the average exponential rate of divergence or convergence of nearby orbits in phase space. A chaotic orbit is characterized by a positive largest Lyapunov exponent, and while the chaotic orbit is trapped, it becomes “less” chaotic and the

value of the largest Lyapunov exponent decreases. In this way, it is possible to detect when an orbit enters a sticky region and also measure the time it remains trapped (54, 55). The recurrence time statistics (31, 32, 44, 45, 56) and the finite-time rotation number (57, 58) have also been employed for the detection of sticky orbits. However, due to the stickiness influence on the value of the Lyapunov exponents, which makes their convergence slower, they are not the optimal choice for distinguishing chaos and regularity for two-dimensional Hamiltonian systems. Therefore, we intend to explore alternate dynamical measures for the quantification of chaotic behavior in two-dimension Hamiltonian systems, and we use the paradigmatic standard map (or Chirikov-Taylor map) (59) as our model. We analyze two alternate measures. The first has been recently proposed and it is based on the ergodic theory for the calculation of time averages in phase space (60, 61) and it relies on the calculation of a weighted Birkhoff average (62–67). The second measure is the recurrence time entropy (RTE) (68–70) and it is based on recurrence plots (RPs) (71–76) and on Slater’s theorem (77–79), however, it was defined originally without any connection with RPs (68). While the first is excellent for distinguishing chaos and regularity, the second gives us more information about the trappings than the largest Lyapunov exponent does. Motivated by this, we calculate these measures for a further Hamiltonian system that also displays a hierarchical phase space: a billiard system.

This thesis is organized as follows. In Chapter 2, we introduce the Hamiltonian systems and briefly comment on some of the main features of quasi-integrable Hamiltonian systems. We introduce two of the most important theorems when studying Hamiltonian systems, the KAM and Poincaré-Birkhoff theorems. We present the conditions on whether the nonresonant *tori* are destroyed or not and discuss the fate of resonant *tori* (Poincaré-Birkhoff theorem) under the perturbation. In Chapter 3, we make a brief survey on the paradigmatic standard map. We also introduce the Lyapunov exponents and present an efficient algorithm for their computation for two-dimensional mappings. We finish Chapter 3 by following Zaslavsky’s derivation of the Fokker-Plank-Kolmogorov (FPK) equation and comment on the modifications to describe anomalous transport. Our contributions and new results are presented in Chapters 4-6. Chapters 4 and 5 are devoted to the study of nonstandard dynamical measures to detect and characterize chaotic behavior in the standard map. In Chapter 6 we introduce another class of Hamiltonian systems: the billiard system, and we apply these nonstandard measures to the study of a family of billiards whose shape depends upon two parameters. Chapter 7 contains our final remarks and by the end of the thesis, we present an appendix listing all the scientific papers published during the development of this thesis.

2 HAMILTONIAN SYSTEMS

We start this chapter by discussing the main features of Hamiltonian systems, their integrability conditions, and the effect of a small perturbation on these systems. We then introduce the Kolmogorov-Arnold-Moser (KAM) theorem, which states whether the system exhibits quasi-periodic motion under small perturbations. In the following, we discuss another theorem of paramount importance for conservative dynamical systems, namely, the Poincaré-Birkhoff theorem, which concerns the consequences of a perturbation in the periodic motion and the emergence of chaotic motion. The discussion of the features of Hamiltonian systems and the aforementioned theorems is based on Refs. (80–84).

2.1 HAMILTONIAN SYSTEMS

The state of a Hamiltonian system with N degrees of freedom is specified by a generalized coordinate vector $\mathbf{q} = (q_1, q_2, \dots, q_N)$ and by a generalized momentum vector $\mathbf{p} = (p_1, p_2, \dots, p_N)$. Its dynamics is completely described by a scalar function, $\mathcal{H}(\mathbf{p}, \mathbf{q}, t)$, called the Hamiltonian function, where t represents the time variable. The time evolution of this system is given by Hamilton's equations,

$$\frac{dq_i}{dt} = \frac{\partial \mathcal{H}(\mathbf{p}, \mathbf{q}, t)}{\partial p_i}, \quad (2.1a)$$

$$\frac{dp_i}{dt} = -\frac{\partial \mathcal{H}(\mathbf{p}, \mathbf{q}, t)}{\partial q_i}, \quad (2.1b)$$

with $i = 1, 2, \dots, N$. The solution of Eq. (2.1) determines the trajectory $(\mathbf{p}(t), \mathbf{q}(t))$ that the system follows in the $2N$ -dimensional space, characterized by the vectors \mathbf{q} and \mathbf{p} . We call this space the phase space of the system. Any set of variables (\mathbf{p}, \mathbf{q}) whose time evolution obeys a set of equations of the form (2.1) is called canonical, and p_i and q_i are conjugated variables.

An essential feature of Hamiltonian systems is given by Liouville's theorem¹ on the preservation of the phase space volume. Let $d\Gamma_t = d\mathbf{p}_t d\mathbf{q}_t$ be an element of phase volume at time t and let $f = f(\mathbf{p}, \mathbf{q}, t)$ be a distribution function of particles in phase space, which is normalized as

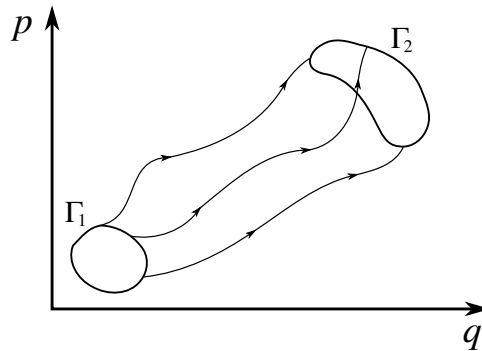
$$\int_{\Gamma} f(\mathbf{p}, \mathbf{q}, t) d\Gamma = 1. \quad (2.2)$$

Equation (2.2) corresponds to the conservation of the number of particles. Writing (2.2) in its differential form, we obtain the continuity equation

$$\frac{\partial f}{\partial t} + \nabla_{(\mathbf{p}, \mathbf{q})} \cdot (\mathbf{J}f) = 0, \quad (2.3)$$

¹ The proof of this theorem can be found in Ref. (9) even for a time-dependent Hamiltonian.

Figure 2.1: Time evolution of the phase space volume Γ_1 to Γ_2 . Liouville's theorem states that $\Gamma_1 = \Gamma_2 = \text{const.}$



Source: adapted from Figure 1.1 of Ref. (80).

where \mathbf{J} is the current vector in the $2N$ -dimensional phase space. We can rewrite Eq. (2.3) as

$$\frac{\partial f}{\partial t} + \sum_{i=1}^N \left(\frac{dq_i}{dt} \frac{\partial f}{\partial q_i} + \frac{dp_i}{dt} \frac{\partial f}{\partial p_i} \right) = 0,$$

which is called Liouville's equation. This equation represents the preservation of the phase space volume along the evolution of the dynamics. Any deformation in the initial condition volume is allowed (see Figure 2.1), however, there are no sources nor sinks. In other words, attractors and repellers are forbidden in Hamiltonian systems due to phase space volume conservation.

An essential concept in Hamiltonian dynamics is the Poisson bracket, which is defined for two arbitrary functions of the generalized coordinates and momentum, $f = f(\mathbf{p}, \mathbf{q})$ and $g = g(\mathbf{p}, \mathbf{q})$, as

$$[f, g] = \sum_{i=1}^N \left(\frac{\partial f}{\partial q_i} \frac{\partial g}{\partial p_i} - \frac{\partial f}{\partial p_i} \frac{\partial g}{\partial q_i} \right).$$

By choosing f as the generalized coordinate, or momentum, and g as the Hamiltonian function, we can rewrite Hamilton's equations as

$$\begin{aligned} \frac{dq_i}{dt} &= [q_i, \mathcal{H}], \\ \frac{dp_i}{dt} &= [p_i, \mathcal{H}]. \end{aligned}$$

For the general case when $f \equiv f(\mathbf{p}, \mathbf{q}, t)$, using Hamilton's equations (2.1), the time derivative of f can be written as

$$\frac{df}{dt} = [f, \mathcal{H}] + \frac{\partial f}{\partial t}.$$

If f does not depend explicitly on time, $\partial f / \partial t = 0$, and if $[f, \mathcal{H}] = 0$ (in this case we say that f commutes with \mathcal{H}), then f is a constant of motion. If the Hamiltonian does not depend explicitly

on time, \mathcal{H} is a constant of motion itself, given that its time derivative is

$$\frac{d\mathcal{H}(\mathbf{p}, \mathbf{q}, t)}{dt} = \frac{\partial \mathcal{H}}{\partial t},$$

since $[\mathcal{H}, \mathcal{H}] = 0$. If the Hamiltonian function of a system fulfills the aforementioned conditions, we call the system an autonomous system.

One of the advantages of Hamilton's formalism is that instead of solving a set of N ordinary differential equations of second order, which is the case of Newtonian and Lagrangian formalism, we need to solve a set of $2N$ ordinary differential equations of first order. Furthermore, it is possible to introduce a convenient change of variables in order to obtain a simpler set of equations of motion to find the trajectory of the system. However, not all change of variables preserves the canonical form of Hamilton's equations (2.1). The change of variables $(\mathbf{p}, \mathbf{q}) \rightarrow (\mathbf{P}, \mathbf{Q})$ that preserves the Hamiltonian form of the equations of motion is called canonical and we can obtain such transformation through generating functions, which depend on one old and one new variable, as follows:

$$S_1(\mathbf{q}, \mathbf{Q}, t), S_2(\mathbf{q}, \mathbf{P}, t), S_3(\mathbf{p}, \mathbf{Q}, t), S_4(\mathbf{p}, \mathbf{P}, t).$$

For example, in terms of S_2 , the canonical transformation is

$$p_i = \frac{\partial S_2}{\partial q_i}, \quad (2.4a)$$

$$Q_i = \frac{\partial S_2}{\partial P_i}, \quad (2.4b)$$

$$\overline{\mathcal{H}}(\mathbf{P}, \mathbf{Q}, t) = \mathcal{H}(\mathbf{p}, \mathbf{q}, t) + \frac{\partial S_2}{\partial t}. \quad (2.4c)$$

With these transformations, we can show, at least in a formal sense, how the equations of motion can be solved. For the case when the Hamiltonian depends explicitly on time, defining $\overline{\mathcal{H}} \equiv 0$ is equivalent to obtaining a new set of coordinates whose time derivatives are zero and the new coordinates are constants that can be understood as the initial conditions of the original set of equations. Thus, the transformation equations are, in fact, the solution of the system in terms of the initial values of position and momentum. By substituting (2.4a) into (2.4c) with $\overline{\mathcal{H}} \equiv 0$, we obtain a partial differential equation for the transformation

$$\mathcal{H}\left(\frac{\partial S_2}{\partial \mathbf{q}}, \mathbf{q}, t\right) + \frac{\partial S_2}{\partial t} = 0, \quad (2.5)$$

where S_2 , solution of Eq. (2.5), is called Hamilton's principal function. When the Hamiltonian does not depend explicitly on time, *i.e.*, when the system is autonomous, setting the new Hamiltonian as a constant is enough, $\overline{\mathcal{H}} \equiv E$, and the transformation (2.4c) becomes the Hamilton-Jacobi

equation

$$\mathcal{H}\left(\frac{\partial S_2}{\partial \mathbf{q}}, \mathbf{q}\right) = E, \quad (2.6)$$

where S_2 , in this case, is called Hamilton's characteristic function. Unless Eqs. (2.5) and (2.6) are separable, *i.e.*, unless it is possible to write

$$S = \sum_{i=1}^N S_i(\mathbf{p}, q_i),$$

$$\mathcal{H} = \sum_{i=1}^N \mathcal{H}_i(\mathbf{p}, q_i),$$

Eqs. (2.5) and (2.6) usually are extremely difficult to solve. Nevertheless, this formalism is useful in obtaining approximate series solutions for quasi-separable systems, or, as is more usually called, quasi-integrable systems, as we will see later on in this chapter.

2.2 INTEGRABLE SYSTEMS

For the special case when the Hamiltonian function does not depend explicitly on time, $\mathcal{H} = \mathcal{H}(\mathbf{p}, \mathbf{q})$ is a constant of motion, and the total energy of the system $E = \mathcal{H}(\mathbf{p}, \mathbf{q})$ is conserved. Therefore, orbits with energy E are restricted to lie on a $(2N - 1)$ -dimensional energy surface. If an autonomous Hamiltonian system with N degrees of freedom has N independent constants of motion $f_i(\mathbf{p}, \mathbf{q})$, $i = 1, 2, \dots, N$, and if these N constants mutually commute, *i.e.*, if $[f_i, f_j] = 0$ for all i, j , we say the system is integrable. If the last condition holds, we say the N constants are in involution, and the constants of motion f_i are independent if none of them can be expressed as a function of the $N - 1$ other constants. The requirement that an integrable system has N constants of motion implies that the trajectory of the system in the $2N$ -dimensional phase space is restricted to lie on a N -dimensional surface, and the requirement that the N constants are in involution restricts the topology of the surface to be a N -dimensional *torus*. Figure 2.2 is a representation of a two-dimensional *torus*.

Let us consider then an autonomous, integrable Hamiltonian system with N degrees of freedom. We can introduce a canonical change of variables such that the new Hamiltonian depends only on the new momentum vector, \mathbf{P} , *i.e.*, $\overline{\mathcal{H}} = \overline{\mathcal{H}}(\mathbf{P})$, such that $\partial \overline{\mathcal{H}} / \partial Q_i = 0 \forall i$. This can be done by choosing the components of the new momentum vector \mathbf{P} as the N constants of motion, $P_i = f_i(\mathbf{p}, \mathbf{q})$. Since f_i are constants,

$$\frac{dP_i}{dt} = \frac{df_i}{dt} = \frac{\partial \overline{\mathcal{H}}}{\partial Q_i} = 0,$$

and hence $\overline{\mathcal{H}} = \overline{\mathcal{H}}(\mathbf{P})$. As a matter of fact, we can consider any independent set of functions of the N constants of motion as the components of the new momentum vector. One particular choice is especially convenient and it makes the task of finding the trajectory of a system in the

Hamiltonian formalism much easier. The action-angle variables are canonically conjugated and denoted by $(\mathbf{P}, \mathbf{Q}) \equiv (\mathbf{I}, \boldsymbol{\theta})$, where the action \mathbf{I} is defined by

$$I_i = \frac{1}{2\pi} \oint_{C_i} \mathbf{p} \cdot d\mathbf{q}, \quad i = 1, 2, \dots, N,$$

and C_i are the paths on the N -dimensional *torus* (Figure 2.2). The canonically conjugated variable to the action, $\boldsymbol{\theta}$, is angle-like because on one circuit following one of the paths C_i around the *torus*, the variable θ_i increases by 2π , while the other variables θ_j return to their original values. This canonical transformation is defined in terms of a generating function,

$$S(\mathbf{I}, \mathbf{q}) = \int_{\mathbf{q}^{(0)}}^{\mathbf{q}} \mathbf{p}(\mathbf{I}, \mathbf{q}') \cdot d\mathbf{q}',$$

in the following way

$$\begin{aligned} \theta_i &= \frac{\partial S(\mathbf{I}, \mathbf{q})}{\partial I_i}, \\ p_i &= \frac{\partial S(\mathbf{I}, \mathbf{q})}{\partial q_i}. \end{aligned}$$

The *torus* is defined by the initial conditions, *i.e.*, by the constants of motion, f_i , and the new Hamiltonian does not depend on $\boldsymbol{\theta}$ by construction. Then the equations of motion are

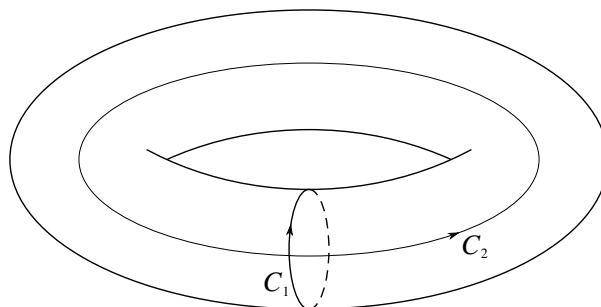
$$\begin{aligned} \frac{dI_i}{dt} &= -\frac{\partial \bar{\mathcal{H}}(\mathbf{I})}{\partial \theta_i} = 0, \\ \frac{d\theta_i}{dt} &= \frac{\partial \bar{\mathcal{H}}(\mathbf{I})}{\partial I_i} = \omega_i(\mathbf{I}), \end{aligned}$$

with solutions

$$I_i = \text{const}, \quad (2.7a)$$

$$\theta_i(t) = \theta_i(0) + \omega_i(\mathbf{I})t. \quad (2.7b)$$

Figure 2.2: Schematic representation of a two-dimensional *torus*.



Source: the author.

This solution is represented by N -dimensional *tori*, with the constant actions being its radius and the angle variables being cyclic. Thus, $\omega_i(\mathbf{I}) = \partial \overline{\mathcal{H}}(\mathbf{I}) / \partial I_i$ can be thought as the components of the nonlinear angular velocity vector and through this vector we can analyze the dynamics of the trajectories on the *torus*, which can be periodic or quasi-periodic. A trajectory on a *torus* is periodic if there is a vector of integer numbers $\mathbf{m} = (m_1, m_2, \dots, m_N)$ such that

$$\mathbf{m} \cdot \boldsymbol{\omega} = 0, \quad (2.8)$$

except when $\mathbf{m} \equiv \mathbf{0}$. This condition is known as the resonant condition and, in this case, the orbit closes on itself after m_1 circuits in θ_1 , m_2 circuits in θ_2 , ..., m_N circuits in θ_N .

Consider the case $N = 2$. The resonant condition (2.8) can be written in the following way

$$\frac{\omega_1}{\omega_2} = -\frac{m_2}{m_1}.$$

Since the coefficients m_i are integers, the ratio between the components of the angular velocity is a rational number, and due to that the set of *tori* that satisfy the resonant condition (2.8) are called rational *tori*. On the other hand, if the resonant condition is not satisfied, the trajectories are quasi-periodic, the ratio ω_1/ω_2 is an irrational number and the *tori* are called irrational *tori*.

For autonomous, integrable Hamiltonian systems with 2 degrees of freedom, the dynamics in the 4-dimensional phase space is restricted to a 2-dimensional *torus*, as shown in Figure 2.2. We can then associate two frequencies to each trajectory, which are the frequencies along each path C_i on the *torus*, defined by the vector $\boldsymbol{\omega}$. We define the rotation number (also known as winding number) of a trajectory as the ratio between these two frequencies as

$$\nu = \frac{\omega_1}{\omega_2},$$

which represents the average number of rotations performed along the two directions, C_1 and C_2 , *i.e.*, another way of defining whether the dynamics of a trajectory on the *torus* is periodic or quasi-periodic is by computing its rotation number. If we can write the rotation number as the ratio between two integer numbers, $\nu = r/s$, the trajectory is periodic on a rational *torus*. Otherwise, the trajectory is quasi-periodic on an irrational *torus*.

2.3 QUASI-INTEGRABLE SYSTEMS

We have previously seen that if we find a canonical transformation that transforms all actions into constants, Eq. (2.7) is the solution of the transformed system and the inverse transformation is the solution in the original coordinates. However, such transformation only exists for integrable systems, *i.e.*, a system with N degrees of freedom that has N constants of motion in involution, and integrable systems with more than one degree of freedom are very rare. We can then ask what the solution of a system that does not differ much from an integrable one looks

like. In other words, how robust is the integrability when the Hamiltonian is slightly perturbed? Intuitively, one might expect that any perturbation would destroy all constants of motion of the system, except for the energy $E = \mathcal{H}(\mathbf{p}, \mathbf{q})$. However, for a small perturbation, not all constants of motion are destroyed, and some of the N -dimensional *tori* survive the perturbation. The answer to these questions came with the very rigorous mathematical work of Kolmogorov (1954), Arnold (1963) and Moser (1962), and the result is what we call today the KAM theorem (13–15).

A typical approach to study this problem is to consider a perturbed Hamiltonian that is the sum of an integrable term, \mathcal{H}_0 , and a perturbative term, $\epsilon\mathcal{H}_1$,

$$\mathcal{H}(\mathbf{p}, \mathbf{q}) = \mathcal{H}_0(\mathbf{p}, \mathbf{q}) + \epsilon\mathcal{H}_1(\mathbf{p}, \mathbf{q}). \quad (2.9)$$

We wish to obtain a canonical transformation such that the new Hamiltonian is a function only of the actions. We express the Hamiltonian (2.9) in terms of the action-angle variables of the unperturbed Hamiltonian,

$$\mathcal{H}(\mathbf{I}, \boldsymbol{\theta}) = \mathcal{H}_0(\mathbf{I}) + \epsilon\mathcal{H}_1(\mathbf{I}, \boldsymbol{\theta}). \quad (2.10)$$

with

$$\begin{aligned} I_i &= \text{const}, \\ \theta_i(t) &= \theta_i(0) + \omega_i(\mathbf{I})t, \\ \omega_i &= \frac{\partial \mathcal{H}_0}{\partial I_i}. \end{aligned}$$

We seek a transformation $(\mathbf{I}, \boldsymbol{\theta}) \rightarrow (\bar{\mathbf{I}}, \bar{\boldsymbol{\theta}})$ of the form

$$\begin{aligned} I_i &= \frac{\partial S(\bar{\mathbf{I}}, \boldsymbol{\theta})}{\partial \theta_i}, \\ \bar{\theta}_i &= \frac{\partial S(\bar{\mathbf{I}}, \boldsymbol{\theta})}{\partial \bar{I}_i}. \end{aligned}$$

such that $\bar{\mathcal{H}} = \bar{\mathcal{H}}(\bar{\mathbf{I}})$. The Hamilton-Jacobi equation (2.6) for S , using (2.10), becomes

$$\begin{aligned} \mathcal{H}\left(\frac{\partial S}{\partial \boldsymbol{\theta}}, \boldsymbol{\theta}\right) &= \bar{\mathcal{H}}(\bar{\mathbf{I}}), \\ \mathcal{H}_0\left(\frac{\partial S}{\partial \boldsymbol{\theta}}\right) + \epsilon\mathcal{H}_1\left(\frac{\partial S}{\partial \boldsymbol{\theta}}, \boldsymbol{\theta}\right) &= \bar{\mathcal{H}}(\bar{\mathbf{I}}). \end{aligned} \quad (2.11)$$

One possible approach for solving (2.11) is expanding S in the form of a power series in ϵ ,

$$S = S_0 + \epsilon S_1 + \epsilon^2 S_2 + \dots, \quad (2.12)$$

where we choose the 0th order term to generate the identity transformation $(\mathbf{I}, \boldsymbol{\theta}) \rightarrow (\bar{\mathbf{I}}, \bar{\boldsymbol{\theta}})$, *i.e.*,

$S_0 = \bar{\mathbf{I}} \cdot \boldsymbol{\theta}$. Substituting (2.12) in (2.11), we have

$$\mathcal{H}_0\left(\bar{\mathbf{I}}, \epsilon \frac{\partial S_1}{\partial \boldsymbol{\theta}}, \epsilon^2 \frac{\partial S_2}{\partial \boldsymbol{\theta}} + \dots\right) + \epsilon \mathcal{H}_1\left(\bar{\mathbf{I}}, \epsilon \frac{\partial S_1}{\partial \boldsymbol{\theta}}, \epsilon^2 \frac{\partial S_2}{\partial \boldsymbol{\theta}} + \dots, \boldsymbol{\theta}\right) = \overline{\mathcal{H}}(\bar{\mathbf{I}}). \quad (2.13)$$

Expanding (2.13) in power series of $\epsilon \ll 1$ and only retaining first order terms, we have

$$\mathcal{H}_0(\bar{\mathbf{I}}) + \epsilon \left[\frac{\partial \mathcal{H}_0}{\partial \bar{\mathbf{I}}} \cdot \frac{\partial S_1}{\partial \boldsymbol{\theta}} + \mathcal{H}_1(\bar{\mathbf{I}}, \boldsymbol{\theta}) \right] = \overline{\mathcal{H}}(\bar{\mathbf{I}}). \quad (2.14)$$

Next, we expand $S_1(\bar{\mathbf{I}}, \boldsymbol{\theta})$ and $\mathcal{H}_1(\bar{\mathbf{I}}, \boldsymbol{\theta})$ in a Fourier series in terms of the angle $\boldsymbol{\theta}$,

$$S_1 = \sum_{\mathbf{m}} S_{1,\mathbf{m}}(\bar{\mathbf{I}}) \exp(i\mathbf{m} \cdot \boldsymbol{\theta}), \quad (2.15a)$$

$$\mathcal{H}_1 = \sum_{\mathbf{m}} \mathcal{H}_{1,\mathbf{m}}(\bar{\mathbf{I}}) \exp(i\mathbf{m} \cdot \boldsymbol{\theta}), \quad (2.15b)$$

where $\mathbf{m} = (m_1, m_2, \dots, m_N)$ is a vector of integers. Substituting the expressions (2.15) in (2.14), we obtain in first order,

$$S_1 = i \sum_{\mathbf{m}} \frac{\mathcal{H}_{1,\mathbf{m}}(\bar{\mathbf{I}})}{\mathbf{m} \cdot \boldsymbol{\omega}_0(\bar{\mathbf{I}})} \exp(i\mathbf{m} \cdot \boldsymbol{\theta}), \quad (2.16)$$

where $\boldsymbol{\omega}_0(\mathbf{I}) \equiv \partial \mathcal{H}_0 / \partial \mathbf{I}$ is the N -dimensional nonlinear frequency vector for the corresponding action \mathbf{I} . At this point arises the question of whether the infinite sum (2.16) converges. This is the so-called ‘‘problem of small denominators’’ since the product $\mathbf{m} \cdot \boldsymbol{\omega}_0$ depends on \mathbf{I} and for some values of \mathbf{I} , $\mathbf{m} \cdot \boldsymbol{\omega}_0$ approaches the resonant condition (2.8). These \mathbf{I} define the resonant *tori* of the unperturbed system, *i.e.*, the rational *tori*, for which the denominator goes to zero and the sum (2.16) diverges. These resonant *tori* typically are destroyed for any perturbation $\epsilon > 0$. However, there is a large set of ‘‘very nonresonant’’ *tori* that survive the perturbation, which is the set of irrational *tori*, and the condition of whether they are destroyed or not is given by the famous KAM theorem.

2.4 THE KAM THEOREM

The KAM theorem has its origin in a conjecture made by Kolmogorov (13), which was proved by Arnold (15) assuming analytical \mathcal{H}_0 and \mathcal{H}_1 , and by Moser (14) assuming these functions have a finite number of derivatives. In this thesis, we will not exhibit the proof of this theorem, which can be found in Refs. (9, 13–15), and we will only discuss the conditions for its validity and its consequences.

As we have previously mentioned, the KAM theorem states that the nonresonant *tori* of an integrable system subjected to a small perturbation are only deformed, and not destroyed by it. The conditions on whether the *tori* are destroyed or not are the following:

1. the frequencies must be linearly independent, *i.e.*,

$$\mathbf{m} \cdot \boldsymbol{\omega}(\mathbf{I}) \neq 0,$$

where $\boldsymbol{\omega} = \partial \mathcal{H}_0 / \partial \mathbf{I}$ e \mathbf{m} is a vector of integers;

2. the perturbation must be smooth (there is a sufficient number of continuous derivatives of \mathcal{H}_1);
3. the initial conditions must be far enough from resonance to satisfy

$$|\mathbf{m} \cdot \boldsymbol{\omega}| \geq K_\epsilon(\boldsymbol{\omega}) |\mathbf{m}|^{-(N+1)} \quad (2.17)$$

for all \mathbf{m} , except $\mathbf{m} \equiv \mathbf{0}$, where $|\mathbf{m}| = |m_1| + |m_2| + \dots + |m_N|$ and $K_\epsilon(\boldsymbol{\omega}) > 0$ is a constant that does not depend on \mathbf{m} and goes to zero in the limit $\epsilon \rightarrow 0$.

The set of *tori* that fulfill all three conditions are called *KAM tori*. And since (2.17) cannot be satisfied for K_ϵ too large, and since K_ϵ increases with ϵ , there exists a condition of sufficiently small perturbation for the existence of the *KAM tori*.

For systems with two degrees of freedom, we can rewrite the inequality (2.17) as

$$\left| \nu - \frac{r}{s} \right| > \frac{K_\epsilon(\boldsymbol{\omega})}{s^{5/2}}, \quad (2.18)$$

where r and s are integer numbers. This means that the *tori* whose rotation number cannot be well approximated by a rational number are not destroyed by a small perturbation. These *tori* are “very irrational” and the last *KAM torus* to be destroyed is the one whose rotation number is the “most irrational”. We can measure how irrational a number is by computing its continued fraction expansion. Let $0 < \gamma < 1$ be an irrational number. We can express it as follows

$$\gamma = \frac{1}{a_1 + \frac{1}{a_2 + \frac{1}{a_3 + \dots}}} \equiv [a_1, a_2, a_3, \dots], \quad (2.19)$$

where the coefficients a_i are natural numbers. This expansion is unique and the truncation of this expansion after some finite number of terms gives a rational approximation of γ . Thus, the most irrational number is the one whose convergence rate of (2.19) is the slowest, *i.e.*, the one with the smallest a_i . Therefore, the most irrational number there is has $a_i = 1$ for all i . Such a number is known as the golden mean and is given by

$$g = \frac{\sqrt{5} - 1}{2} \approx 0.618 = [1, 1, 1, \dots].$$

A little less irrational than the golden mean are the so-called noble numbers. Their continued fraction expansion have the form $g_k = [k, 1, 1, 1, \dots]$, with $k > 1$.

In addition to the condition of sufficiently small perturbation, the system must be non-degenerate for the KAM theorem to be valid, and this imposes that the integrable part of the perturbed Hamiltonian (2.10) must satisfy the non-degeneracy condition, given by

$$\det \left| \frac{\partial^2 \mathcal{H}_0}{\partial I_j \partial I_k} \right| = \det \left| \frac{\partial \omega_j}{\partial I_k} \right| \neq 0 \quad (2.20)$$

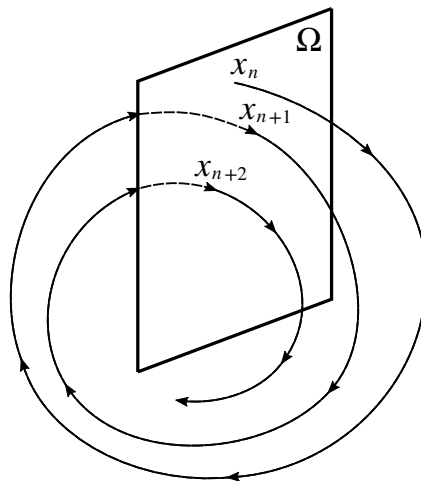
for all (\mathbf{p}, \mathbf{q}) . This means, essentially, that the unperturbed system must be nonlinear. For example, let $\omega_1 = \partial \mathcal{H}_0 / \partial I_1$ be a constant, *i.e.*, correspond to linear oscillations. In this way the condition (2.20) is violated and the KAM theorem cannot be applied. In other words, this condition implies that the rotation number, ν , must change monotonically through the surfaces of \mathcal{H}_0 .

Therefore, we have learned from the KAM theory that the nonresonant *tori* with rotation number sufficiently irrational keep their topology and are just slightly deformed in the presence of a small perturbation. However, on the resonant *tori* and in their neighborhood, the KAM theorem cannot be applied. The *tori* in this region are the ones that do not survive the perturbation and their fate is described by the Poincaré-Birkhoff theorem.

2.5 POINCARÉ SECTION

Before we state the Poincaré-Birkhoff theorem, let us introduce the Poincaré surface of section, or simply the Poincaré section. The Poincaré section is an extremely useful tool for the visualization of trajectories of dynamical systems. Systems with more than one degree of free-

Figure 2.3: Time evolution of a trajectory in phase space and its successive intersection with the Poincaré section Ω .



Source: adapted from Figure 1.3(a) of Ref. (80).

dom are difficult to deal with due to their high dimensionality and the Poincaré section is a way of representing a trajectory in the N -dimensional phase space in a $(N - 1)$ -dimensional space. It consists of a surface Ω in phase space transverse to the flow of trajectories, as shown in Figure 2.3. We define the Poincaré map by the successive intersections of a trajectory with the surface Ω in a particular way (*e.g.* from left to right). During the time evolution of the trajectory, there will be an arbitrary number of intersections, and we relate the n th intersection with the next through the Poincaré map:

$$(\mathbf{p}_{n+1}, \mathbf{q}_{n+1}) = \mathbb{P}(\mathbf{p}_n, \mathbf{q}_n).$$

In general, a particularly convenient choice for Ω can be made. For example, consider an autonomous Hamiltonian system with two degrees of freedom. The dynamics is restricted to lie on a three-dimensional surface $\mathcal{H}(p_1, p_2, q_1, q_2) = \mathcal{H}_0$ in the four-dimensional phase space. This equation allows us to write any of the four variables, *e.g.*, p_2 , as a function of the other three

$$p_2 = p_2(p_1, q_1, q_2, \mathcal{H}_0). \quad (2.21)$$

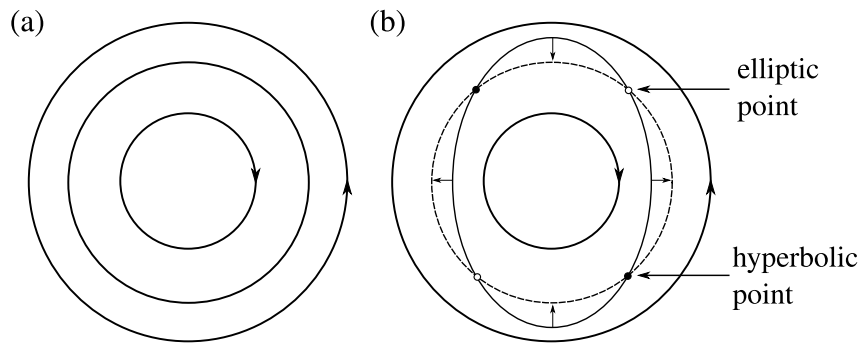
In case of a bounded motion, the trajectory crosses the plane $q_2 = \text{const}$ in the three-dimensional volume repeatedly. The plane p_1 - q_1 is, then, a convenient choice for the Poincaré section. Another example is the case of a Hamiltonian system with one degree of freedom with a periodic time dependency, $\mathcal{H}(p, q, t) = \mathcal{H}(p, q, t + \tau)$. In this case, we can construct the Poincaré section using the intersections of the trajectory with the $(\mathbf{p}(t_n), \mathbf{q}(t_n))$ plane for each multiple of the period τ , $t_n = t_0 + n\tau$.

In the Poincaré section, the resonant *tori* with rotation number $\nu = r/s$ are denoted by s points, and the nonresonant *tori* are denoted by closed invariant curves, since the dynamics is quasi-periodic and the points never return exactly to their original position, thus filling all the curve.

2.6 THE POINCARÉ-BIRKHOFF THEOREM

We have seen that most *tori* survive small perturbations. The resonant *tori*, however, do not survive. To simplify the discussion, we consider a resonant *torus* with rotation number $\nu = r/s$. Each point of the *torus* is a fixed point of the s -fold iterated unperturbed Poincaré map. If we assume that ν increases outward, then outside (inside) the rational *torus* there are *tori* with rotation number greater (smaller) than ν , which for s iterations of the mapping the points move counterclockwise (clockwise), as indicated schematically in Figure 2.4(a). Thus, between these two *tori*, there must exist a *torus* whose angular coordinate is constant under the s -fold iterated perturbed Poincaré map. These points only move radially under the action of the s -fold iterated map, and the full curve in Figure 2.4(b) is mapped into the dashed curve. Due to area preservation, the image of the full curve must enclose the same area as the original

Figure 2.4: The neighborhood of a resonant *torus*. (a) Illustration of an integrable system, where the middle curve represents the rational *torus* with rotation number $\nu = r/s$ ($s = 2$ in this illustration). The inner and outer curves represent the irrational *tori*. (b) Illustration of the perturbed system. The intersections between the dashed and full lines are the fixed points of the s -fold iterated Poincaré map. The inner and outer curves represent the irrational *tori* that survive the perturbation.



Source: adapted from Figure 3.3 of Ref. (80).

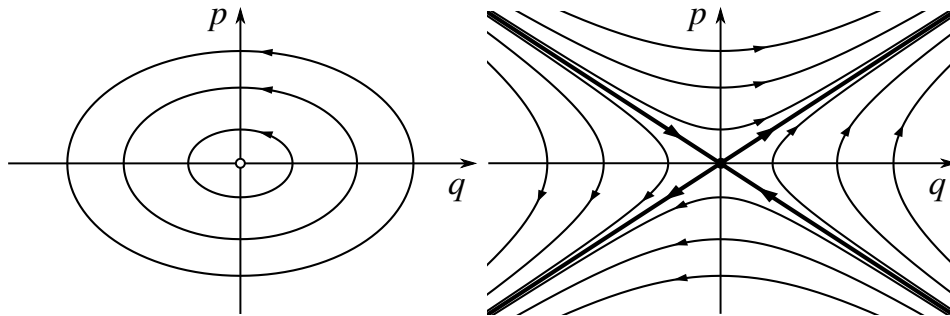
curve. This can only be possible if both curves intersect each other in an even number of points. Each one of the intersections returns to its original position under the action of the s -fold iterated perturbed Poincaré map. Thus, these intersection points are the fixed points of the Poincaré map. Therefore, for an even number of intersections, there must exist $2ks$ ($k = 1, 2, \dots$) fixed points, which are the so-called Poincaré-Birkhoff fixed points. Although generally $k = 1$, the theorem makes no claim about the value of k . Therefore, a resonant *torus* is not completely destroyed in the presence of a small perturbation. Its remnants form a chain of elliptic and hyperbolic fixed points alternately following each other.

The dynamics in the neighborhood of a fixed point differs fundamentally whether the fixed point is elliptic or hyperbolic. An elliptic point is a stable equilibrium point and the orbits in phase space circle about it. On the other hand, a hyperbolic point is an unstable equilibrium point. This point is characterized by two directions, one stable and one unstable. In this case, unless the orbit is initialized exactly over the stable direction, all orbits tend to move further away from the hyperbolic points' neighborhood. It is the hyperbolic points' instability the source of chaotic motion. These two behavior are exemplified in Figure 2.5.

Chaos arises in the neighborhood of the remnants of the destroyed resonant *tori* in thin bands. Smaller KAM *tori* are formed around the elliptic points created after the resonant *tori* destruction. In these regions, the motion is basically quasi-periodic, and the elements of the chains are called elliptic or regular islands. However, this is not valid for the entire phase space, since the previous discussion also applies here: the resonant *tori* are destroyed and around them, a new chain of elliptic and hyperbolic points is created again, but now in a smaller scale. If we magnify any of these small KAM *tori*, we see that the structure repeats itself for arbitrarily smaller scales.

It is interesting to analyze the consequences of the KAM and Poincaré-Birkhoff theorems for two-dimensional Hamiltonian systems, *i.e.*, systems where the dynamics is restricted to lie on a

Figure 2.5: Neighborhood of an elliptic point (on the left) and a hyperbolic point (on the right). The orbits that circle about the elliptic point in elliptical trajectories are called elliptical orbits. The thinner lines in the figure on the right represent hyperbolic orbits that move away from the hyperbolic point in all directions. The thicker lines are the asymptotes (stable and unstable directions) of the hyperbolic point.



Source: the author.

two-dimensional surface (Poincaré section). The trajectories that circle the elliptic points in these systems form islands in phase space² and a KAM *torus* divides the phase space into two distinct regions. These KAM *tori* act as barriers to chaotic motion since they are invariant curves that cannot be crossed by trajectories in phase space, thus separating chaotic and regular regions.

According to the KAM theorem, for small perturbations only the resonant *tori* are destroyed and most *tori* persist. Therefore, although present, the chaotic region volume is small. However, as the perturbation increases, more and more KAM *tori* disappear and originally separated chaotic bands merge in a great chaotic sea. The proportion of the area of the regular islands embedded in the chaotic sea gradually decreases and chaos grows stronger. It is worth mentioning that the KAM theorem is only valid for small perturbations, but for not-too-strong perturbations, several regular islands are still present in the chaotic sea. Since chaotic and regular domains occupy a finite area larger than zero, the phase space structures constitute a fat fractal (21).

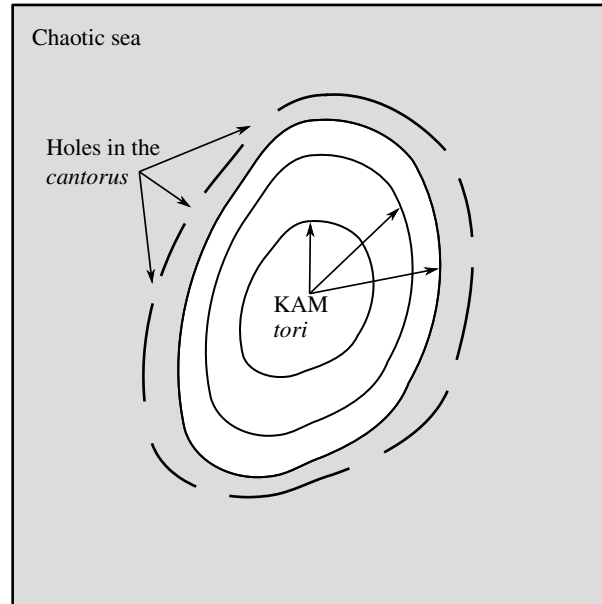
The fate of KAM *tori* after their destruction differs fundamentally from the fate of resonant *tori*. When a KAM *torus* is destroyed by the perturbation, it gives rise to a Cantor set³, called “*cantori*” (19, 20). Unlike the KAM *tori* which are full barriers to the transport in phase space, the *cantori* act as partial barriers, where trajectories may be trapped in a certain region bounded by them for a finite period of time, but eventually they will escape. The *cantori* are like a KAM *torus*, but with small holes through which the trajectory can pass through, as exemplified in Figure 2.6.

There is a hierarchical structure of regular islands, KAM *tori* and *cantori* that repeats itself for arbitrarily smaller scales. These regions bounded by *cantori* form the so-called dynamical traps (26). The chaotic orbits that approach an island may spend an arbitrarily long, but finite, time in this neighborhood, in which the orbits behave similarly as quasi-periodic orbits until

² From now on, unless stated otherwise, understand as phase space the appropriate Poincaré section.

³ The Cantor set is a set of points on line segments with the property that its dimension is a fractional value of approximately 0.63 (18).

Figure 2.6: Schematic representation of the phase space of a two-dimensional Hamiltonian system, where the chaotic sea is depicted in gray and the regular island in white. Within this island, there exist KAM *tori*, and surrounding the island are the remnants of a destroyed KAM *torus*, known as the *cantorus*.



Source: the author.

eventually they escape. This produces long intervals of intermittency with quasi-regular motion in the chaotic orbit, known as stickiness (22–33). Before the orbit escapes to the chaotic sea, it becomes trapped in regions bounded by *cantori*, and once inside this region, the orbit may cross an inner *cantorus* and so on to arbitrary small levels in this hierarchical structure of islands-around-islands.

3 THE STANDARD MAP – A BRIEF SURVEY

In this chapter we make a brief review of the paradigmatic standard map, introduced by Chirikov (59), and we illustrate all the features of Hamiltonian systems discussed in Chapter 2. We also introduce the Lyapunov exponents, which are the most successful mathematical tool to quantify chaos in dynamical systems, and we present the algorithm introduced by Eckmann and Ruelle (85) for the evaluation of the Lyapunov exponents for mappings. We also follow Zaslavsky derivation (27, 47, 82, 86–88) of the Fokker-Plank-Kolmogorov (FPK) equation, to obtain the kinetic description of chaotic dynamics, which results in the normal transport, and briefly comment on his modifications to the FPK equation to describe anomalous transport. Finally, we compute the diffusion exponent for different values of the nonlinearity parameter of the standard map.

3.1 THE KICKED ROTOR – THE STANDARD MAP

Let us now illustrate all these features of Hamiltonian systems discussed so far using the kicked rotor as an example. Consider a rod with length ℓ and moment of inertia I , which is attached to a frictionless pivot at one end. The other end of the rod experiences periodic pulses with intensity k/ℓ ($k > 0$) applied at time instants $t = 0, \tau, 2\tau, \dots$. There is no gravitational force, and the motion of the rod is confined to a plane. The generalized coordinates, in this case, are the angular position of the rod, θ , and the angular momentum, p . The Hamiltonian for this system is given by

$$\mathcal{H}(p, \theta, t) = \frac{p^2}{2I} - \frac{k}{\ell} \cos \theta \sum_n \delta(t - n\tau),$$

where $\delta(\cdot)$ is the Dirac delta function. From (2.1), the equations of motion are

$$\frac{dp}{dt} = -\frac{k}{\ell} \sin \theta \sum_n \delta(t - n\tau), \quad (3.1a)$$

$$\frac{d\theta}{dt} = \frac{p}{I}. \quad (3.1b)$$

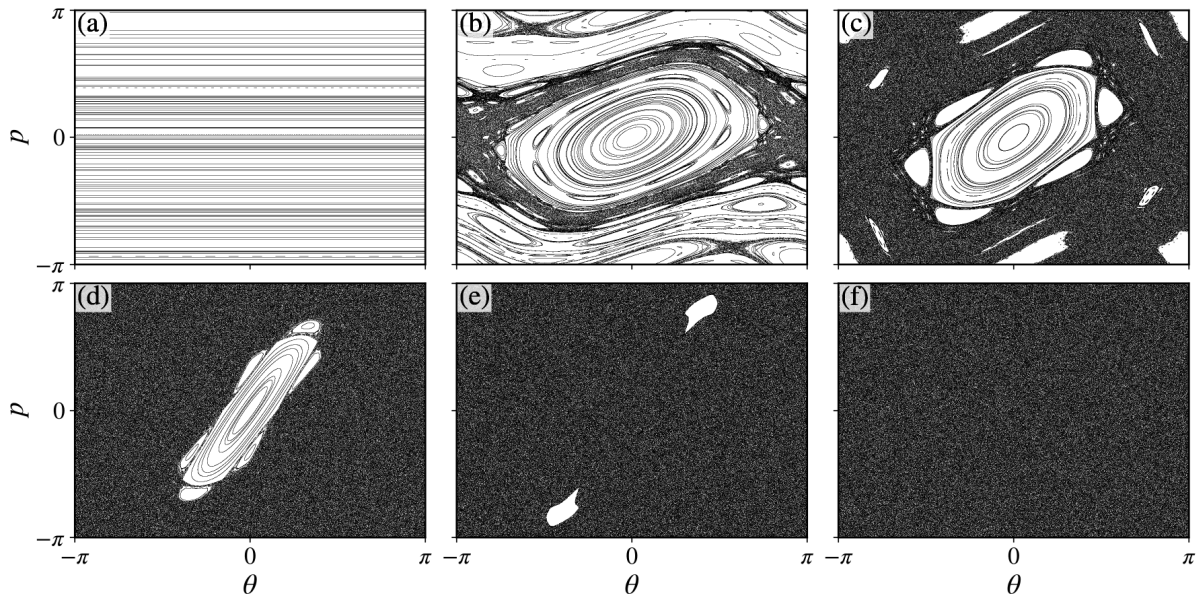
Between two kicks, there is no force acting on the rod, *i.e.*,

$$p = \text{const}, \quad (3.2a)$$

$$\theta = \frac{p}{I}t + \text{const}. \quad (3.2b)$$

For the Poincaré section, we consider the positions of θ and p immediately after each pulse. The solution before the n th pulse, $p(t_n^{(-)})$, $\theta(t_n^{(-)})$, with $t_n^{(\pm)} = n\tau \pm 0^+$, where 0^+ denotes a positive infinitesimal, can be connected to the solution immediately after the n th pulse, $p(t_n^{(+)})$, $\theta(t_n^{(+)})$,

Figure 3.1: The phase space of the standard map for 100 randomly chosen initial conditions iterated for $N = 1.5 \times 10^4$ times with (a) $k = 0.0$, (b) $k = 0.9$, (c) $k = 1.5$, (d) $k = 3.63$, (e) $k = 5.3$, and (f) $k = 9.0$.



Source: the author.

using (3.1) and (3.2)

$$p(t_n^{(+)}) - p(t_n^{(-)}) = -\frac{k}{\ell} \sin \theta_n,$$

$$\theta(t_n^{(+)}) - \theta(t_n^{(-)}) = \frac{p_{n+1} \tau}{I}.$$

We can set $\tau/I = 1$ and $\ell = 1$ without loss of generality, and we obtain, therefore, the mapping

$$\theta_{n+1} = \theta_n + p_{n+1} \pmod{2\pi}, \quad (3.3a)$$

$$p_{n+1} = p_n - k \sin \theta_n \pmod{2\pi}, \quad (3.3b)$$

where $\pmod{2\pi}$ in the first equation indicates that θ is an angular variable on the interval $[0, 2\pi)$, and k is the nonlinearity parameter. By taking $p \pmod{2\pi}$ the dynamics takes place on a *torus* $[-\pi, \pi] \times [-\pi, \pi]$ and by omitting it, the dynamics takes place on a *cylinder* $[-\pi, \pi] \times (-\infty, \infty)$. This map is called the “standard map” (or Chirikov-Taylor map) (59), and in spite of its simple mathematical form, it exhibits all the features of a typical quasi-integrable Hamiltonian system, and it has become a paradigmatic model for the study of Hamiltonian chaos.

For $k = 0$, the dynamics is regular, the system is integrable, p_n are all constants, and all orbits lie on invariant rotational *tori* [Figure 3.1(a)]. As the nonlinearity parameter k increases, the sufficiently irrational invariant rotational *tori* persists as invariant curves, as stated by the KAM theorem [Figure 3.1(b)], whereas the resonant *tori* are destroyed, and it is possible to observe

chaotic behavior for appropriate initial conditions. For the critical value of $k = k_c \approx 0.971635$ (89) the last invariant rotational *torus* ceases to exist, leading to a scenario of global stochasticity, and one single chaotic orbit fills a large portion of the phase space. For k not too large, several regular islands are still present in the chaotic sea [Figures 3.1(c)-3.1(e)] and as k increases even further, their size gradually decreases, until eventually, for sufficiently large values of k , almost no islands can be found embedded in the chaotic sea [Figure 3.1(f)].

We can find the period-1 fixed points of the map by requiring that

$$\begin{aligned}\theta_{n+1} &= \theta_n, \\ p_{n+1} &= p_n.\end{aligned}$$

From (3.3), we have

$$\begin{aligned}p_n - k \sin \theta_n &= 0, \\ k \sin \theta_n &= 0.\end{aligned}$$

The second equation demands that $\theta_n = m\pi$, where $m = 0, 1, 2, \dots$. The first one implies that $p_n = 0$. Therefore, there are two period-1 fixed points in the interval $\theta \in [0, 2\pi)$: $(\theta, p) = (0, 0)$ and $(\pi, 0)$. To analyze their stability, we need the stability matrix, also known as the Jacobian matrix. Given a mapping $\mathbf{x}_{n+1} = \mathbf{f}(\mathbf{x}_n) = \mathbf{f}^n(\mathbf{x}_0)$, the Jacobian matrix is given by

$$J_{ij} = \frac{\partial f_i}{\partial x_j}. \quad (3.4)$$

For the standard map (3.3), we have

$$J = \begin{pmatrix} \frac{\partial \theta_{n+1}}{\partial \theta_n} & \frac{\partial \theta_{n+1}}{\partial p_n} \\ \frac{\partial p_{n+1}}{\partial \theta_n} & \frac{\partial p_{n+1}}{\partial p_n} \end{pmatrix} = \begin{pmatrix} 1 - k \cos \theta_n & 1 \\ -k \cos \theta_n & 1 \end{pmatrix}. \quad (3.5)$$

The determinant of the Jacobian matrix, $|J|$, is related to the change in the phase space volume, where $|J| < 1$ indicates contraction and $|J| > 1$ indicates expansion. Thus, for area-preserving maps, $|J| = 1$ must hold for all points in phase space. Indeed, by taking the determinant of (3.5), we see that

$$|J| = 1 - k \cos \theta_n + k \cos \theta_n = 1.$$

For area-preserving maps, the stability of the fixed point can be estimated using their residue (89, 90), given by

$$R_i = \frac{1}{4} [2 - \text{Tr}(J_i^n)], \quad (3.6)$$

where Tr is the trace and J_i^n is the n time iterated Jacobian matrix of the i th period- n fixed point. An orbit is elliptic for $0 < R_i < 1$, parabolic for $R_i = 0, 1$ and hyperbolic otherwise. Therefore,

the residue for the first period-1 fixed point $(\theta, p) = (0, 0)$ is $R_1 = k/4$ and the orbit is elliptic if

$$0 < \frac{k}{4} < 1,$$

such that $k \in [0, 4]$. For the second fixed point, $R_2 = -k/4$, thus the orbit is hyperbolic for all values of $k > 0$.

3.2 LYAPUNOV EXPONENTS

As we have previously seen, the phase space of a typical quasi-integrable Hamiltonian system is neither fully integrable nor uniformly hyperbolic, but there is a coexistence of regular and chaotic domains. Furthermore, for two-dimensional Hamiltonian systems, these are distinct and disconnected domains. Therefore, it is of major importance the development of mathematical tools to characterize orbits into these two categories. One of the most important feature of chaotic motion is the so-called sensitivity to the initial conditions, *i.e.*, two initial conditions originally extremely close to each other tend to rapidly diverge, making the orbit unpredictable. The Lyapunov exponents (51–53) have proven to be one of the most useful dynamical diagnostic for chaotic motion, and they are the average exponential rate of divergence or convergence of nearby orbits in phase space.

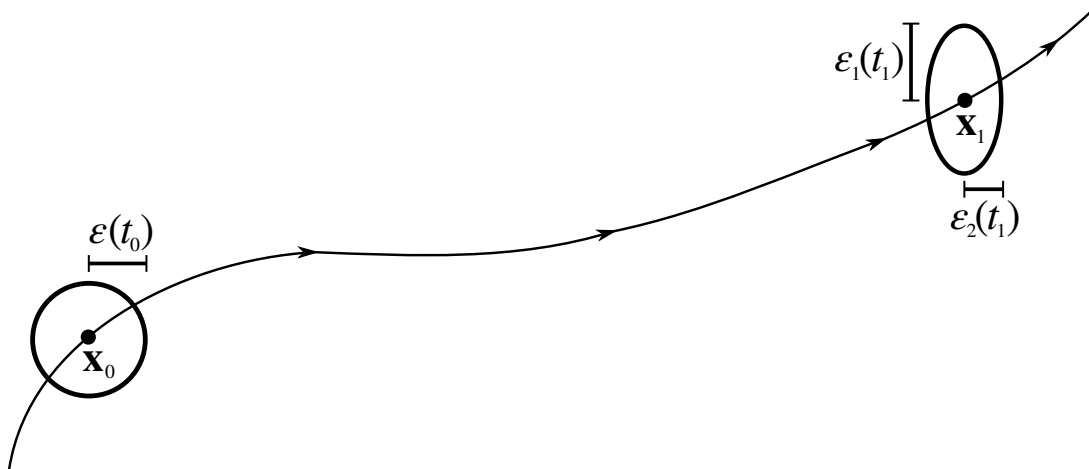
Consider now a set of initial conditions on an N -dimensional hypersphere of radius $\varepsilon(t_0) \equiv \varepsilon_0$ centered at the point \mathbf{x}_0 at time t_0 in phase space. With the temporal evolution of the initial conditions, at a later time t_1 , for example, this hypersphere will transform into an ellipsoidal hypersurface with axes measuring $\varepsilon_i(t_1)$, where $i = 1, 2, \dots, N$. In Figure 3.2, this process is schematically depicted for the two-dimensional case ($N = 2$). We define the Lyapunov exponents as a measure of the growth or decay of the principal axes $\varepsilon_i(t)$. Mathematically, they are defined by the limit

$$\lambda_i^\infty = \lim_{t \rightarrow \infty} \lim_{\varepsilon_0 \rightarrow 0} \frac{1}{t} \ln \frac{\varepsilon_i(t)}{\varepsilon_0}. \quad (3.7)$$

Therefore, an N -dimensional system has N characteristic Lyapunov exponents, and we say that the system is chaotic if at least one of them is positive. Moreover, the sum of all Lyapunov exponents is the negative of the phase space contraction rate (83). Therefore, for Hamiltonian systems, this sum must equal to zero. Hence, for systems with a two-dimensional phase space ($N = 2$), there are two exponents and they satisfy $\lambda_1 = -\lambda_2$. In this case, all periodic and quasiperiodic orbits have zero Lyapunov exponents, while chaotic orbits exhibit $\lambda_1 > 0$. Alternatively to the definition (3.7), it is possible to define the Lyapunov exponents in terms of the n iterate of the Jacobian matrix, \mathbf{Df}^n , of a mapping $\mathbf{x}_{n+1} = \mathbf{f}(\mathbf{x}_n) = \mathbf{f}^n(\mathbf{x}_0)$, as (85)

$$\lambda_i^\infty = \lim_{n \rightarrow \infty} \frac{1}{n} \ln (\|\mathbf{Df}^n u_i\|), \quad (3.8)$$

Figure 3.2: Temporal evolution of a two-dimensional sphere of initial conditions around the point \mathbf{x}_0 , where $\epsilon_i(t)$ denotes the length of its i th axis at time t .



Source: the author.

where u_i is the eigenvector corresponding to the i th eigenvalue of $D\mathbf{f}^n$ and we can write $D\mathbf{f}^n$ as

$$D\mathbf{f}^n = J(\mathbf{f}^{n-1}(\mathbf{x}_0))J(\mathbf{f}^{n-2}(\mathbf{x}_0)) \cdots J(\mathbf{f}(\mathbf{x}_0))J(\mathbf{x}_0) = \prod_{k=1}^n J(\mathbf{f}^{k-1}(\mathbf{x}_0)), \quad (3.9)$$

where J is the Jacobian matrix (3.4). There is also a similar definition to (3.8) for the continuous-time case, and it can be found in Ref. (85).

Both definitions of the Lyapunov exponents, (3.7) and (3.8), correspond to the infinite-time Lyapunov exponents. The infinite-time exponents capture the asymptotic behavior of orbits and they have the same value for almost every point in phase space. They are more commonly used in theoretical analysis rather than practical calculations, as it is impossible to numerically reach the infinite-time limit. Therefore, in practice, we truncate the computation of the Lyapunov exponents at some instant in time. We call this quantity the finite-time Lyapunov exponents (FTLE), $\lambda_i \equiv \lambda_i(\mathbf{x}_0, n)$, which, in general, depends on the chosen initial condition, contrary to its infinite-time counterpart.

In Refs. (51, 52) are described an efficient algorithm for the calculation of the spectrum of Lyapunov exponents when the equations of motion are explicitly known, and in Ref. (53) the same algorithm is described for an experimental time series. However, it is possible to exploit some matrix properties to increase the efficiency of the Lyapunov exponents computation. That is what Eckmann and Ruelle described in Ref. (85) and we will outline it shortly.

First, let the Jacobian matrix be the product of an orthogonal matrix O and an upper triangular matrix T ,

$$J = OT.$$

We can write the upper triangular matrix as

$$T = O^{-1}J.$$

Now, let us denote by J_n , O_n , and T_n the Jacobian, orthogonal, and upper triangular matrices at the instant n , respectively. Then, we can introduce the operator $O_0O_0^{-1}$ in (3.9), such that

$$\mathbf{Df}^n = J_{n-1}J_{n-2} \cdots J_1O_0O_0^{-1}J_0,$$

where we identify $O_0^{-1}J_0$ as T_0 and we can rewrite J_1O_0 as j_1 . Thus, we have

$$\mathbf{Df}^n = J_{n-1}J_{n-2} \cdots j_1T_0.$$

Applying now the operator $O_1O_1^{-1}$, we obtain

$$\begin{aligned} \mathbf{Df}^n &= J_{n-1}J_{n-2} \cdots J_2O_1O_1^{-1}j_1T_0, \\ &= J_{n-1}J_{n-2} \cdots j_2T_1T_0. \end{aligned}$$

Therefore, by continuously applying the operator $O_kO_k^{-1}$ in Df^n , and defining

$$T_{k+1} = O_{k+1}^{-1}j_{k+1} = O_{k+1}^{-1}J_{k+1}O_k, \quad (3.10)$$

we conclude that the n th iterate of the Jacobian matrix can be expressed in terms of the product of n upper triangular matrices,

$$\mathbf{Df}^n = T_{n-1}T_{n-2} \cdots T_1T_0 = \prod_{k=1}^n T_{k-1} = \mathcal{T}, \quad (3.11)$$

which is an upper triangular matrix itself, whose eigenvalues are its diagonal elements. Consequently, the Lyapunov exponents can be expressed in terms of the diagonal elements of \mathcal{T} as

$$\lambda_i^\infty = \lim_{n \rightarrow \infty} \frac{1}{n} \ln |\mathcal{T}_{ii}|. \quad (3.12)$$

We are interested in two-dimensional area-preserving mappings, such as the standard map. We use then the two-dimensional rotation matrix as the orthogonal matrix O to find the eigenvalues of \mathcal{T} ,

$$O = \begin{pmatrix} \cos \beta & \sin \beta \\ -\sin \beta & \cos \beta \end{pmatrix}. \quad (3.13)$$

Its inverse equals its transpose since O is an orthogonal matrix,

$$O^{-1} = \begin{pmatrix} \cos \beta & -\sin \beta \\ \sin \beta & \cos \beta \end{pmatrix}. \quad (3.14)$$

Rewriting (3.10) in its matrix form,

$$\begin{aligned} \begin{pmatrix} T_{11}^{k+1} & T_{12}^{k+1} \\ 0 & T_{22}^{k+1} \end{pmatrix} &= \begin{pmatrix} \cos \beta_{k+1} & -\sin \beta_{k+1} \\ \sin \beta_{k+1} & \cos \beta_{k+1} \end{pmatrix} \begin{pmatrix} J_{11}^{k+1} & J_{12}^{k+1} \\ J_{21}^{k+1} & J_{22}^{k+1} \end{pmatrix} \begin{pmatrix} \cos \beta_k & \sin \beta_k \\ -\sin \beta_k & \cos \beta_k \end{pmatrix}, \\ &= \begin{pmatrix} J_{11}^{k+1} \cos \beta_{k+1} - J_{21}^{k+1} \sin \beta_{k+1} & J_{12}^{k+1} \cos \beta_{k+1} - J_{22}^{k+1} \sin \beta_{k+1} \\ J_{11}^{k+1} \sin \beta_{k+1} + J_{21}^{k+1} \cos \beta_{k+1} & J_{12}^{k+1} \sin \beta_{k+1} + J_{22}^{k+1} \cos \beta_{k+1} \end{pmatrix} O_k. \end{aligned}$$

Therefore

$$T_{11}^{k+1} = \cos \beta_k (J_{11}^{k+1} \cos \beta_{k+1} - J_{21}^{k+1} \sin \beta_{k+1}) - \sin \beta_k (J_{12}^{k+1} \cos \beta_{k+1} - J_{22}^{k+1} \sin \beta_{k+1}), \quad (3.15)$$

$$T_{12}^{k+1} = \sin \beta_k (J_{11}^{k+1} \cos \beta_{k+1} - J_{21}^{k+1} \sin \beta_{k+1}) + \cos \beta_k (J_{12}^{k+1} \cos \beta_{k+1} - J_{22}^{k+1} \sin \beta_{k+1}), \quad (3.16)$$

$$0 = \cos \beta_k (J_{11}^{k+1} \sin \beta_{k+1} + J_{21}^{k+1} \cos \beta_{k+1}) - \sin \beta_k (J_{12}^{k+1} \sin \beta_{k+1} + J_{22}^{k+1} \cos \beta_{k+1}), \quad (3.17)$$

$$T_{22}^{k+1} = \sin \beta_k (J_{11}^{k+1} \sin \beta_{k+1} + J_{21}^{k+1} \cos \beta_{k+1}) + \cos \beta_k (J_{12}^{k+1} \sin \beta_{k+1} + J_{22}^{k+1} \cos \beta_{k+1}). \quad (3.18)$$

From (3.17) we obtain an expression for the angle β in terms of its previous value,

$$\tan \beta_{k+1} = \frac{-J_{21}^{k+1} \cos \beta_k + J_{22}^{k+1} \sin \beta_k}{J_{11}^{k+1} \cos \beta_k - J_{12}^{k+1} \sin \beta_k}, \quad (3.19)$$

and numerically, we compute the finite-time Lyapunov exponents as

$$\lambda_i = \frac{1}{n} \sum_{k=1}^n \ln |T_{ii}^k|, \quad (3.20)$$

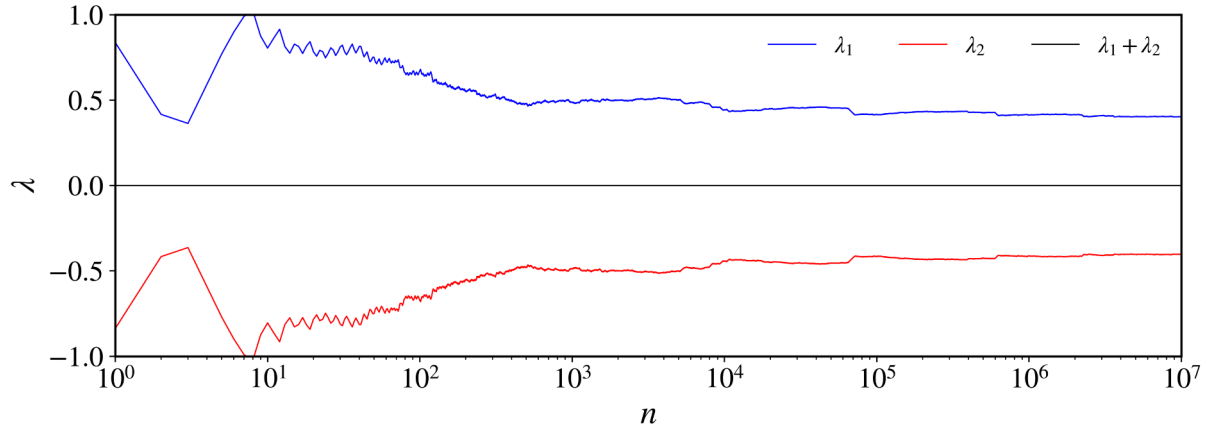
where we have omitted the dependency in \mathbf{x}_0 and n .

In Figure 3.3 is depicted the Lyapunov exponents time series for the standard map (3.3) with $k = 1.5$ for an initial condition lying on the chaotic sea. We observe a positive largest Lyapunov exponent (blue curve), indicating chaotic dynamics. Moreover, $\lambda_1 + \lambda_2 = 0$ for the entire time series (black curve), which corroborates the area-preservation feature of the map. We also observe that the convergence rate of the Lyapunov exponents to their asymptotic values is rather slow.

To develop a better understanding of the behavior of λ_1 as a function of time, we select four distinct chaotic initial conditions for $k = 0.9$ and $k = 1.5$ [Figure 3.4]. For $k = 0.9$ there are still several rotational invariant *tori* in phase space, which restrain the transport in the p -direction, resulting in distinct and disconnected chaotic domains. Each of these domains has its own characteristic Lyapunov exponents, which are related to the area of the chaotic component for fixed k (91)¹. The black region in Figure 3.4(a) has the largest area and, consequently, the largest Lyapunov exponent. For $k = 1.5$ [Figure 3.4(b)], there is only one chaotic domain

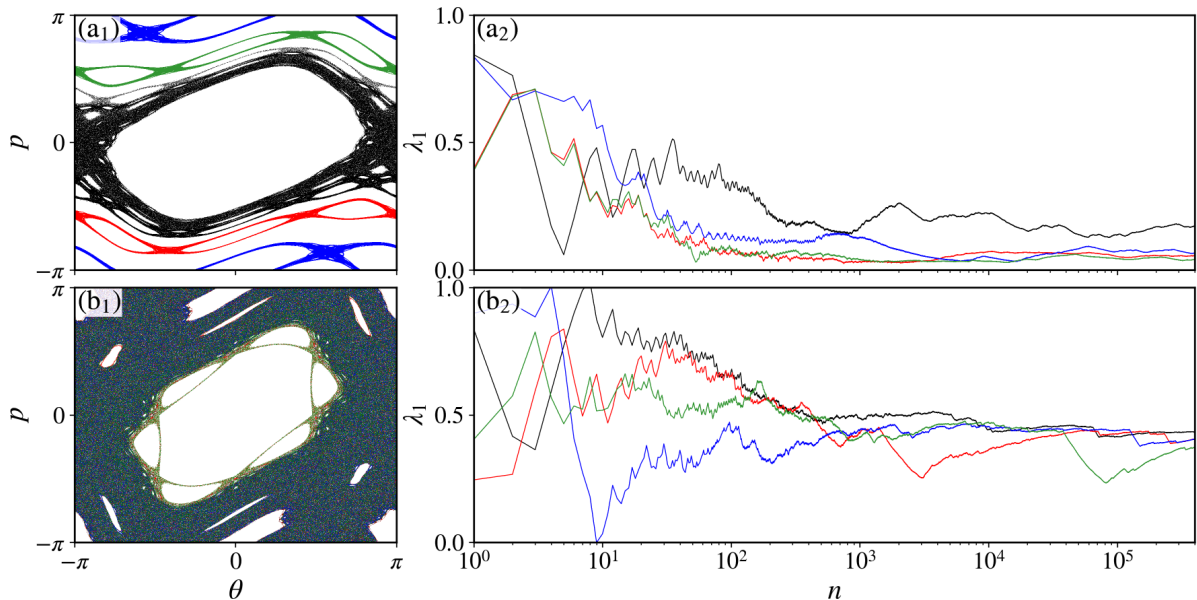
¹ In Ref. (91) the authors make a complete analysis of the characteristic times of the standard map, and also present empirical relations between the largest Lyapunov exponent with the area of the chaotic component, as well as with the nonlinearity parameter k .

Figure 3.3: The Lyapunov exponents time series of the standard map (3.3) with $k = 1.5$ and initial condition $(\theta_0, p_0) = (3.0, 0.0)$. In blue is the largest Lyapunov exponent, λ_1 , and in red the smallest Lyapunov exponent, λ_2 . As has been stated in the text, due preservation of phase space volume, the sum of all Lyapunov exponents must be zero, which is verified by the black curve, $\lambda_1 + \lambda_2$.



Source: the author.

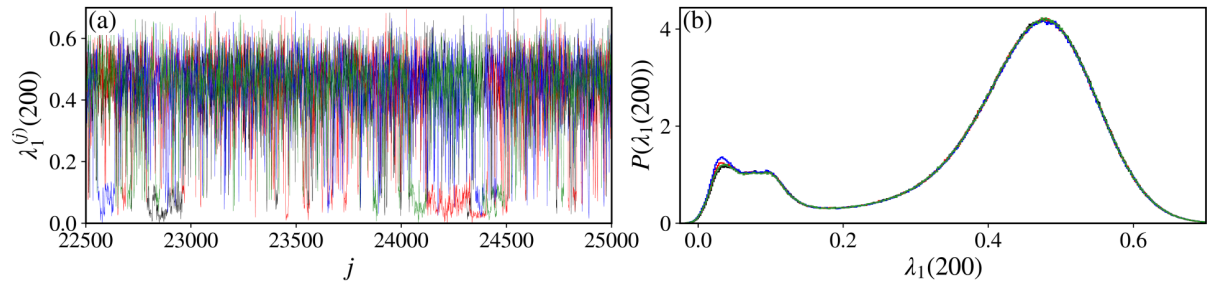
Figure 3.4: The phase space and the largest Lyapunov exponent time series of the standard map with (a) $k = 0.9$ and initial conditions (black) $(\theta_0, p_0) = (3.0, 0.0)$, (red) $(\theta_0, p_0) = (\pi, -\pi/2 - 0.12)$, (blue) $(\theta_0, p_0) = (\pi, -2.55)$, and (green) $(\theta_0, p_0) = (\pi, \pi/2 + 0.11)$, and with (b) $k = 1.5$ and initial conditions (black) $(\theta_0, p_0) = (3.0, 0.0)$, (red) $(\theta_0, p_0) = (2.87, 0.0)$, (blue) $(\theta_0, p_0) = (-\pi, -2.0)$, and (green) $(\theta_0, p_0) = (3\pi/2, -\pi)$.



Source: the author.

that fills a significant portion of phase space. The largest Lyapunov exponent of all selected initial conditions converges to the same asymptotic value, however, in this case, the trapping of chaotic orbits around the hierarchical structure of islands-around-islands previously discussed in Chapter 2 is more prominent, and is reflected by the several drops in the value of λ_1 as the

Figure 3.5: (a) The FTLE “time series” and (b) the FTLE probability distribution of the standard map with $k = 1.5$ and initial conditions (black) $(\theta_0, p_0) = (3.0, 0.0)$, (red) $(\theta_0, p_0) = (2.87, 0.0)$, (blue) $(\theta_0, p_0) = (-\pi, -2.0)$, and (green) $(\theta_0, p_0) = (3\pi/2, -\pi)$.



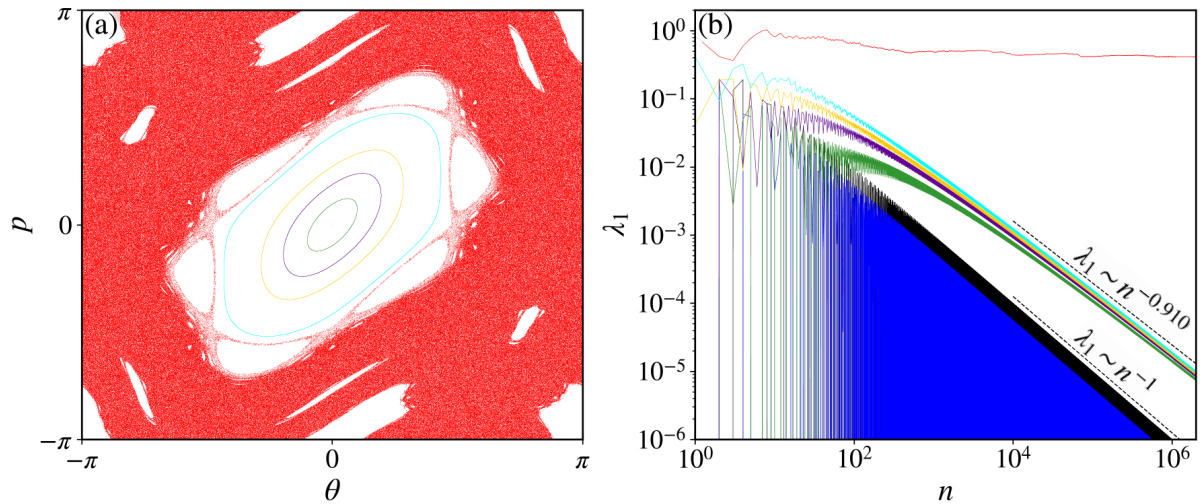
Source: the author.

dynamics evolves [Figure 3.4(b₂)]. These trappings that cause the sudden drops in the value of λ_1 make the Lyapunov exponent not the optimal choice to detect chaotic orbits, since it takes longer to reach its asymptotic value, increasing the computational effort needed.

Therefore, this irregular behavior of λ_1 as the orbit wanders through the chaotic sea makes it useful to compute the FTLE in windows of size m , along the evolution of a single orbit of length n , $\{\lambda_1^{(j)}(m)\}_{j=1,2,\dots,n/m}$, and define its probability distribution function, $P(\lambda_1(m))$. Szezech *et al.* (54) demonstrated that for parameter values for which the standard map exhibits sticky regions, *e.g.* $k = 1.5$, the FTLE distribution is bimodal [Figure 3.5(b)]. The FTLE “time series” [Figure 3.5(a)] exhibits abrupt changes in the value of $\lambda_1(m)$, indicating different transitions from different regimes in the dynamics of the orbit. These transitions cause the FTLE distribution to split into two modes, where the mode corresponding to higher values of $\lambda_1(m)$ indicates the windows when the orbit was in the bulk of the chaotic sea. Whereas, when the orbit is trapped, the value of $\lambda_1(m)$ decreases, and this corresponds to the secondary mode near zero.

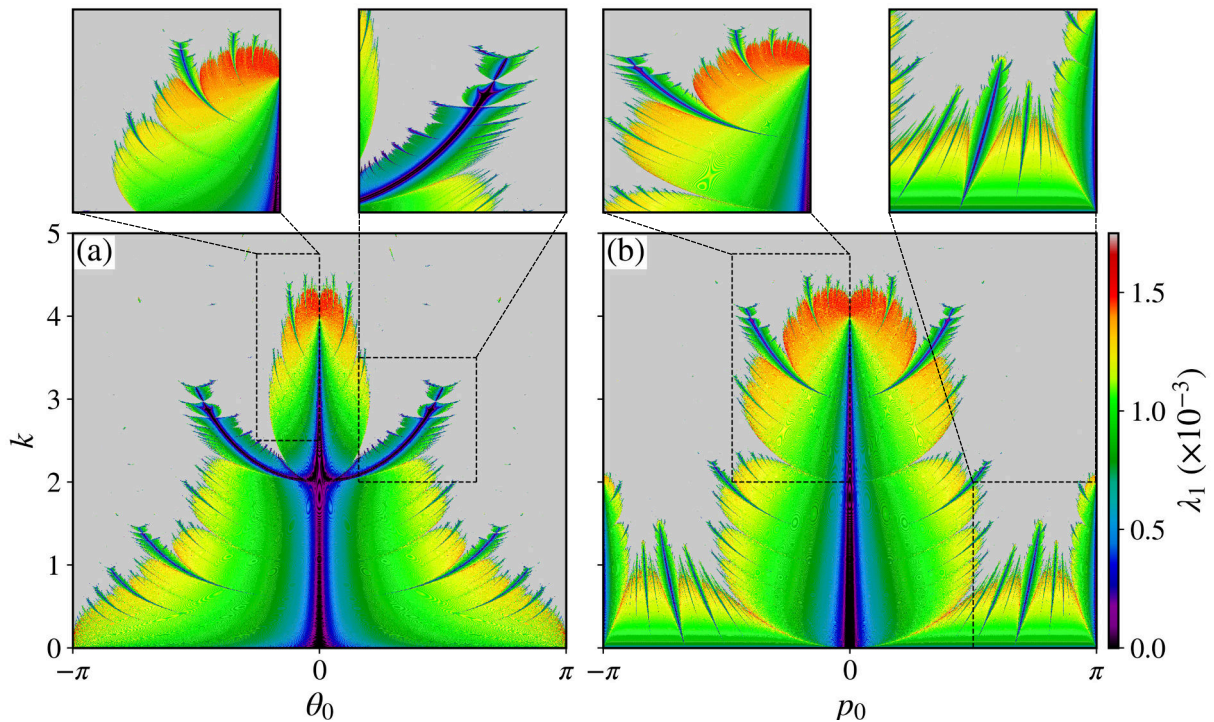
All regular orbits have zero Lyapunov exponents for infinite times, however, due to the finite-time nature of the numerically computed Lyapunov exponents, they converge to zero only when $n \rightarrow \infty$. Furthermore, the convergence rate depends on the chosen initial condition (92). The decays curves are shown in Figure 3.6(b) for the orbits shown in Figure 3.6(a). For the regular orbits, we observe a power-law decay, $\lambda_1 \sim n^{-\alpha}$. The red curve corresponds to the chaotic orbit, and naturally $\lambda_1 > 0$. The blue curve corresponds to the fixed point $(\theta, p) = (0.0, 0.0)$ and we observe a much faster convergence towards zero for this orbit than for the rest of them. And even though the magnitude of λ_1 for the irrational orbits are slightly different, the Lyapunov exponents of all irrational orbits converge to zero with the same rate. For the periodic orbit, the decay exponent is $\alpha = 1$, while for the quasi-periodic ones is $\alpha = 0.910 \pm 0.009$. It is important to stress that this is not a numerical artifact due to the numerical method. Manchein and Beims (92) reported the same behavior using the algorithm described in (51, 52), while we used Eckmann and Ruelle’s algorithm (85) previously described. Also, for this periodic orbit, we can analytically determine the largest Lyapunov exponent from the eigenvalues of the time- n

Figure 3.6: (a) The phase space and (b) the largest Lyapunov exponent time series of the standard map for $k = 1.5$ and $T = 2 \times 10^6$ with initial condition (red) $(\theta_0, p_0) = (3.0, 0.0)$, (blue) $(\theta_0, p_0) = (0.0, 0.0)$, (green) $(\theta_0, p_0) = (0.25, 0.0)$, (purple) $(\theta_0, p_0) = (0.5, 0.0)$, (yellow) $(\theta_0, p_0) = (0.75, 0.0)$, and (cyan) $(\theta_0, p_0) = (1.25, 0.0)$. The convergence rate of λ_1 towards zero is different for different initial conditions, where the fastest convergence rate is for the fixed point itself (red curve).



Source: adapted from Figure 1 of Ref. (92).

Figure 3.7: The largest Lyapunov exponent for a 1000×1000 grid of uniformly chosen values of (a) (k, θ_0) with $p_0 = 0$, and (b) (k, p_0) with $\theta_0 = 0$ and $T = 1.0 \times 10^4$.



Source: the author.

iterated Jacobian matrix,

$$\mathbf{Df}^n = \begin{pmatrix} 1 - k & 1 \\ -k & 1 \end{pmatrix}^n,$$

and we observe that both analytical and numerical λ_1 (black and blue curve of Figure 3.6, respectively) exhibit the same rate of decay (92).

This difference in the convergence rate allows us to locate where the periodic orbits are in phase space, and also study the bifurcations as the nonlinearity parameter k is varied. Figure 3.7 shows the conservative generalized bifurcation diagram (CGBD) (92) for the standard map, which can be constructed by calculating λ_1 in the parameter space. In this case, it can be $\theta_0 \times k$ with $p_0 = 0.0$ [Figure 3.7(a)] or $p_0 \times k$ with $\theta_0 = 0.0$ [Figure 3.7(b)]. The gray points correspond to chaotic orbits while the purple to red points around the main black lines correspond to irrational regular orbits whose largest Lyapunov exponent has not yet converged to zero, and they also define the size of the islands. Through this diagram, we can observe complex transitions from regular to chaotic dynamics as k changes. We also observe that the structure repeats itself for smaller scales (insets of Figure 3.7), characteristic of fractal boundaries.

3.3 DIFFUSION

3.3.1 The Fokker-Plank-Kolmogorov Equation

When studying Hamiltonian chaos, we can examine chaotic orbits using two different time scales of description: short t_c and large τ . On a short scale, we focus on the occurrence of chaos and the local properties of the system that contribute to the mixing of fast variables (phases). The Lyapunov exponents are commonly used to describe the local properties of chaos in this context. On a large scale, our attention shifts to the properties of orbit distributions and the system's kinetics. In simpler terms, we are interested in understanding the transport of particles within the system. To derive a kinetic description of chaotic dynamics is to reduce the number of variables by averaging over fast variables:

$$P(p, t) = \langle\langle P(p, q, t) \rangle\rangle,$$

where $P(p, q, t)$ is the probability density of having the particle at generalized momentum and coordinate p and q , respectively, at time t . The generalized coordinate q is considered as the fast variable and $\langle\langle \cdot \rangle\rangle$ denotes averaging over q . Therefore, we are interested in the derivation of a kinetic equation for $P(p, t)$ to describe chaotic dynamics. Such an equation is called the Fokker-Plank-Kolmogorov (FPK) equation and it was first used to investigate chaotic motion by Zaslavsky and Chirikov in 1972 (86).

The FPK equation was first obtained by Fokker and Plank, and later by Kolmogorov using a special scheme and conditions that are important for understanding some basic principles of kinetic (93). In the following, we will outline such derivation based on Refs. (27, 82, 88). Let

x be a characteristic variable of the wandering process, for example, a particle coordinate, and $W(x, t; x', t')$ be a probability density of having a particle at position x at time t if the particle was at position x' at time $t' \leq t$. An equation of the Markov-type process can be written for $W(x, t; x', t')$:

$$W(x_3, t_3; x_1, t_1) = \int W(x_3, t_3; x_2, t_2) W(x_2, t_2; x_1, t_1) dx_2, \quad (3.21)$$

which means that the transition from (x_1, t_1) to (x_3, t_3) can go through all possible states (x_2, t_2) . A typical assumption for W is its time uniformity, *i.e.*,

$$W(x, t; x', t') = W(x, x'; t - t'). \quad (3.22)$$

For small $\Delta t = t - t'$, we have, in first order,

$$W(x, x_0; t + \Delta t) = W(x, x_0; t) + \frac{\partial W(x, x_0; t)}{\partial t} \Delta t. \quad (3.23)$$

Equation (3.23) provides the existence of the limit

$$\lim_{\Delta t \rightarrow 0} \frac{W(x, x_0; t + \Delta t) - W(x, x_0; t)}{\Delta t} = \frac{\partial W(x, x_0; t)}{\partial t}, \quad (3.24)$$

which imposes some specific physical constraints that we will discuss in Section 3.3.2. Equation (3.21) consists of only one function W with different arguments, and the central point of this derivation is the distinction between functions W which correspond to different time scales. Let us introduce a new notation:

$$P(x, t) \equiv W(x, x_0; t), \quad (3.25)$$

where P will be used for t which satisfies the condition

$$t \ll t_c, \quad (3.26)$$

and t_c is a characteristic time that defines a short-scales time of the process. This explains the notation (3.25) since, in this case, $W(x, x_0; t) \equiv P(x, t)$ does not depend on the initial condition x_0 , contrary to $W(x, x_0; t + \Delta t)$ which defines the transition during a very short time interval. Thus, with these considerations and Eqs. (3.21) and (3.22), we can rewrite (3.24) as

$$\frac{\partial P(x, t)}{\partial t} = \lim_{\Delta t \rightarrow 0} \frac{1}{\Delta t} \left[\int W(x, y; \Delta t) P(y, t) dy - P(x, t) \right]. \quad (3.27)$$

For $\Delta t = 0$ it should be no transition if the velocity is finite, *i.e.*,

$$\lim_{\Delta t \rightarrow 0} W(x, y; \Delta t) = \delta(x - y). \quad (3.28)$$

For $\Delta t \ll 1$, (3.28) provides the following expansion (47)

$$W(x, y; \Delta t) = \delta(x - y) + A(y; \Delta t)\delta'(x - y) + \frac{1}{2}B(y; \Delta t)\delta''(x - y), \quad (3.29)$$

where we kept the terms up to second order, the prime denotes the derivative with respect to the argument and A and B can be expressed as moments of $W(x, y; \Delta t)$ as

$$A(y; \Delta t) = \int (y - x)W(x, y; \Delta t) dx \equiv \langle\langle \Delta y \rangle\rangle, \quad (3.30)$$

$$B(y; \Delta t) = \int (y - x)^2 W(x, y; \Delta t) dx \equiv \langle\langle (\Delta y)^2 \rangle\rangle. \quad (3.31)$$

Similarly, coefficients of higher order in the expansion of $W(x, y; \Delta t)$ can be expressed as higher moments of W .

The transition probability $W(x, y; \Delta t)$ satisfies two normalization conditions

$$\int W(x, y; \Delta t) dx = 1, \quad (3.32)$$

and

$$\int W(x, y; \Delta t) dy = 1. \quad (3.33)$$

By integrating (3.29) with respect to y and using (3.33), we obtain

$$A(y; \Delta t) = \frac{1}{2} \frac{\partial B(y; \Delta t)}{\partial y}, \quad (3.34)$$

or, applying the notations introduced in Eqs. (3.30) and (3.31),

$$\langle\langle \Delta y \rangle\rangle = \frac{1}{2} \frac{\partial}{\partial y} \langle\langle (\Delta y)^2 \rangle\rangle. \quad (3.35)$$

The final step of the derivation is to consider the Kolmogorov conditions (93): assuming the existence of the limits

$$\begin{aligned} \lim_{\Delta t \rightarrow 0} \frac{1}{\Delta t} \langle\langle \Delta x \rangle\rangle &\equiv \mathcal{A}(x), \\ \lim_{\Delta t \rightarrow 0} \frac{1}{\Delta t} \langle\langle (\Delta x)^2 \rangle\rangle &\equiv \mathcal{B}(x), \\ \lim_{\Delta t \rightarrow 0} \frac{1}{\Delta t} \langle\langle (\Delta x)^m \rangle\rangle &= 0, \text{ for } m > 2, \end{aligned} \quad (3.36)$$

we obtain the Fokker-Plank-Kolmogorov (FPK) equation from (3.27)

$$\frac{\partial P(x, t)}{\partial t} = -\frac{\partial}{\partial x} [\mathcal{A}(x)P(x, t)] + \frac{1}{2} \frac{\partial^2}{\partial x^2} [\mathcal{B}(x)P(x, t)], \quad (3.37)$$

which can be rewritten as a diffusion equation

$$\frac{\partial P}{\partial t} = \frac{1}{2} \frac{\partial}{\partial x} \left(D \frac{\partial P}{\partial x} \right) \quad (3.38)$$

after applying (3.34), with a diffusion coefficient

$$D = B = \lim_{\Delta t \rightarrow 0} \frac{\langle\langle (\Delta x)^2 \rangle\rangle}{\Delta t}. \quad (3.39)$$

By identifying

$$J = \frac{1}{2} D \frac{\partial P}{\partial x}$$

as the particle flux, (3.38) can be written in a divergent form that corresponds to the conservation of the number of particles:

$$\frac{\partial P}{\partial t} = \frac{\partial J}{\partial x}.$$

Furthermore, Eqs. (3.35), (3.36) and (3.39) provide an additional condition

$$\mathcal{A}(x) = \frac{1}{2} \frac{\partial D}{\partial x},$$

which shows that $\mathcal{A}(x)$ can be understood as the convective part of the particle flux, which is zero if $D = \text{const}$.

3.3.2 Normal Transport

Several authors have devoted time and effort to the solutions of the FPK equation (3.37) for different initial and boundary conditions (e.g. (94)). Here we will consider the most simple case, which we will refer to as normal transport. Considering $D = \text{const}$, $x \in (-\infty, \infty)$, $P(x, t = 0) = \delta(x)$, then we obtain a distribution known as Gaussian distribution

$$P(x, t) = \frac{1}{\sqrt{2\pi Dt}} \exp\left(-\frac{x^2}{2Dt}\right). \quad (3.40)$$

All its odd moments are zero, and its second moment is

$$\langle x^2 \rangle = Dt, \quad (3.41)$$

and higher moments are

$$\langle x^{2m} \rangle = D_m t^m.$$

As we have mentioned, Kolmogorov conditions (3.36) impose some physical constraints which limit the application of the FPK equation to real phenomena. For instance, consider the limit $\delta t \rightarrow 0$ and an infinitesimal displacement δx along a particle trajectory that corresponds to this limit. Then the particle velocity v is given by $\delta x / \delta t \rightarrow v$, and conditions (3.36) and with

notation (3.39) gives

$$\frac{(\delta x)^2}{\delta t} = v^2 \delta t = D = \text{const.}$$

This equation means that v should be infinite in the limit $\delta t \rightarrow 0$, which makes no physical sense. When we look at the solution (3.40), the same issue arises. The solution satisfies the initial condition $P(x, t = 0) = \delta(x)$, *i.e.*, a particle is at the origin at $t = 0$. For any finite time t , (3.40) gives a non-zero probability of the particle to be at any arbitrary point x , since $\exp(-x^2)$ goes to zero only when $x \rightarrow \infty$, which means the same as before: it is necessary an infinite velocity to propagate from $x = 0$ to $x \rightarrow \infty$ in a small time interval t . A physical approach to prevent this conflict to arise when using the FPK equation is to abandon the limit $\Delta t \rightarrow 0$ in (3.36) and to consider $\min \Delta t$, which satisfies the limit

$$\frac{t}{\min \Delta t} \rightarrow \infty.$$

To demonstrate how the FPK equation can be applied to real physical problems, consider the standard map (3.3). In this case, $\min \Delta t = 1$ and for $k \gg 1$ we can consider the angular variable θ to be random with an almost uniform distribution in the interval $[0, 2\pi)$ (59). Then

$$\begin{aligned} \langle\langle \sin \theta \rangle\rangle &= 0, \\ \langle\langle \sin^2 \theta \rangle\rangle &= \frac{1}{2}, \\ \Delta p_n &\equiv p_{n+1} - p_n, \\ \langle\langle \Delta p_n \rangle\rangle &= 0, \\ \langle\langle (\Delta p_n)^2 \rangle\rangle &= \frac{k^2}{2}, \end{aligned}$$

where $\langle\langle \cdot \rangle\rangle$ denotes average over θ . The corresponding FPK equation is

$$\frac{\partial P(p, t)}{\partial t} = \frac{1}{2} D(k) \frac{\partial^2 P(p, t)}{\partial p^2}, \quad (3.42)$$

with

$$D(k) = \frac{k^2}{2}. \quad (3.43)$$

A more sophisticated analysis of (3.42) gives an oscillatory behavior for $D(k)$ (95)

$$D(k) = \begin{cases} \frac{1}{2} k^2 \{ [1 - 2J_2(k)] [1 - J_2(k)] \}, & \text{for } k \geq 4.5, \\ 0.15(k - k_{\text{cr}})^3, & \text{for } k_c < k \leq 4.5, \end{cases} \quad (3.44)$$

where $k_c \approx 0.9716$ is the critical value when the last rotational invariant *torus* ceases to exist (89) and J_2 is the Bessel function of the first kind of order 2.

Numerically, we estimate the diffusion coefficient for the standard map as [*cf.* Eq. (3.41)]

(48, 49, 88, 91, 96, 97)

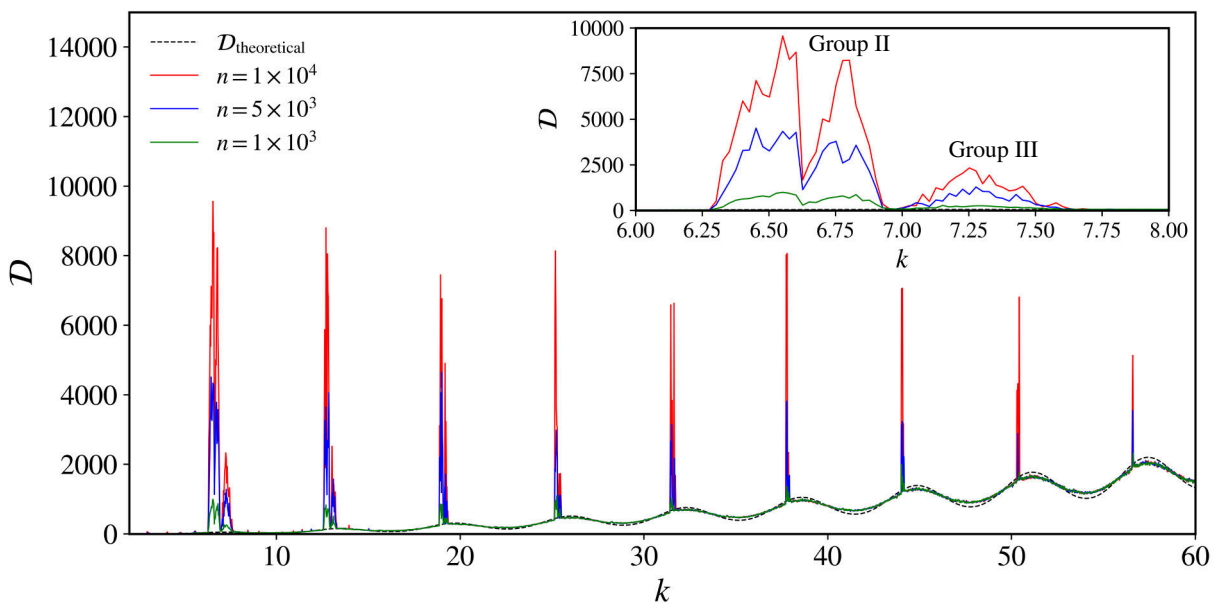
$$D(k) = \frac{\langle (p - p_0)^2 \rangle}{n}, \quad (3.45)$$

where n is the number of iterations of the mapping and $\langle \cdot \rangle$ denotes the average over a large ensemble of initial conditions. In general, we need a large number of iterations to ensure the convergence of the diffusion exponent, however, we do not observe a significant difference for different numbers of iterations (Figure 3.8). Also, we observe only small deviations of the numerically calculated diffusion coefficient (green, blue, and red lines) from its theoretical value (black dashed line). However, (3.44) fails for several intervals of k (inset of Figure 3.8). In these cases, the diffusion is anomalous and the diffusion coefficient goes to infinity when the number of iterations goes to infinity (48). That is the reason why the peaks of the red curve ($n = 1.0 \times 10^4$) are higher than the peaks of the green and blue curves ($n = 1.0 \times 10^3$ and $n = 5.0 \times 10^3$, respectively).

The anomalous diffusion has been related to the existence of accelerator modes (59), which corresponds to orbits that surround periodic orbits that are stable for values of k in the intervals

$$2\pi|l| \leq k \leq \sqrt{(2\pi l)^2 + 16}, \quad (3.46)$$

Figure 3.8: The diffusion coefficient, Eq. (3.45), for the standard map as a function of the nonlinearity parameter, with $\Delta k = 0.025$ for (green) $n = 1.0 \times 10^3$, (blue) $n = 5.0 \times 10^3$, and (red) $n = 1.0 \times 10^4$. In black dashed line is the theoretical value for the standard map as predicted in (3.44). We considered 100×100 initial conditions uniformly distributed in a grid on the entire phase space $[0, 2\pi] \times [0, 2\pi]$. Inset: magnification on the interval $k \in [6, 8]$ that shows the groups II and III of accelerator mode islands. We observe a deviation of the numerically calculated diffusion coefficient from its theoretical value.



Source: adapted from Figure 1 of Ref. (49).

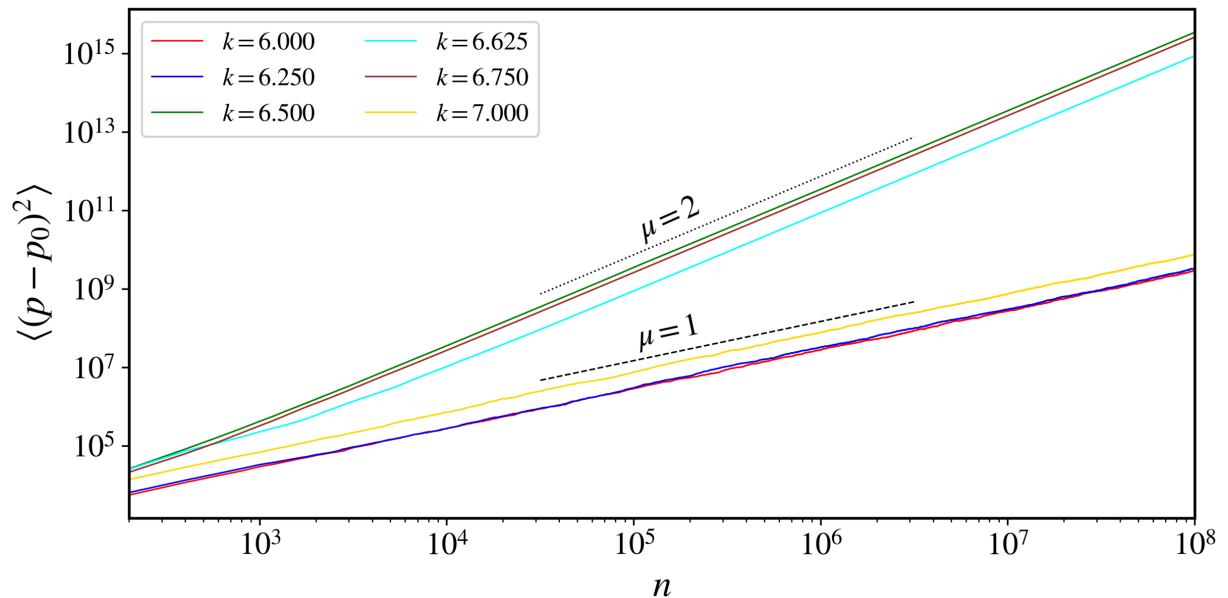
where $l > 0$ is an integer. Contopoulos *et al.* (98) named this kind of island group II islands (inset of Figure 3.8) and the moment of each orbit is increased by approximately 2π after each iteration. These islands appear in a recurrent way for values of k near $k = 2l\pi$, in intervals given by (3.46). There are also islands forming a third group, named group III, that appear for values of $k \approx (2|l| + 1)\pi$. The third group corresponds to periodic orbits of higher periods, and their role in the transport becomes less important with increasing k (49).

3.3.3 Anomalous Transport

To obtain an approximation to the anomalous transport in chaotic Hamiltonian systems, Zaslavsky (27, 47, 82, 87, 88) made a few modifications to the derivation of the FPK equation to include fractal time and fractional derivatives. He followed a similar scheme as introduced by Kolmogorov (93) and this lead him to a phenomenological, fractional kinetic equation, called the fractional Fokker-Plank-Kolmogorov equation (FFPK) or simply fractional kinetic equation (FKE). We will not outline this derivation, which can be found in Refs. (27, 47, 82, 87, 88). The main result is the generalization of the diffusion process, with the second moment of the distribution given by

$$\langle x^2 \rangle \sim t^\mu, \quad (3.47)$$

Figure 3.9: The variance of the momentum, $\langle (p - p_0)^2 \rangle$, as a function of the number of iterations n for (red) $k = 6.0$, (blue) $k = 6.25$, (green) $k = 6.5$, (cyan) $k = 6.625$, (brown) $k = 6.75$, and (yellow) $k = 7.0$. The black dashed (dotted) line indicates the slope of $\mu = 1$ ($\mu = 2$). We considered 30×30 initial conditions uniformly distributed in a grid on the entire phase space $[0, 2\pi] \times [0, 2\pi]$.



Source: the author.

where $\mu \in [0, 2]$ is the diffusion exponent (or transport exponent). When there are no accelerator mode islands present in phase space, we have normal diffusion and $\mu = 1$ (48, 49, 88, 97, 99). The case $\mu > 1$ is called superdiffusion and the case $\mu < 1$ subdiffusion. The case $\mu = 2$ is associated strictly with the presence of accelerator modes, and we have ballistic transport.

For the standard map (3.3), the generalization of (3.42) is defined by [*cf.* Eq. (3.47)]

$$\langle (p - p_0)^2 \rangle = D_\mu(k)n^\mu, \quad (3.48)$$

where $D_\mu(k)$ is the generalized classical diffusion constant, and the convergence of μ can be found for $n \rightarrow \infty$. Numerically, we obtain μ from the slope of the average of the variance of the momentum, $\langle (p - p_0)^2 \rangle$, as a function of the number of iterations in logarithmic scale (Figure 3.9). For the values of k where the diffusion coefficient (3.39) goes to infinity (Figure 3.8), there are accelerator mode islands of period 1 and the slope of the variance of the momentum as a function of n is $\mu = 2$ (green, cyan, and brown curves in Figure 3.9), whereas when there are no accelerator modes islands, we obtain the normal diffusion, with $\mu = 1$ (red, blue and yellow curves in Figure 3.9).

4 EFFECTIVE FRACTAL DIMENSION AND STICKINESS

We begin this chapter by introducing a new method based on a weighted Birkhoff average to distinguish chaotic and regular orbits in two-dimensional maps. We present this methodology for the standard map (3.3) for different values of the nonlinearity parameter and define a cutoff value above which the orbits are said to be regular, and chaotic otherwise. Next, we outline the uncertainty fraction method, used to compute the box-counting dimension of a boundary, and together with the weighted Birkhoff average method, we obtain the fractal dimension of the boundary for different values of the nonlinearity parameter k of the standard map and different levels in the hierarchical structure of islands-around-islands.

4.1 WEIGHTED BIRKHOFF AVERAGE

In Chapter 3 we have introduced the Lyapunov exponents as a mathematical tool for the detection of chaotic motion in phase space. Although widely used, the Lyapunov exponents exhibit a very slow convergence, as we have seen in Figures 3.4 and 3.6. When sticky domains are present in phase space, the convergence is even worse due to the successive trappings of chaotic orbits. Furthermore, the computation of the Lyapunov exponents is expensive because it is necessary to integrate both equations of motion and the linearized dynamics when using Benettin's method (52). When using Eckmann and Ruelle's method (85), however, it is not necessary to integrate the linearized dynamics, but it still requires the knowledge of the Jacobian matrix of the model, which is not always available. To avoid all these issues, a new method based on a weighted Birkhoff average has been proposed (62–67) and has been proved an excellent alternative to the Lyapunov exponents.

The Birkhoff average of a function $h : M \rightarrow \mathbb{R}$ on the phase space M along the trajectory of a map $f : M \rightarrow M$ beginning at a point $z_0 \in M$ is given by the sum

$$B_N(h; z_0) = \frac{1}{N} \sum_{n=0}^{N-1} h(f^n(z_0)). \quad (4.1)$$

The Birkhoff ergodic theorem (16) states that if the trajectory is ergodic, then the time average of a function h along the trajectory, $B_N(h; z_0)$, converges to its space average

$$\langle h \rangle = \int_M h \, d\mu$$

for $N \rightarrow \infty$, where μ is an invariant measure over the trajectory. The Birkhoff average, however, does not have a fast convergence to the space average. For a chaotic orbit the convergence rate of (4.1) is $N^{-1/2}$, and N^{-1} for the quasiperiodic case. The slow convergence of (4.1) for quasiperiodic orbits is due to the lack of smoothness at the ends of the orbit. It is possible

to improve this convergence by considering small weights to the terms when n is near 0 and N instead of weighting the terms $h(f^n(z_0))$ in the average equally. Thus, we add a weighting function g , normalized as such

$$\sum_{n=0}^{N-1} g\left(\frac{n}{N}\right) = 1, \quad (4.2)$$

that vanishes at the beginning and end of the orbit and we introduce the weighted Birkhoff average as

$$WB_N(h; z_0) = \sum_{n=0}^{N-1} g\left(\frac{n}{N}\right) h(f^n(z_0)). \quad (4.3)$$

If a smooth map f has a quasiperiodic orbit $\{f^n(z_0)\}$ with Diophantine rotation vector, h and g are C^∞ and $g \in \mathcal{G}_m$, where \mathcal{G}_m is the space of bump functions whose first m derivatives vanish on the boundary, then $WB_T(h; z_0)$ [Eq. (4.3)] converges to $\langle h \rangle$ (100). By choosing the smooth bump function

$$g(u) = \begin{cases} C \exp\left[-\frac{1}{u(1-u)}\right], & u \in (0, 1), \\ 0, & \text{otherwise,} \end{cases} \quad (4.4)$$

which is \mathcal{G}_∞ and C is the normalization constant to satisfy (4.2), $WB_N(h; z_0)$ converges to the space average faster than any power of N (see Theorems 1.1 and 3.1 in Ref. (64)). The weighted Birkhoff average, however, does not improve the convergence rate of chaotic orbits.

Therefore, it is possible to distinguish between regular and chaotic dynamics in maps¹ by examining the convergence rate of $WB_N(h; z_0)$ to $\langle h \rangle$ as $N \rightarrow \infty$ (62, 63, 65, 66) by comparing the value of $WB_N(h; z_0)$ along the first N iterates with $WB_N(h; f^N(z_0))$ along the second N iterates. In the limit $N \rightarrow \infty$ these values should be equal and we measure the convergence rate by computing the number of zeros after the decimal point by defining

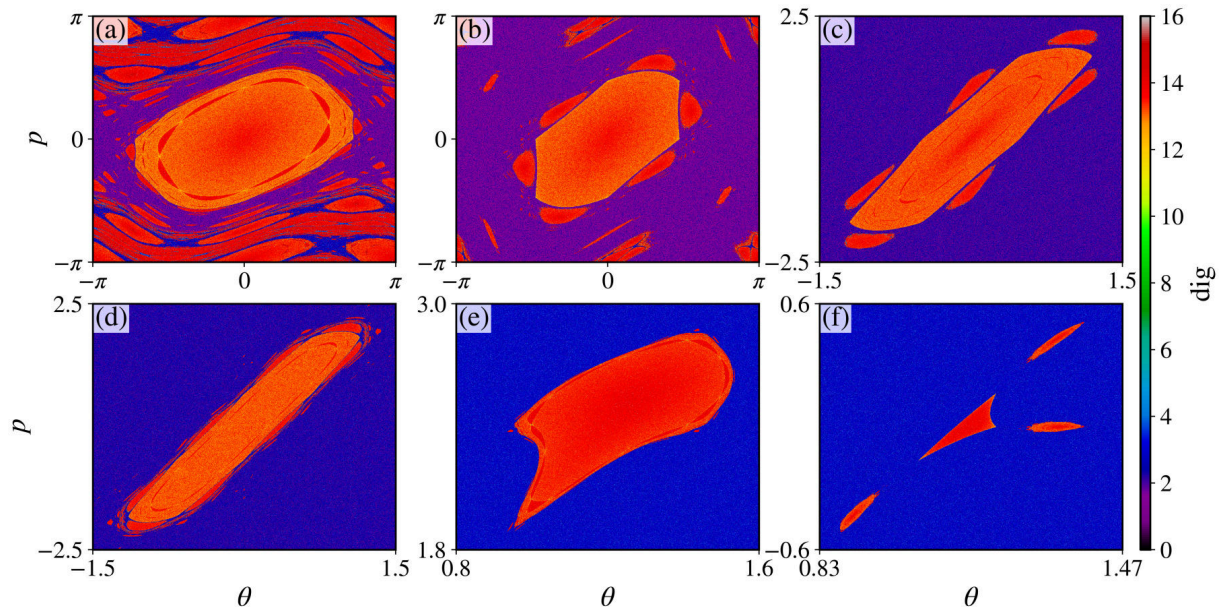
$$\text{dig} = -\log_{10} |WB_N(h; z_0) - WB_N(h; f^N(z_0))|. \quad (4.5)$$

If dig is large, the convergence is fast and the orbit is regular. If dig is small, the orbit is chaotic. However, a smaller value of dig (e.g. $\text{dig} = 1$) does not imply that this orbit is “more chaotic” than an orbit with a larger value of dig (e.g. $\text{dig} = 3$). It seems that there is a correlation with the area of the chaotic component, but the relation is not as clear as it is with the Lyapunov exponents (91). Also, note that the total number of iterates necessary to compute (4.5) is $2N$.

In Figure 4.1 is shown the value of dig for a grid of 1000×1000 initial conditions uniformly distributed in the depicted regions in the phase space of the standard map (3.3) for six distinct values of k . The total iteration time is $2N = 2.0 \times 10^6$ and $h(\theta, p) = \cos \theta$. The regular islands are represented by a red color, while the chaotic regions by purple/blue. We observe a clear distinction between them by looking at the histograms of the values of dig of Figure 4.1 (Figure 4.2). There are mainly two peaks in the distribution. The one centered around $\text{dig} \sim 2.5$

¹ Recently, this methodology has been extended to the case of flows (67).

Figure 4.1: The number of zeros after the decimal point of the convergence of the weighted Birkhoff average, dig [Eq. (4.5)], for a grid of 1000×1000 uniformly distributed initial conditions in the phase space region depicted of the standard map (3.3), with (a) $k = 0.9$, (b) $k = 1.5$, (c) $k = 3.93$, (d) $k = 4.0$, (e) $k = 5.3$, and (f) $k = 6.908745$. The total iteration time is $2N = 2.0 \times 10^6$, and $h(\theta, p) = \cos \theta$. The regular regions are characterized by high values of dig (red), while the chaotic ones by small values of dig (blue).

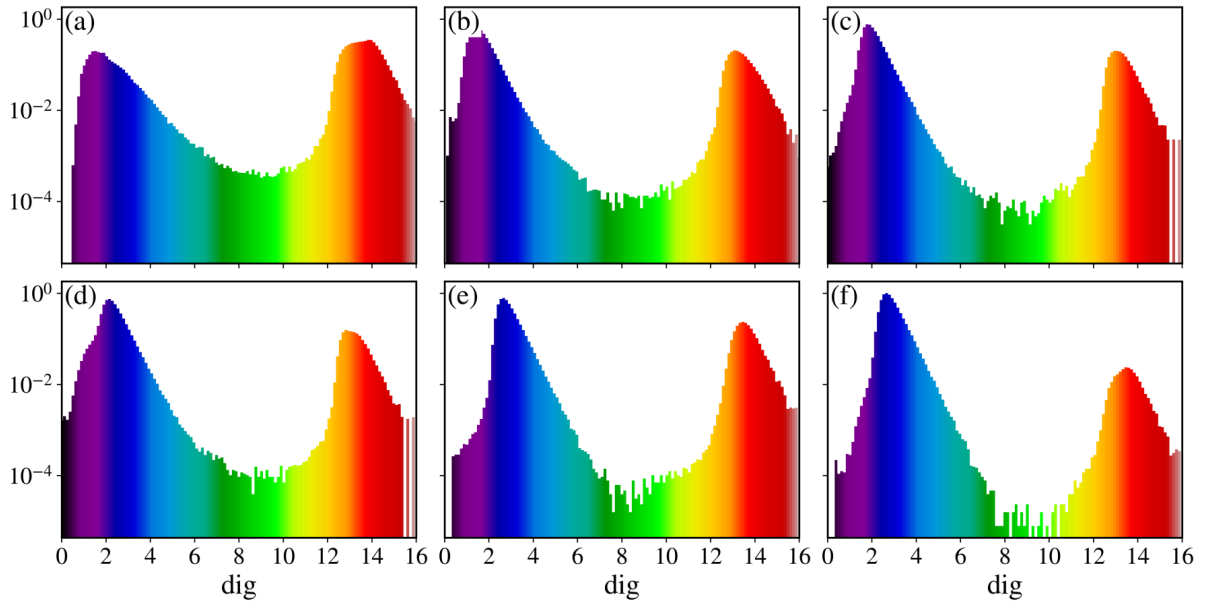


Source: the author.

corresponds to the chaotic orbits while the regular ones are centered around $\text{dig} \sim 14$. Although they occur less often, there are also orbits with intermediate values of dig . These are trapped orbits whose value of dig has not yet converged to its asymptotic value. The specific choice of the function h is arbitrary at some level, given that it satisfies the requirements of Theorems 1.1 and 3.1 of Ref. (64). Here, we use $h(\theta, p) = \cos \theta$, the same function used in Ref. (65) to compare the weighted Birkhoff average method with the Lyapunov exponents and the 0-1 test. However, other functions have also been used. In Ref. (62) the authors used $h(\theta, p) = \sin(\theta + p)$ to demonstrate the method for the standard map, and in Ref. (66), Meiss and Sander used the frequency map of a three-dimensional analog of the standard map as the function h .

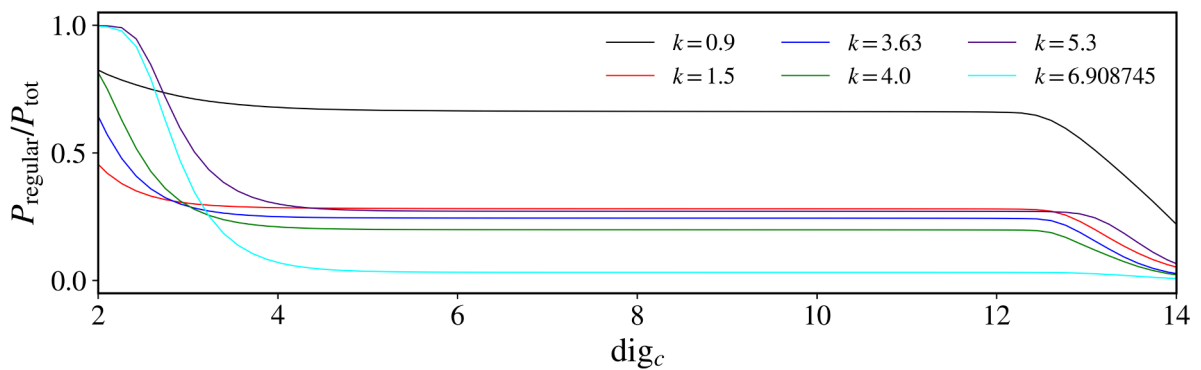
By the definition of the Lyapunov exponents, we say an orbit is chaotic if at least one exponent is greater than zero. However, in numerical simulations, we define a small cutoff value to distinguish between regular and chaotic orbits. When using the weighted Birkhoff average method we also need to define such a value. Meiss and Sander (66) also addressed this problem. Based on our analysis of the histograms of dig (Figure 4.2), we choose $\text{dig}_c = 11.25$ as the cutoff value above which the orbits are regular. We choose a large value in order to be conservative in classifying orbits as regular, since trapped orbits show intermediate values of dig but are, in fact, chaotic. Furthermore, because the number of orbits with intermediate values is small compared to regular and chaotic ones, no significant changes occur for small changes in the cutoff value.

Figure 4.2: Histograms of the values of dig shown in Figure 4.1. There are mainly two peaks, each one characterizing one dynamical regime. The peak for small values of dig corresponds to chaotic orbits, while the peak for larger values of dig to regular orbits. There are orbits with an intermediate value of dig , and they are trapped orbits whose value of dig has yet not converged its asymptotic value. We note that as k increases, the proportion of regular orbits diminishes, as expected.



Source: the author.

Figure 4.3: The normalized proportion of regular orbits as a function of the cutoff value dig_c for the data in Figures 4.1 and 4.2. For small and large values of dig , the proportion changes significantly, however, there is an interval around $\text{dig}_c \in [5, 12]$ in which the proportion is almost constant.



Source: the author.

In fact, there is a whole interval of the cutoff value in which the distinction remains accurate (Figure 4.3).

4.2 FRACTAL DIMENSION AND UNCERTAINTY EXPONENT

Therefore, the method just described is an efficient method for distinguishing chaos and regularity, however, the exact boundary between these two regimes is extremely hard to determine. Due to the presence of the islands, the chaotic sea constitutes a fat fractal (21), and it is widely known that fractal structures are present in a variety of dynamical systems, ranging from dissipative (101–104) to Hamiltonian systems (105–108). There are many definitions of the dimension d of a boundary. The most commonly used is called the capacity or box-counting dimension and is defined as

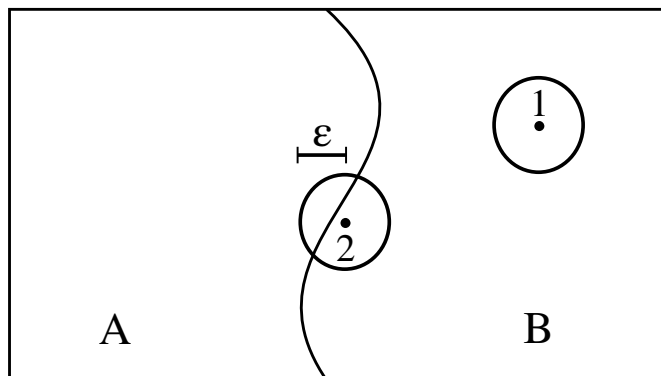
$$d = \lim_{\delta \rightarrow 0} \frac{\ln N(\delta)}{\ln 1/\delta}, \quad (4.6)$$

where $N(\delta)$ is the minimum number of D -dimensional boxes of length δ required to cover the boundary. For smooth boundaries, d equals the phase space dimension, D , and we say a boundary is fractal if $d < D$.

Typically, a nonlinear system exhibits multiple final states (*e.g.* multiple attractors in dissipative systems or the coexistence of chaos and regularity in Hamiltonian systems). In such cases, the final state might depend on the initial state of the system. For example, in Figure 4.4 is exemplified the case of two different final states, denoted by A and B. Initial conditions on the left (right) of the boundary will asymptotically go to the final state A (B). However, if the initial conditions are known with an uncertainty of ε , it is not possible to say to which final state the initial state belongs. In Figure 4.4, points 1 and 2 represent initial conditions known with an uncertainty ε . We can say for sure that the orbit generated by initial condition 1 belongs to the final state B. However, the orbit generated by initial condition 2 may belong to either A or B. In this sense, we say that initial condition 2 is uncertain.

Now, let us consider the fraction of all uncertain initial conditions within the phase space region shown in Figure 4.4. We denote this fraction $f(\varepsilon)$, and we clearly have $f(\varepsilon) \sim \varepsilon$, *i.e.*, a

Figure 4.4: A region in phase space with two different final states, A and B, divided by the boundary. A and B can represent either two different attractors or the boundary of an island. Points 1 and 2 are initial conditions with uncertainty ε .



Source: adapted from Figure 1 of Ref. (101).

reduction in the uncertainty of the initial condition corresponds to a proportional reduction in the uncertainty of the final state measured by $f(\varepsilon)$. This is the case of smooth boundaries. This, however, is not the case for several nonlinear systems (109). When the boundaries are fractal, the uncertainty fraction is expected to scale with ε as a power law (101–103),

$$f(\varepsilon) \sim \varepsilon^\alpha, \quad (4.7)$$

and we say that there is final state sensibility. In such a case, a great reduction in the uncertainty of the initial condition uncertainty yields only a small decrease in the uncertainty of the final state. In other words, in order to reduce the uncertainty of the final state, it may be necessary a considerable reduction in the initial condition uncertainty ε . In (4.7) $\alpha \leq 1$ is the uncertainty exponent, and it is possible to relate it to the box-counting dimension (4.6). The definition (4.6) simply points out that

$$N(\delta) \sim \delta^{-d}. \quad (4.8)$$

By setting $\delta \equiv \varepsilon$, the volume of the uncertain region on the phase space is given by $N(\varepsilon)\varepsilon^D$, where ε^D is the volume of boxes. Thus, from (4.8), the uncertain phase space volume is estimated to be $N(\varepsilon)\varepsilon^D \sim \varepsilon^{D-d}$. Therefore, the uncertainty exponent is (102)

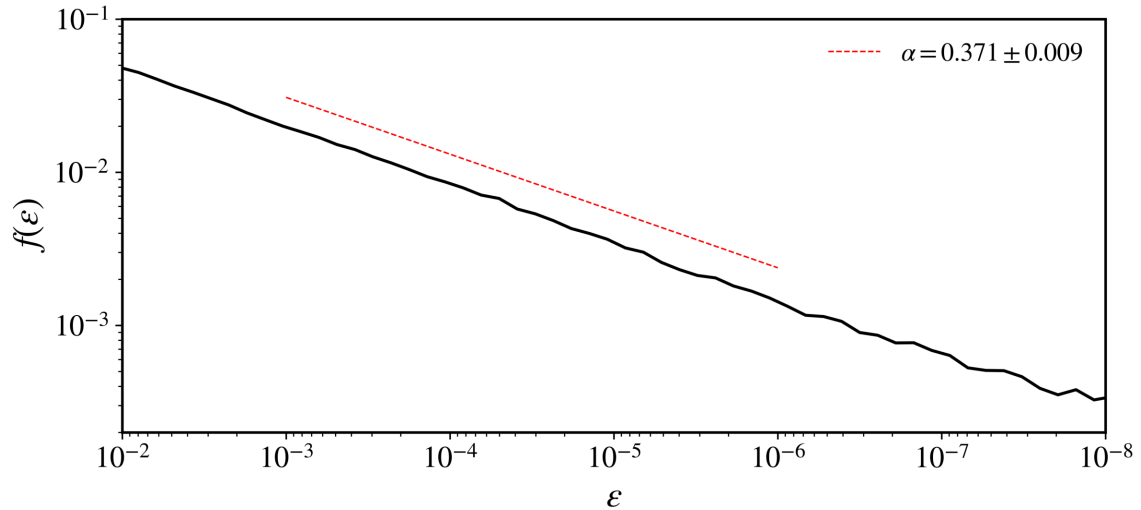
$$\alpha = D - d. \quad (4.9)$$

In our case, the phase space dimension is $D = 2$, such that a smooth boundary is characterized by $\alpha = 1$, since $d = 1$ in this case, whereas a fractal boundary is characterized by $\alpha \in (0, 1)$.

To numerically estimate the uncertainty exponent, we consider a large number of randomly chosen initial conditions (θ_0, p_0) . For each initial condition, we estimate the final state of the system, which in our case means the evaluation of dig [Eq. (4.5)] with total iteration time $2N = 2 \times 10^6$ and $h(\theta, p) = \cos \theta$. We check whether dig is larger or not than the cutoff value. If so, we say the initial condition is regular, *i.e.*, is inside of an island. If not so, the orbit lies in the chaotic sea. We then perturb each initial condition in the θ direction by $\pm\varepsilon$ to produce two new initial conditions $(\theta_0 \pm \varepsilon, p_0)$, and evaluate dig for these two new initial conditions. If either of the two perturbed initial conditions has a different result, we say the original initial condition is uncertain. The uncertainty fraction, $f(\varepsilon)$, is the ratio between the number of uncertain initial conditions and the total number of them. We repeat this computation ten times with 5.0×10^4 initial conditions for each value of ε , which we change from 10^{-2} to 10^{-8} . We compute the uncertainty exponent for each one of the ten computations and take its mean and standard deviation: $\alpha = \bar{\alpha} \pm \sigma_\alpha$. The uncertainty exponent can be estimated from the slope in the $\log f(\varepsilon)$ - $\log \varepsilon$ plot (Figure 4.5). For $k = 4.0$ we obtain an exponent of $\alpha = 0.371 \pm 0.009$, and a dimension of $d = 1.629 \pm 0.009$.

Now, suppose we wish to decrease by half the uncertainty of the measurement, *i.e.*, suppose

Figure 4.5: The uncertainty fraction as a function of ε for the phase space region depicted in Figure 4.1(d) with $k = 4.0$. We observe a power law dependence with exponent $\alpha = 0.371 \pm 0.009$. We chose 5.0×10^4 random initial conditions for each value of ε , and we performed this simulation ten times. We computed the uncertainty exponent for each one of the ten simulations and took its mean and standard deviation: $\alpha = \bar{\alpha} \pm \sigma_\alpha$.



Source: the author.

$f'(\varepsilon') = f(\varepsilon)/2$. Then

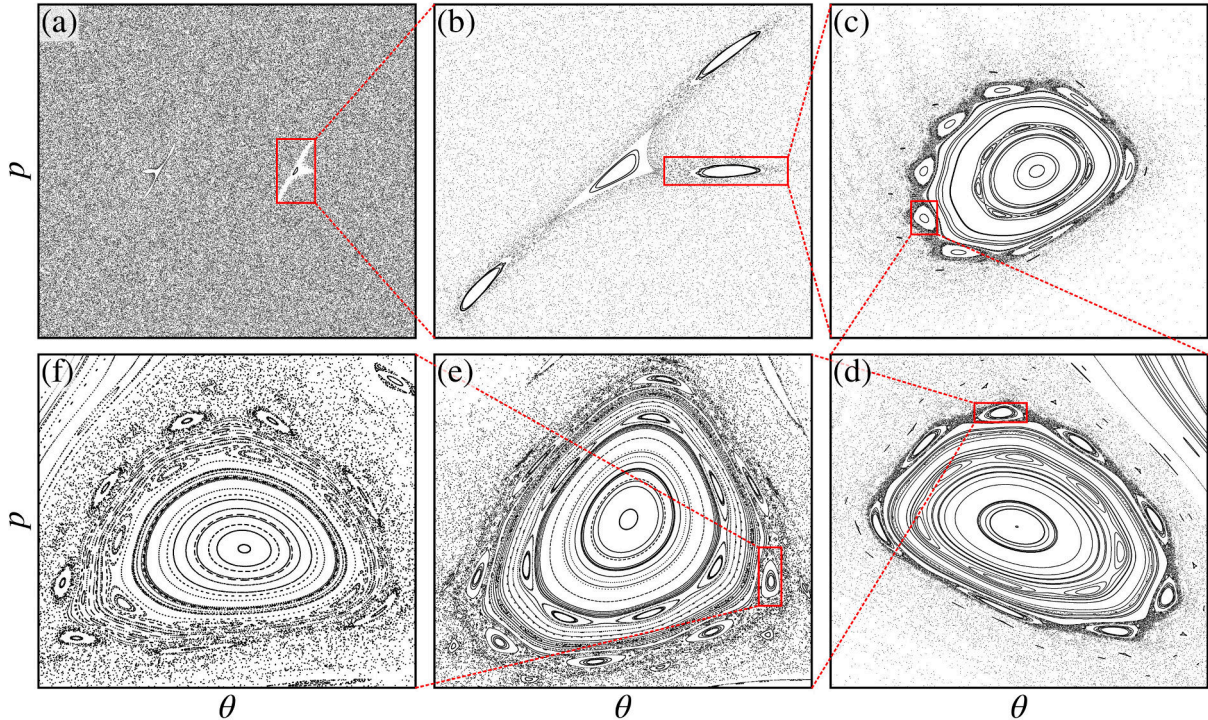
$$\begin{aligned} (\varepsilon')^\alpha &= \frac{1}{2} \varepsilon^\alpha, \\ \alpha \log \varepsilon' &= \log \frac{1}{2} + \alpha \log \varepsilon, \\ \log \varepsilon' &= \log \left(\frac{1}{2} \right)^{1/\alpha} + \log \varepsilon, \\ \varepsilon' &= 2^{-1/\alpha} \varepsilon. \end{aligned}$$

In words, in order to decrease by half the uncertainty of the measurement, it would be necessary to improve the quality of the measurement, *i.e.*, the uncertainty in the initial condition, by a factor of $2^{1/\alpha}$. In the case of the standard map with $k = 4.0$ (Figures 4.1(d) and 4.5), this factor would be of $2^{1/0.371} \approx 6.5$. Therefore, fractal boundaries impose an obstruction to predictability in the sense that in order to obtain the desired uncertainty in a measurement, it is necessary a considerable reduction in the “error” of the measurement.

4.3 EFFECTIVE FRACTAL DIMENSION

The origin of the fractality of phase space in two-dimension Hamiltonian systems lies in the coexistence of chaotic and regular domains. As we have mentioned in Chapter 2, the phase space of a typical Hamiltonian system exhibits a complex structure of islands-around-islands embedded in the chaotic sea. This structure repeats itself for arbitrarily small scales. For particular

Figure 4.6: The phase space of the standard map with $k = 6.908745$ for 100 randomly chosen initial conditions distributed (a) in the entire phase space $[-\pi, \pi] \times [-\pi, \pi]$ and (b)-(f) in the regions delimited by the first five rows of Table 4.1. Figures (b)-(f) are magnifications around the islands marked by a red box.



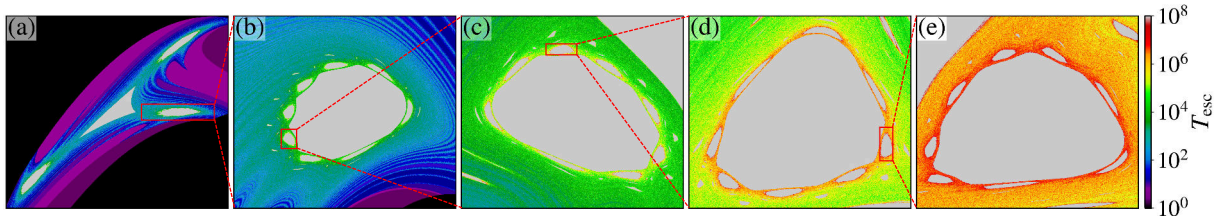
Source: the author.

values of the nonlinearity parameter k , the structure of islands-around-islands in the standard map assumes a self-similar character (46, 47, 88, 99, 99, 110). This structure is related to the accelerator modes and it is the origin of anomalous transport (46) together with local topological properties of the phase space near the islands. By introducing a renormalization group transform (47, 87) it is possible to define scaling constants of the island chain. Benkadda *et al.* (99) and Zaslavsky *et al.* (88) obtained such scaling constants for the area and period of the islands in the chain for the standard map with $k = 6.476939$ and $k = 6.908745$, respectively. They computed the area and period of each island in the chain, and showed that there is a rule that relates these quantities of the n th generation island and the next:

$$\begin{aligned} S_{n+1} &= \lambda_S S_n, \\ T_{n+1} &= \lambda_T T_n. \end{aligned} \tag{4.10}$$

In order to determine the self-similar structure, we choose $k = 6.908745$ and consider 100 randomly chosen initial conditions in the entire phase space $[-\pi, \pi] \times [-\pi, \pi]$ [Figure 4.6(a)]. For this value of k there are two sets of islands, and each of these sets are composed of a main island surrounded by three other islands [Figure 4.6(b)]. By continuously magnifying the re-

Figure 4.7: The escape time for a grid of 1000×1000 uniformly distributed initial conditions in the regions given in Table 4.1 for the standard map with $k = 6.908745$. Figures (b)-(e) are magnifications around the indicated islands and the color bar is in logarithmic scale.



Source: the author.

regions denoted by the red box in Figure 4.6 and defined by the first five rows of Table 4.1, and considering 100 randomly chosen initial conditions in each one of these regions, we can observe the self-similar structure reported by Zaslavsky *et al.* (88). The sequence of islands generated by $k = 6.908745$ is 1–3–8–8–8, which means that the central island (1) is surrounded by three other islands (3) and each one of these islands is surrounded by eight islands (8) and so on. We label this sequence as (g, q) , where g represents the order of generation and q is the number of islands of the g th generation. In Figure 4.6(d), for example, we have $(g, q) = (2, 8)$. These structures are also revealed by counting the time required (escape time) for an orbit to escape the region depicted in Figure 4.6(b) (first row of Table 4.1). We consider 1000×1000 uniformly distributed initial conditions in a grid for each of the regions specified in Table 4.1 and count their escape time (Figure 4.7). The regular orbits remain for all times inside the region (gray color) and the not-trapped chaotic orbits leave the region after a few iterations (black to blue color). The intermediate values of T_{esc} correspond to trapped orbits and the magnifications in Figures 4.7(b)-(e) show the stickiness structures and the self-similar hierarchy of the island chain. Note that the smaller the scale, the longer it takes for the orbits to escape.

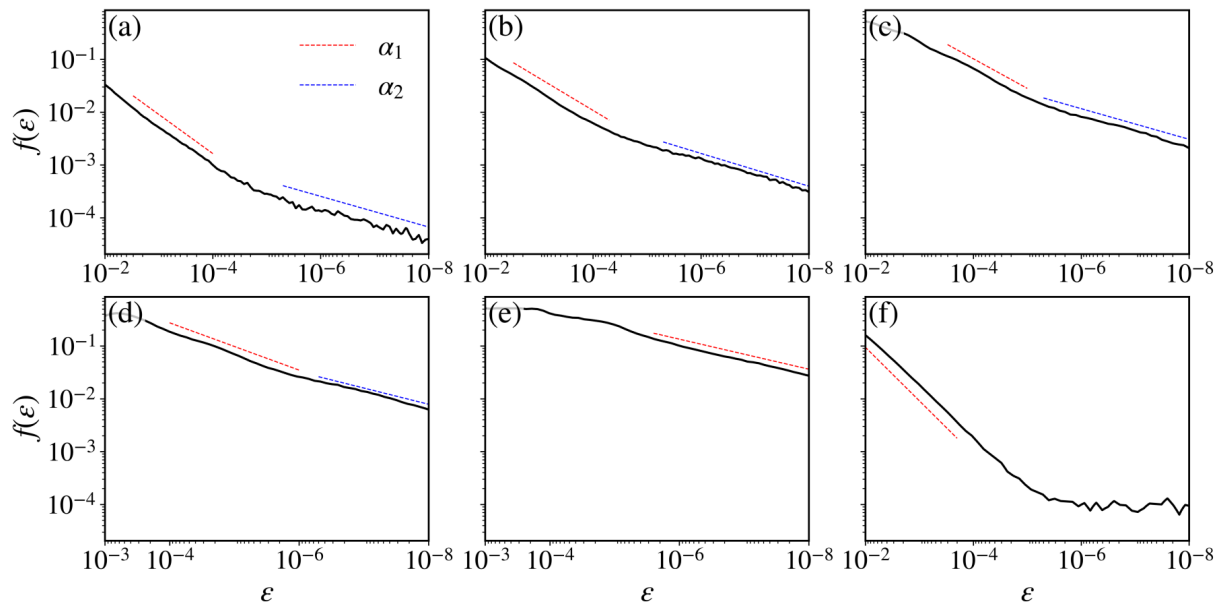
We now compute the uncertainty exponent for the island chain shown in Figure 4.7. We proceed in the same way as for $k = 4.0$. We consider 5.0×10^4 randomly chosen initial conditions

Table 4.1: The first five rows corresponds to the phase space regions shown in Figures 4.6(b)-(f) and 4.7 given by $\{\theta, p \mid \theta_0 \geq \theta \geq \theta_1, p_0 \geq p \geq p_1\}$. The last row corresponds to the phase space region around the central island in 4.6(b) and 4.7(a).

θ_0	θ_1	p_0	p_1
0.83	1.47	-0.6	0.6
1.22	1.43	-0.05	0.05
1.2650	1.2794	-0.019	-0.009
1.2705	1.2725	-0.011 03	-0.010 46
1.272 22	1.272 34	-0.010 89	-0.010 79
1.0314	1.218 61	-0.1908	0.1908

Source: the author.

Figure 4.8: The uncertainty fraction as a function of ε for (a)-(e) the phase space regions shown in Figure 4.7 and given by Table 4.1 and (f) for the region around the central island in Figure 4.7(a) given by the last row of Table 4.1. We observe a power law dependence, however, now it is possible to associate different exponents with different intervals of ε . We choose 5.0×10^4 random initial conditions for each value of ε , and we perform these simulations twenty-five times for (a) and (b) and ten times for (c)-(f). We compute the uncertainty exponent for each one of these simulations and take its mean and standard deviation: $\alpha = \bar{\alpha} \pm \sigma_\alpha$.



Source: the author.

for each value of ε , which we vary from 10^{-2} to 10^{-8} for the first three regions [(a)-(c)] and from 10^{-3} to 10^{-8} for the remaining two [(d) and (e)]. For each uncertain initial condition, we also count the escape time, T_{esc} . We repeat these computations twenty-five times for (a) and (b) and then times for (c)-(e), and we estimate the uncertainty exponent for each one of these computations and take its mean and standard deviation: $\alpha = \bar{\alpha} \pm \sigma_\alpha$ (Table 4.2). The logarithmic plots of $f(\varepsilon)$ are shown in Figure 4.8. The power law dependence is again evident, however, unlike the previous case (Figure 4.5), we can now associate different exponents with different intervals of ε [except for Figure 4.8(e)], and we evaluate the mean escape time, $\langle T_{\text{esc}} \rangle$, for each one of these intervals (Table 4.2).

We observe a very similar behavior of $f(\varepsilon)$ for regions (a)-(d). There are two decay rates in these cases, given by the exponents α_1 and α_2 , where $\alpha_1 > \alpha_2$. Figure 4.8(e) shows that for values of ε in the range of $10^{-3} \gtrsim \varepsilon \gtrsim 10^{-5}$, the function $f(\varepsilon)$ does not follow a power law. This behavior can be attributed to the fact that, in this scenario, the size of the island is comparable to the scale of ε . Consequently, numerous false positive uncertain initial conditions arise, leading to a deviation from the expected power law. This observation holds true for all deviations from the power law decay when ε takes large values, as exemplified in Figure 4.8(c) for $10^{-2} \gtrsim \varepsilon \gtrsim 10^{-3}$. The presence of distinct exponents, and therefore different dimensions (Table 4.2), for different intervals of ε indicates the existence of an effective fractal dimension (111, 112) that depends on

Table 4.2: The uncertainty exponent α , the dimension d , and the mean escape time $\langle T_{\text{esc}} \rangle$ of the phase space regions shown in Figure 4.7 and given by Table 4.1.

Fig. 4.7	α_1	d_1	$\langle T_{\text{esc}}^{(1)} \rangle$	α_2	d_2	$\langle T_{\text{esc}}^{(2)} \rangle$
(a)	0.74 ± 0.01	1.26	2.8×10^4	0.29 ± 0.06	1.71	1.2×10^6
(b)	0.611 ± 0.005	1.398	1.5×10^5	0.31 ± 0.03	1.69	1.6×10^6
(c)	0.561 ± 0.008	1.439	5.3×10^5	0.29 ± 0.02	1.71	1.6×10^6
(d)	0.448 ± 0.004	1.552	1.9×10^6	0.307 ± 0.004	1.693	2.7×10^6
(e)	0.284 ± 0.002	1.716	7.3×10^6	—	—	—

Source: the author.

the scale of the initial condition uncertainty. In other words, at scale ε_1^* , the system exhibits a fractal dimension of $d(\varepsilon_1^*) = d_1$, while at scale ε_2^* , the system behaves as if the fractal dimension is $d(\varepsilon_2^*) = d_2$, and so on. Thus, at various scales ε_i^* , the island boundary demonstrates an effective fractal dimension of $d(\varepsilon_i^*) = d_i$, which differs from the asymptotic value reached as ε approaches zero. In the specified range of ε , the observed dimension remains small for large ε values, until it abruptly becomes larger for small ε values.

The uncertainty of the initial conditions, ε , can be related to the resolution of a measuring device. And as fractal boundaries introduce unpredictability in the system, we can argue that in order to enhance our ability to predict whether an initial condition is regular or chaotic, we may need to amplify the experimental accuracy by a larger factor that depends on the scale of resolution. Let us consider the island depicted in Figure 4.7(b) as an example. If the apparatus has an accuracy of 10^{-4} and we aim to improve the predictive capability regarding the regularity or chaos of the initial condition by a factor of 2, the accuracy needs to be increased by $2^{1/0.611} \approx 3.1$. On the other hand, if the apparatus has a resolution of 10^{-7} , the required improvement in accuracy would be $2^{1/0.31} \approx 9.4$. Therefore, at realistic length scales, the uncertainty of the measurement is not determined by the asymptotic fractal dimension, but rather by the effective fractal dimension (112). Beyond the dependence on the scale, the effective fractal dimension also depends on the position in phase space. By performing the same procedure for the calculation of the uncertainty fraction for the region around the central island (last row of Table 4.1), which is surrounded by the period-3 islands, of Figure 4.7(a), we obtain an exponent of $\alpha = 0.987 \pm 0.009$ for $10^{-2} \leq \varepsilon \leq 10^{-5}$ [Figure 4.8(f)]. This results in a dimension of $d = 1.013 \pm 0.009$, which is clearly different from the dimension of the period-3 islands. A similar result was found for the dimension of the stable and unstable manifolds (111–113). The dimension for the central island corresponds to a smooth boundary (within numerical errors), and it corroborates the previous statement that the fractality is due to the hierarchy of islands-around-islands. In the chosen region, there is no such hierarchy. Furthermore, for $\varepsilon < 10^{-5}$ we observe a zero uncertainty exponent, which corresponds to a riddle boundary (114), *i.e.*, for scales smaller than approximately 10^{-5} , a reduction in the initial condition uncertainty does not

reduce the uncertainty in the final state.

Moreover, the order of generation of the island chain also influences the dimension of the boundary. As we go deep into the self-similar structure, *i.e.*, increase g , the dimension for larger values of ε , d_1 , increases whereas the second dimension remains constant (within numerical errors). Besides, there is a tendency of d_1 towards d_2 for increasing g , until $g = 4$ is reached and only one dimension is present for the specified interval of ε . The dependency of the dimension on the order of generation is due to the complex hierarchical structure of the island chain and *cantori*. The inner we go into this structure, the longer the orbits stay inside *cantori*, leading to very long escape times (Figure 4.7 and $\langle T_{\text{esc}} \rangle$ in Table 4.2). These extremely long times impose difficulty in the prediction of the final state, hence the dimension of the inner levels is larger (111). A similar result was found in Ref. (113) for the dynamics of a two-dimensional advection of a flow. Furthermore, the dimension and mean escape time for the second power law regime do not change significantly. This is so because at that scale of ε we are actually measuring an inner, finer level of the self-similar hierarchy. Followed by that, we expect that by decreasing even more the uncertainty in the initial conditions, more power law regimes with different exponents will be found, bounded, of course, to the value of $\alpha > 0$, and $d < D$.

5 CHARACTERIZATION OF STICKINESS USING RECURRENCE PLOTS

In this chapter, we present a brief review on the basics of recurrence plots (RPs) and their quantification analysis. For a detailed discussion on all the features of the recurrence plot and its quantification analysis, we refer the reader to Refs. (72–76) and references therein. We present the different patterns the graphical visualization of RPs can exhibit, and we define some of the most used quantification measures of RPs. We also introduce the little-known Slater’s theorem, and relate it to the recurrence time entropy. We illustrate all of these quantification measures using the standard map [Eq. (3.3)] for different parameter values. We then compute the Pearson correlation coefficient between these measures and the largest Lyapunov exponent, λ_1 , in order to find the optimal RP-based measure for chaotic detection. Motivated by Slater’s theorem, we choose the recurrence time entropy (RTE) as our mathematical tool for dynamical characterization, and we perform a similar approach as for the finite-time Lyapunov exponent (FTLE) in Section 3.2 to obtain the probability distribution of finite-time RTE. We use this distribution to identify the specific areas in phase space that correspond to the modes of the distribution and we compute the cumulative distribution of the trapping times in each one of these regions.

5.1 RECURRENCE PLOT

5.1.1 Definition

The state of a dynamical system in a d -dimensional phase space can be specified by d state variables in the form of a vector

$$\mathbf{x}(t) = (x_1(t), x_2(t), \dots, x_d(t))^T. \quad (5.1)$$

Usually, there is a time-evolution law that determines the state of the system at each instant of time t given the state at any particular moment. For Hamiltonian systems, for example, this law is given by Hamilton’s equations (2.1). More generally, for time-continuous systems, the time-evolution law is given by a set of differential equations

$$\frac{d\mathbf{x}(t)}{dt} = \mathbf{F}(\mathbf{x}(t)), \quad (5.2)$$

where $\mathbf{F} : \mathbb{R}^d \rightarrow \mathbb{R}^d$. If \mathbf{F} is known, it is possible to integrate (5.2), either analytically or numerically, to obtain the trajectory $\mathbf{x}(t)$ in phase space. For discrete systems, the time-evolution law is given by a mapping

$$\mathbf{x}_{n+1} = \mathbf{M}(\mathbf{x}_n) = \mathbf{M}^n(\mathbf{x}_0), \quad (5.3)$$

where $\mathbf{M} : \mathbb{R}^d \rightarrow \mathbb{R}^d$ and the future of the system, \mathbf{x}_{n+1} , is uniquely determined by an initial state \mathbf{x}_0 . The standard map (3.3) is an example of such a system.

The recurrence plot (RP), first introduced by Eckmann *et al.* (71), is a graphical representation of the recurrences of time series of dynamical systems. High-dimensional systems are difficult to treat due to the high-dimensionality of phase space, and the original idea behind the RPs was to provide a mathematical and graphical tool to investigate even these high-dimensional systems. An RP allows us to analyze the d -dimensional space trajectory through a two-dimensional representation of its recurrences given by the recurrence matrix formally defined as

$$R_{ij} = H(\varepsilon - \|\mathbf{x}_i - \mathbf{x}_j\|), \quad (5.4)$$

where $i, j = 1, 2, \dots, N$, and N is the number of samples of the times series. The function $H(\cdot)$ is the Heaviside unit step function, ε is a small threshold, and $\|\mathbf{x}_i - \mathbf{x}_j\|$ is the spatial distance in phase space between two states, \mathbf{x}_i and \mathbf{x}_j , in terms of a suitable norm. A class of vector norms that is generally used is the p -norm, defined as

$$\|\mathbf{x}\|_p = \left(\sum_{i=1}^n |x_i|^p \right)^{1/p}. \quad (5.5)$$

For $p = 1$, we obtain the taxicab (or Manhattan) norm, and $p = 2$ corresponds to the traditional Euclidean norm. As p approaches infinity, the p -norm approaches the maximum (or supremum) norm

$$\|\mathbf{x}\|_\infty = \max_i (|x_i|), \quad (5.6)$$

which corresponds to choosing the maximum of all components of \mathbf{x} . Throughout this chapter, unless mentioned otherwise, we consider the maximum norm (5.6). This norm is more often used because it is computationally faster to compute, it is independent of the phase space dimension, and it allows some analytical results (115).

The recurrence matrix \mathbf{R} is a binary matrix that contains the value 1 for recurrent states and the value 0 for non-recurrent ones. Since $R_{ii} \equiv 1$ by definition, the RP always exhibits a main diagonal line, called line of identity (LOI), and the RP, for fixed ε , is symmetric with respect to this line. Since it is often impossible to find exact recurrent states in the sense that $\mathbf{x}_i \equiv \mathbf{x}_j$, the recurrence of two states is defined as they are sufficiently close to each other up to a distance ε . This statement is expressed by the Heaviside function in (5.4). A special parameter of the RP is the threshold ε . Regardless of the used norm, this parameter has to be chosen carefully. If ε is chosen too large, almost every point is recurrent with every other point. On the other hand, if ε is chosen too small, there will be almost no recurrent states, and we cannot learn anything from the RP. Hence the choice of ε has to be a compromise between having ε as small as possible, but at the same time with a sufficient number of recurrent states.

Several ‘‘rules of thumb’’ have been proposed to this day in the literature. However, in general, the optimal choice of ε depends on the application and the experimental conditions. Initially, it was thought that the optimal choice would be to consider ε as a few percent of the mean

or maximum phase space diameter (116), without exceeding 10% (117). However, the influence of noise may demand a larger threshold. An alternative is to choose ε such that the recurrence point density, *i.e.*, the recurrence rate, is fixed (118). This would introduce the need of finding the optimal value of the recurrence rate, though. A further possibility, introduced to analyze processes with noise (72, 115), is to choose ε as five times larger than the standard deviation of the observational noise. A more recent study has shown that using $\varepsilon \rightarrow 0$ is not the best choice either (119). Thus, all approaches have their strengths and weakness, and regardless of the choice we make, the effect of a finite ε will always be present. Therefore, in our analysis, we follow a similar approach to Refs. (72, 115), and consider the threshold to be 10% of the time series standard deviation, *i.e.*, $\varepsilon = \sigma/10$. Regarding the calculation of the standard deviation, when dealing with d -dimension data, the problem of how to calculate its standard deviation arises. The simplest approach one could consider is (i) to concatenate the time series of each component, creating a new dN -dimensional vector

$$(x_1^{(1)}, x_2^{(1)}, \dots, x_N^{(1)}, x_1^{(2)}, x_2^{(2)}, \dots, x_N^{(2)}, \dots, x_1^{(d)}, x_2^{(d)}, \dots, x_N^{(d)})^T,$$

where N is the time series length, and compute its standard deviation. Another approach one could choose is (ii) to consider a standard deviation vector, $\boldsymbol{\sigma}$, where each component is the standard deviation of each component of the time series individually, and compute its norm. Here, we consider approach (ii) because choosing approach (i) when one time series has a different value range than the others might strongly bias the standard deviation. Furthermore, we consider the maximum norm (5.6). The influence of ε on our results will be discussed later on in this chapter.

5.1.2 Structures in a Recurrence Plot

As we have previously mentioned, the RP is a graphical tool to visualize phase space trajectories. We represent the recurrent states by a colored dot, and the recurrence matrix \mathbf{R} displays different patterns according to the dynamics of the underlying system. These patterns have in their composition small-scale structures which are the basis for the quantitative analysis of RPs (72, 75). They are:

- Isolated recurrence points: they occur when the states are rare or if they do not persist for any time.
- Diagonal lines: they occur when a segment of the trajectory runs parallel to another segment for l time units, *i.e.*, when the trajectory returns to the same region of phase space at different times. Mathematically, a diagonal line of length ℓ is defined by

$$(1 - R_{i-1, j-1})(1 - R_{i+\ell, j+\ell}) \prod_{k=0}^{\ell-1} R_{i+k, j+k} = 1. \quad (5.7)$$

The diagonal lines can have two directions. The ones parallel to the LOI represent the parallel running of trajectories for the same time evolution, while the diagonal lines perpendicular to the LOI represent parallel running with opposite time direction. The lengths of diagonal lines in an RP are directly influenced by the degree of determinism or predictability inherent in the system dynamics. When a system is predictable, similar states ($R_{ij} = 1$) tend to lead to similar future states, $R_{i+1,j+1} = 1$, with a high probability. In perfectly predictable systems, the diagonal lines in the RP would be infinitely long. On the other hand, stochastic systems exhibit only single points or short lines in the RP. In such systems, close states have a very low probability of leading to a future state where $R_{i+1,j+1} = 1$. For chaotic systems, where close states diverge exponentially, the diagonal lines are very short, and the faster the divergence, the shorter the diagonals.

- Vertical lines: they mark a time length in which a state does not change or changes very slowly. Formally, a vertical line of length v is defined by

$$(1 - R_{i,j-1})(1 - R_{i,j+v}) \prod_{k=0}^{v-1} R_{i,j+k} = 1. \quad (5.8)$$

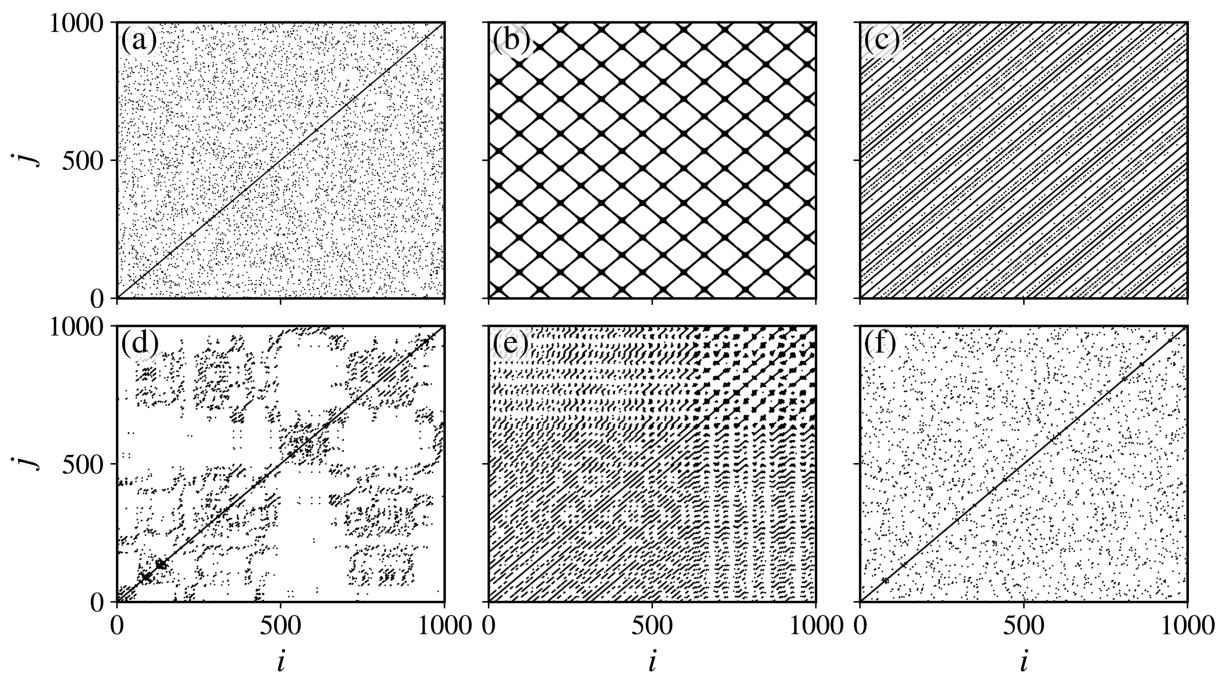
This is a typical behavior of laminar states (120) and it seems that the state is trapped for some time.

- White vertical lines: they correspond to the time it takes for the trajectory to return to a previous state, *i.e.*, they correspond to the recurrence time (69, 70, 75, 121, 122). A white vertical line of length w is defined by

$$R_{ij} R_{i,j+w} \prod_{k=0}^{w-1} (1 - R_{i,j+k}) = 1. \quad (5.9)$$

The recurrence matrices in Figure 5.1 illustrate the appearance of RPs for different dynamical processes. For uncorrelated noise [Figure 5.1(a)], there is a large number of single points with almost no line structures, while for a periodic function, all the points lie on long diagonal lines separated by a fixed distance [Figure 5.1(b)]. For the quasiperiodic dynamics, all points also lie on diagonal lines with a nonconstant distance separating them [Figure 5.1(c)]. However, there are few isolated single points. These occur due to the quasiperiodicity of the process. For longer times, these points will fill the entire diagonal. For the chaotic dynamics when there are still islands present in the phase space of the standard map ($k = 1.5$), the RP is characterized by both long and short diagonal lines organized in a non-regular way [Figure 5.1(d)]. However, this is not the case for all chaotic orbits. The RP of a sticky orbit [Figure 5.1(e)], *i.e.*, a trapped orbit which behaves similarly as a quasiperiodic but exhibit $\lambda_1 > 0$, seems to be in between the quasiperiodic [Figure 5.1(c)] and chaotic [Figure 5.1(d)] cases. The diagonal lines are longer than those in the chaotic case, indicating that the sticky orbit is “more regular” than the chaotic

Figure 5.1: Examples of recurrence matrix for different dynamical processes. (a) Uniformly distributed white noise, generated using the Numpy (123) function *random.normal* with zero mean and standard deviation equals to unity, (b) periodic dynamics, generated using a sine wave $x(t) = \sin(t)$, for $t \in [0, 50]$, (c) quasiperiodic dynamics ($\lambda_1 = 0.00014$), generated using the standard map (3.3) with $k = 1.5$, and initial condition $(\theta_0, p_0) = (1.0, 0.0)$, (d) chaotic dynamics ($\lambda_1 = 0.43214$), generated using the standard map (3.3) with $k = 1.5$ and initial condition $(\theta_0, p_0) = (2.85, 0.0)$, (e) chaotic dynamics ($\lambda_1 = 0.33276$), generated using the standard map (3.3) with $k = 1.5$ and initial condition $(\theta_0, p_0) = (1.6, 0.0)$, and (f) chaotic dynamics ($\lambda_1 = 2.18496$), generated using the standard map (3.3) with $k = 9.0$ and initial condition $(\theta_0, p_0) = (3.0, 0.0)$. The threshold is $\varepsilon = \sigma/100$ in (a) and $\varepsilon = \sigma/10$ for (b)-(f), where σ is the standard deviation of the time series. The Lyapunov exponent of (c)-(f) have been calculated considering 1.0×10^5 iterations.



Source: the author.

one, but the diagonal lines are not as long as those in the quasiperiodic case. Moreover, the vertical distances between the diagonal lines have some regularity.

5.1.3 Recurrence Quantification Analysis

Therefore, the visual representation of RPs can offer valuable insights into the dynamics of the underlying system. However, due to the user's interpretation and intuition subjectivity, only the visual representation is not enough for a complete and accurate description. About three decades ago, Zbilut and Webber introduced quantities based on the diagonal and vertical lines to quantify RPs (117, 124, 125), which is now called recurrence quantification analysis (RQA).

The simplest measure of the RQA is the recurrence rate,

$$\text{RR} = \frac{1}{N^2} \sum_{i,j=1}^N R_{ij}, \quad (5.10)$$

which is a measure of the density of recurrence points in the RP. In the limit $N \rightarrow \infty$, RR corresponds to the probability that a state recurs to its neighborhood in phase space. More complex measures are based on the line structures in the RP. The following measures are based on the histogram $P_D(\ell)$ of diagonal lines of length ℓ , defined by

$$P_D(\ell) = \sum_{i,j=1}^N (1 - R_{i-1,j-1}) (1 - R_{i+\ell,j+\ell}) \prod_{k=0}^{\ell-1} R_{i+k,j+k}. \quad (5.11)$$

Similarly to the density of recurrence points in the RP (RR), the determinism, DET, is defined as the fraction of the recurrence points that form diagonal lines of at least length ℓ_{\min}

$$\text{DET} = \frac{\sum_{\ell=\ell_{\min}}^N \ell P_D(\ell)}{\sum_{\ell=1}^N \ell P_D(\ell)}. \quad (5.12)$$

As we have seen, periodic signals are characterized by long diagonal lines (large DET), whereas chaotic dynamics is characterized mainly by short diagonal lines (small DET). For stochastic processes there are no diagonal lines, save for very short ones due to chance recurrences ($\text{DET} \approx 0$). Therefore, DET can be understood as the predictability of the process. The ratio of DET and RR has been applied to the study of physiological systems and it is useful in describing dynamical transitions since during certain transitions the RR decreases while DET remains constant (124). The variable ratio (RATIO) can be computed from

$$\text{RATIO} = N^2 \frac{\sum_{\ell=\ell_{\min}}^N \ell P_D(\ell)}{\left(\sum_{\ell=1}^N \ell P_D(\ell) \right)^2}. \quad (5.13)$$

A diagonal of length ℓ indicates that a portion of the trajectory remains near another segment of the trajectory for ℓ units of time, suggesting a connection to the divergence of these segments. The diagonal line length,

$$L = \frac{\sum_{\ell=\ell_{\min}}^N \ell P_D(\ell)}{\sum_{\ell=\ell_{\min}}^N P_D(\ell)}, \quad (5.14)$$

is the average time two segments of the trajectory stay close to each other, and it can be interpreted as the mean prediction time. Related to L is the maximal line length in the diagonal direction, L_{\max}

$$L_{\max} = \max \left(\{ \ell_i \}_{i=1}^{N_\ell} \right), \quad (5.15)$$

where N_ℓ is the total number of diagonal lines. The smaller L_{\max} the more divergent the trajectories, and a relation between L_{\max} and the largest Lyapunov exponent can be found (72). Lastly, the Shannon entropy of the frequency distribution of the diagonal lines, defined as

$$S_D = - \sum_{\ell=\ell_{\min}}^{\ell_{\max}} p_D(\ell) \ln p_D(\ell), \quad (5.16)$$

where $p_D(\ell) = P_D(\ell)/N_\ell$, reflects the complexity of the deterministic structure in the system.

Analogously to the measures based on the diagonal lines, Marwan *et al.* (120) proposed additional recurrence quantifications based on the vertical lines in the RP. These measures are based on the histogram of vertical lines of length v , defined by

$$P_V(v) = \sum_{i,j=1}^N (1 - R_{i,j-1})(1 - R_{i,j+v}) \prod_{k=0}^{v-1} R_{i,j+k}. \quad (5.17)$$

Analogous to the definition of DET [Eq. (5.12)], the density of recurrence points forming vertical structures can be computed by

$$\text{LAM} = \frac{\sum_{v=v_{\min}}^N v P_V(v)}{\sum_{v=1}^N v P_V(v)}, \quad (5.18)$$

and is called laminarity. LAM corresponds to the occurrence of laminar states and will decrease if the RP consists of more single recurrence points than vertical structures. Similarly to Eq. (5.14), the average length of vertical structures is defined as

$$\text{TT} = \frac{\sum_{v=v_{\min}}^N v P_V(v)}{\sum_{v=1}^N P_V(v)}, \quad (5.19)$$

and is called trapping time. TT is an estimate of the mean time that the system stays at a specific state or how long the state is trapped. The maximum length of the vertical structures measures the longest vertical line in the RP and is defined as [*cf.* Eq. (5.15)]

$$V_{\max} = \max \left(\{v_i\}_{i=1}^{N_v} \right), \quad (5.20)$$

where N_v is the total number of vertical lines. Lastly, the Shannon entropy of the distribution of vertical lines measures the complexity of the vertical structures in the RP and is defined by

$$S_V = - \sum_{v=v_{\min}}^{v_{\max}} p_V(v) \ln p_V(v), \quad (5.21)$$

where $p_V(v) = P_V(v)/N_v$.

We can also use the recurrence times to define measures of complexity. This is particularly

interesting due to Slater's theorem (77–79). The theorem states that for any irrational rotation, with rotation number ω , over a unit circle, there are at most three different return times to a connected interval of size $\delta < 1$. Furthermore, the third return time is always the sum of the other two, and two of these three return times are consecutive denominators in the continued fraction expansion [Eq. (2.19)] of the rotation number. Therefore, we can categorize the various solutions of a nonlinear system by simply counting the number of unique return times of an orbit. If there is only one return time, the orbit is periodic (black color in Figure 5.2); if there are exactly three returns, the orbit is considered quasiperiodic (blue color in Figure 5.2). If the number of returns exceeds three, then the orbit is deemed chaotic (cyan to gray color in Figure 5.2). This approach has been used to identify chaotic and quasiperiodic orbits in the standard map (126, 127) and, more recently, to explore the parameter space of a one-dimensional map (128). It is an effective technique, however, it is not immediately evident how to apply it to detect sticky orbits in two-dimensional quasi-integrable Hamiltonian systems, for example. Therefore, we propose using the distribution of white vertical lines, which are an estimate of the recurrence times of an orbit (69, 70, 75, 121, 122), to define the recurrence time entropy (RTE). The histogram of white vertical lines of length w , $P_w(w)$, is defined by

$$P_w(w) = \sum_{i,j=1}^N R_{ij} R_{i,j+w} \prod_{k=0}^{w-1} (1 - R_{i,j+k}), \quad (5.22)$$

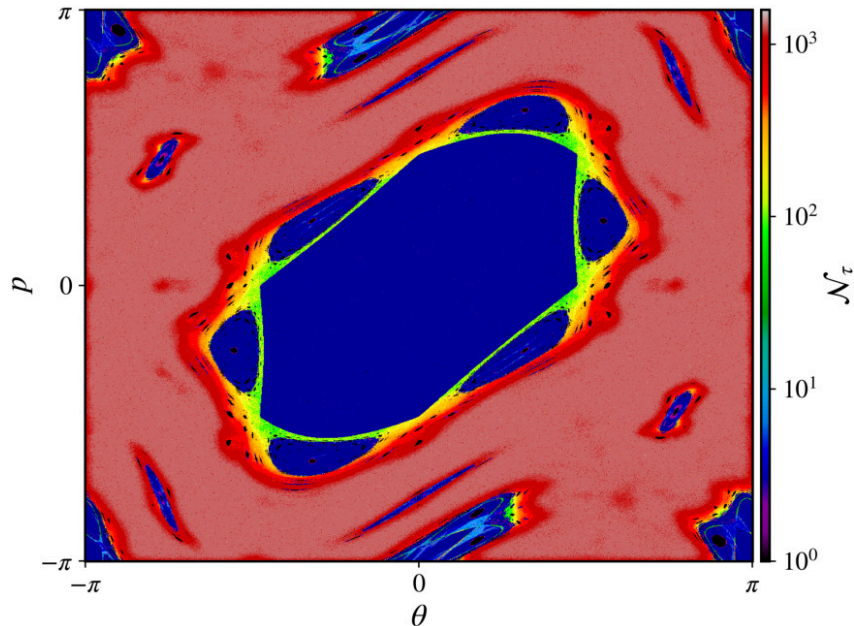
such that the RTE is defined by (68, 70)

$$\text{RTE} = - \sum_{w=w_{\min}}^{w_{\max}} p_w(w) \ln p_w(w), \quad (5.23)$$

where $p_w(w) = P_w(w)/N_w$, and N_w is the total number of white vertical lines. The RTE was originally introduced without any connection to RPs (68), and it was shown that it can provide a good estimate for the Kolmogorov-Sinai (KS) entropy (129) and the largest Lyapunov exponent (130).

It is important to evaluate (5.22) with careful attention. The presence of border lines, which are cut short by the borders of the RP, in a finite RP can introduce bias to the distribution of white vertical lines, potentially affecting RQA measures, like the RTE (131). To mitigate these border effects, we exclude white vertical lines that start and end at the RP's borders from the distribution. In this manner, a periodic orbit, which only has one return time (its own period), will result in $\text{RTE} = 0$. A quasiperiodic orbit, with three return times, will yield a relatively low RTE value, while a chaotic orbit will exhibit a high RTE value. As mentioned before, a chaotic orbit that experiences stickiness spends a significant amount of time in the vicinity of an island where its behavior resembles that of a quasiperiodic orbit. Consequently, we expect that the RTE of sticky orbits will be lower than that of chaotic orbits but higher than what would be observed for a quasiperiodic orbit.

Figure 5.2: The number of unique recurrence times, \mathcal{N}_τ , for 1000×1000 uniformly distributed initial conditions in a grid on the entire phase space $[-\pi, \pi] \times [-\pi, \pi]$ for $k = 1.5$. Each initial condition is chosen as the center of the recurrence region, with size $\varepsilon = \sigma/10$, where σ is the standard deviation of the time series generated by it. We iterate each initial condition for 2×10^6 times.



Source: the author.

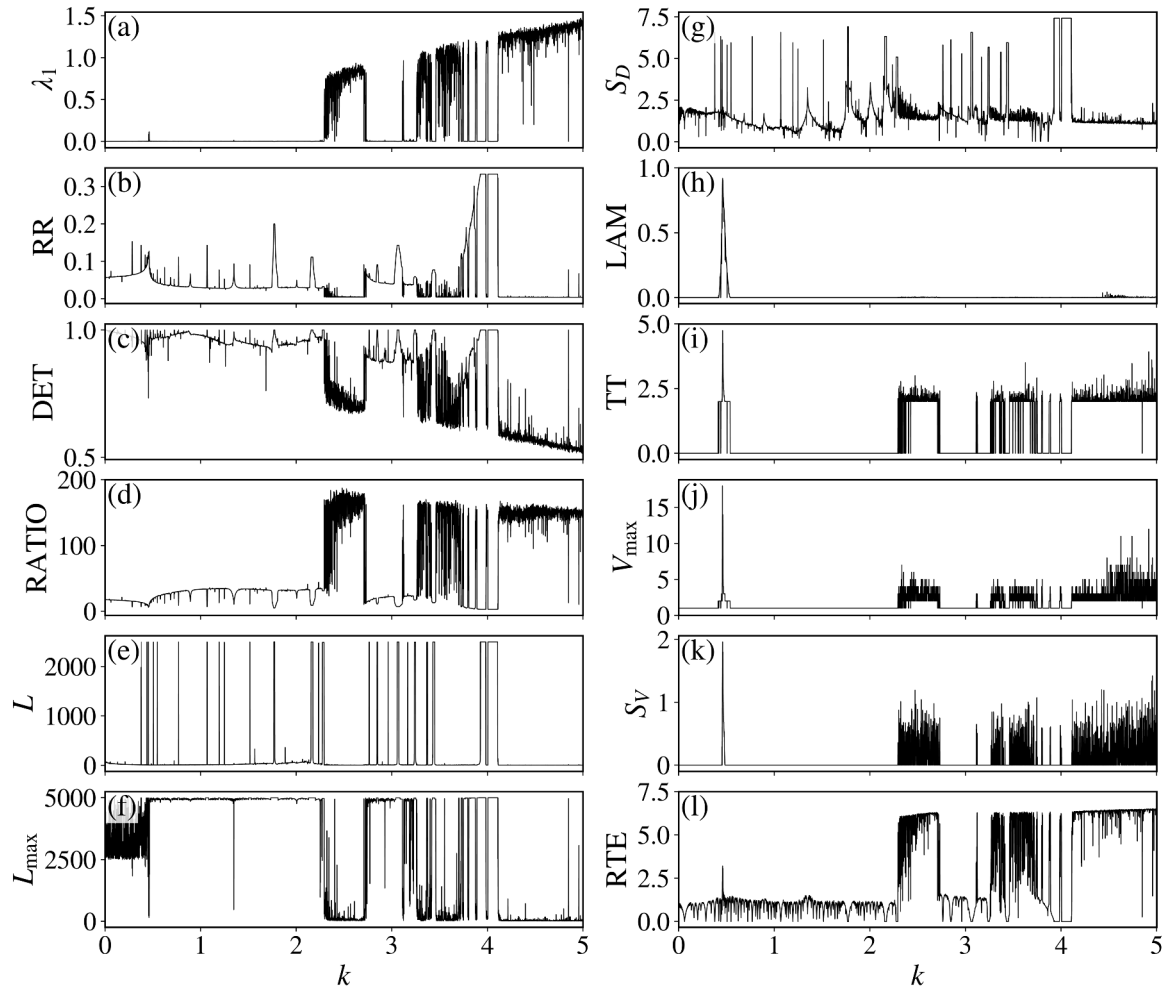
5.1.4 RQA Measures for the Standard Map

Next, we illustrate the application of the RQA for the standard map [Eq. (3.3)]. We choose a fixed initial condition, $(\theta_0, p_0) = (0.0, 1.3)$, and change the nonlinearity parameter in the interval $k \in [0, 5]$, with $\Delta k = 0.001$. For each parameter value, we generate a time series of length $N = 5000$ and compute the recurrence rate [Eq. (5.10), and Figure 5.3(b)], the RQA measures for the diagonal lines [Eqs. (5.12)-(5.16), and Figures 5.3(c)-(g)], for the vertical lines [Eqs. (5.18)-(5.21), and Figure 5.3(h)-(k)], and the recurrence time entropy [Eq. (5.23), and Figure 5.3(l)]. We also calculate the largest Lyapunov exponent, λ_1 [Figure 5.3(a)].

The measures based on the diagonal lines DET, RATIO, and L_{\max} capture quite well the regular/chaotic transitions, but the mean diagonal line length, L , and the entropy of diagonal lines, S_D , do not detect all of them. There is a clear anti-correlation between DET and L_{\max} and λ_1 . Whenever $\lambda_1 > 0$, DET and L_{\max} decrease, and in the regular windows, they exhibit a large value. However, during the regular windows ($\lambda_1 \approx 0$), DET and L_{\max} have a few isolated peaks and falls even though we do not observe such behavior in λ_1 [Figure 5.3(a)]. These might be fixed considering a longer time series. RATIO, on the other hand, exhibits a positive correlation with λ_1 , increasing its value for chaotic regions and keeping a small value when $\lambda_1 \approx 0$. It does not detect, however, the small chaotic region for $k \approx 0.5$.

Some of the measures based on vertical lines also capture the transition from regular to

Figure 5.3: (a) The largest Lyapunov exponent, (b) the recurrence rate, the RQA measures (c)-(g) based on diagonal lines, given by Eqs. (5.12)-(5.16), respectively, and (h)-(k) based on vertical lines, given by Eqs. (5.18)-(5.21), respectively, and (l) the recurrence time entropy [Eq. (5.23)] as a function of the nonlinearity parameter k , with a step of $\Delta k = 0.001$. The length of the time series is $N = 5000$, and for each parameter value, we choose a fixed initial condition of $(\theta_0, p_0) = (0.0, 1.3)$.



Source: the author.

chaotic dynamics. The mean trapping time, TT, and the longest vertical line, V_{\max} show clear maxima at the regions where $\lambda_1 > 0$, and zero values when $\lambda_1 \approx 0$ [Figures 5.3(i) and 5.3(j)], indicating that no vertical lines are detected in the last case. The entropy of vertical lines, S_V , exhibits high values in the chaotic windows, however, it falls to zero for some parameter values in these regions [Figure 5.3(k)], and the laminarity, LAM, does not give us any information for large values of k [Figure 5.3(h)]. The recurrence rate [Figure 5.3(b)] also does not capture the dynamical transitions. However, recently Palmero *et al.* demonstrated that by considering an ensemble of initial conditions and calculating RR for all of them, it is possible to find orbits that differ from the average behavior, and these orbits are the ones that experience stickiness (132).

The measure based on the recurrence times (white vertical lines) also exhibits a positive

Table 5.1: The correlation coefficient, ρ [Eq. (5.24)], between λ_1 and each one of the corresponding RQA measures for the standard map (3.3) in the interval $k \in [0, 5]$ (Figure 5.3) with a time series of length $N = 5000$ and initial condition $(\theta_0, p_0) = (0.0, 1.3)$ for each parameter value.

RR	DET	RATIO	L	L_{\max}	S_D	LAM	TT	V_{\max}	S_V	RTE
-0.42	-0.96	0.92	-0.19	-0.91	-0.21	-0.07	0.89	0.70	0.48	0.95

Source: the author.

correlation to λ_1 . Whenever $\lambda_1 > 0$, the RTE is large. Also, when $\lambda_1 \approx 0$, the RTE assumes low values. Furthermore, there are several values of k for which $\text{RTE} \rightarrow 0$, indicating that at these points, the initial condition $(\theta_0, p_0) = (0.0, 1.3)$ is very close to a periodic orbit. The oscillations in the regular windows are expected to diminish as we increase the length of the time series.

Therefore, at least qualitatively, we can see that some of the aforementioned measures are either positively or negatively correlated to λ_1 . In order to quantify this correlation, we use the Pearson correlation coefficient, defined by

$$\rho_{xy} = \frac{\text{cov}(x, y)}{\sigma_x \sigma_y}, \quad (5.24)$$

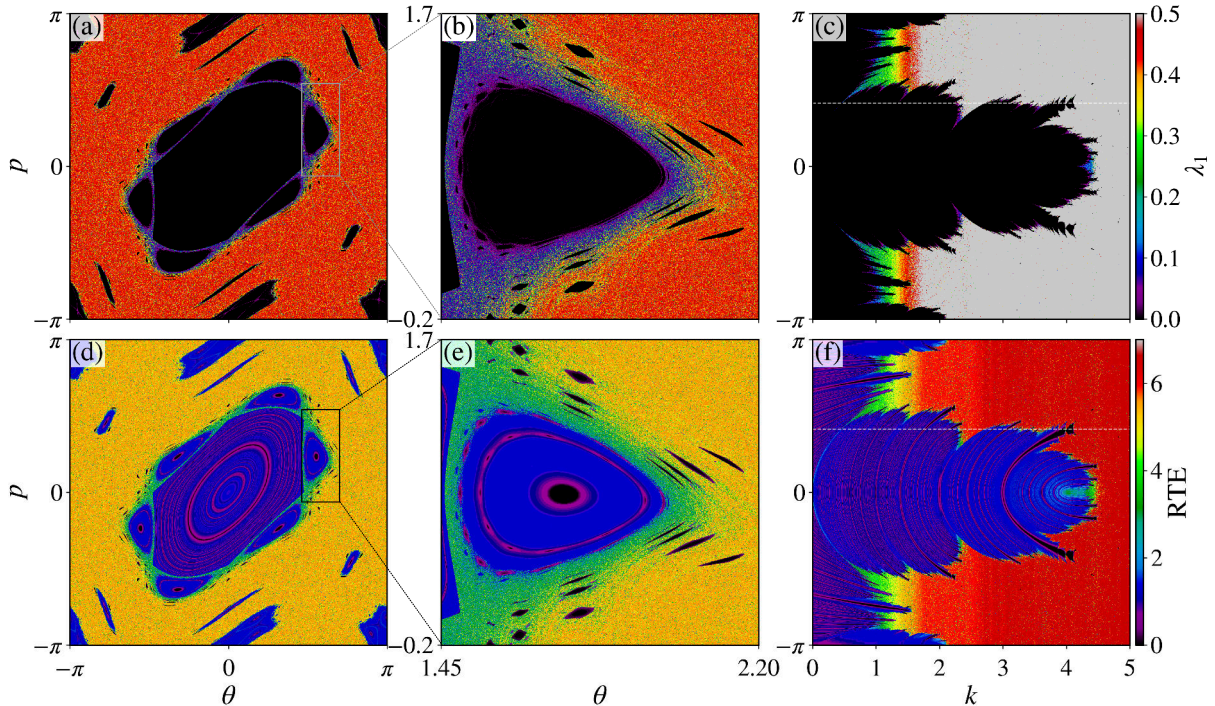
where $\text{cov}(x, y)$ is the covariance of the two time series, x and y , and σ_x and σ_y are their respective standard deviation. By calculating the correlation coefficient between λ_1 [Figure 5.3(a)] and all the RQA measures presented in Figures 5.3(b)-(l), we find that DET and L_{\max} are negatively correlated to λ_1 , while RATIO, TT, V_{\max} , and RTE are positively correlated to λ_1 . In both cases, the absolute value of the correlation coefficient is high. The remaining measures exhibit a small correlation coefficient (Table 5.1).

The RQA measures which generate the largest correlation coefficients are DET (-0.96) and RTE (0.95). However, Zou *et al.* demonstrated that by calculating RR in windows during the time evolution of the orbit (*cf.* Section 3.2), it is possible to detect transitions along the orbit evolution (*e.g.* trappings) (127). They also showed that DET detects such transitions, but not as efficiently as RR. Here, we seek a measure based on the intrinsic property of dynamical systems that quasiperiodic orbits can have at most three different return times to a previous point on the orbit. Therefore, we use the RTE as our mathematical tool to characterize chaotic dynamics.

5.2 RECURRENCE TIME ENTROPY

We have seen that the RTE captures the regular/chaotic transitions as we change the nonlinearity parameter k (Figure 5.3). To have a better visualization of the correspondence between λ_1 and the RTE, we plot in Figure 5.4 the values of λ_1 and RTE for 1000×1000 initial conditions uniformly distributed in a grid in phase space (θ, p) with $k = 1.5$, and in the parameter space

Figure 5.4: (a)-(c) The largest Lyapunov exponent, λ_1 , and (d)-(f) the recurrence time entropy, RTE, for a 1000×1000 uniformly distributed initial conditions in a grid in phase space with $k = 1.5$, for (a), (b), (d), and (e) and in parameter space (k, p) , with $\theta_0 = 0.0$ for (c) and (f). Panels (b) and (e) are magnifications of the white boxes in (a) and (d), respectively, and the dotted white line in (c) and (f) represents the initial condition used in Figure 5.3.

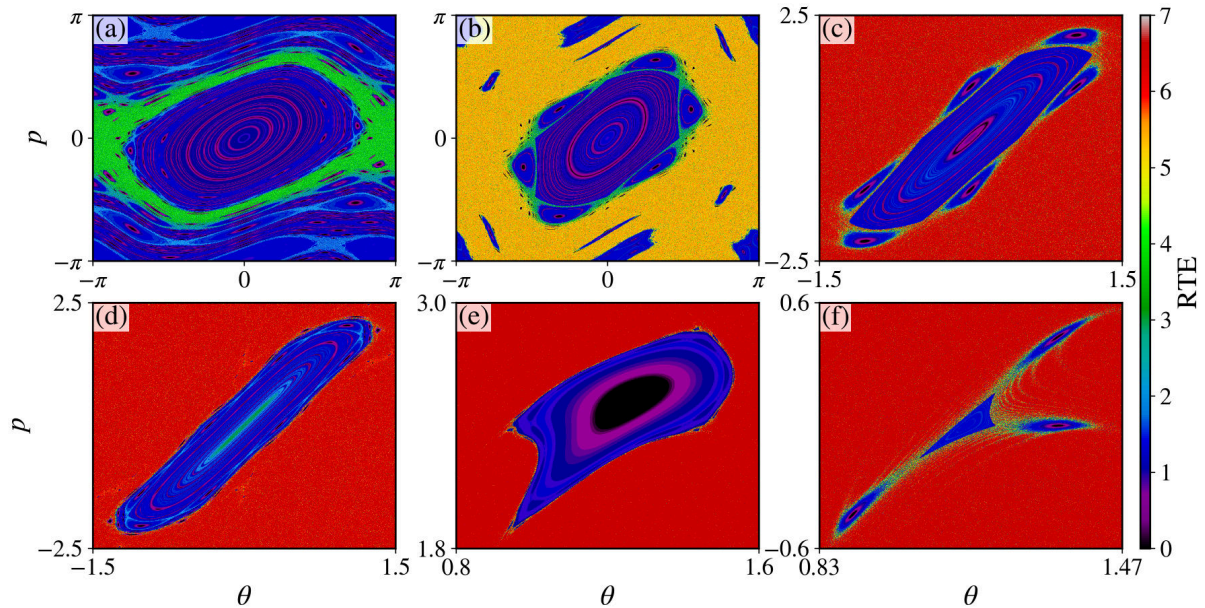


Source: the author.

(k, p) with $\theta_0 = 0.0$. Figures 5.4(b) and 5.4(e) are magnifications of the white boxes in Figures 5.4(a) and 5.4(d), respectively. The RTE encompasses all the characteristics of the Lyapunov exponent and more. In the chaotic sea, where the value of λ_1 is positive, the RTE is high, while within the islands where λ_1 approaches zero, the RTE is low. Additionally, in regions where the rotation number of the orbit approximates a rational number, the RTE is even lower (62, 64) [indicated by the transition from blue to purple in Figure 5.4(d)]. As we approach the elliptic points, the RTE gradually decreases, and Figure 5.4(f) demonstrates the occurrence of bifurcations and the transition from regular to chaotic behavior as k changes.

For the chosen parameter value of the standard map, namely $k = 1.5$, the system exhibits several sticky regions, resulting in a bimodal distribution of the FTLE (54) [Figure 3.5(b)]. The region between the main island and the period-6 satellite islands is particularly notable for exhibiting stickiness. In this region, both the value of λ_1 and the RTE decrease compared to the rest of the chaotic sea, demonstrating similar behavior. We also quantify the correlation between λ_1 and RTE for the data presented in Figure 5.4 using Eq. (5.24). For Figures 5.4(a) and 5.4(d), we obtain $\rho_{\lambda_1, \text{RTE}} = 0.93$, for Figures 5.4(b) and 5.4(e), we obtain $\rho_{\lambda_1, \text{RTE}} = 0.89$, and for Figures 5.4(c) and 5.4(f), we obtain $\rho_{\lambda_1, \text{RTE}} = 0.94$. Figure 5.5 shows the RTE for a grid of 1000×1000 initial conditions uniformly distributed in the depicted phase space regions for six distinct values

Figure 5.5: The RTE for a grid of 1000×1000 uniformly distributed initial conditions in the depicted phase space regions of the standard map (3.3), with (a) $k = 0.9$, (b) $k = 1.5$, (c) $k = 3.93$, (d) $k = 4.0$, (e) $k = 5.3$, and $k = 6.908745$. For each initial condition, we use a time series of length $N = 5000$. The regular orbits are characterized by small values of RTE (black to blue) while the chaotic orbits by a large value of RTE (green to red). The black points correspond to orbits for which none, or only one return time has been found. Increasing the length of the time series should decrease the size of the black regions. These regions also indicate the position of the elliptic points.



Source: the author.

of k [cf. Figure 4.1] where for each orbit we generate a time series of length $N = 5000$. There is a clear distinction from regular to chaotic dynamics for all values of k . The black to blue points (low values of RTE) correspond to the regular orbits, while the green to red points (large values of RTE) correspond to chaotic ones. We expect that by increasing the length of the time series, the size of the black regions should decrease. These regions appear for orbits which exhibit only one return time. This should occur only for periodic orbits, however, due to shortness of the time series, quasiperiodic orbits may exhibit only one return time, especially when close to the elliptic point.

Therefore, the RTE is an excellent measure to discern periodicity, weak chaos, and strong chaos. Also, we obtain remarkably good results with the RTE considering only a short time series (5000 data points). Next, we follow the evolution of a single chaotic orbit of the standard map over a long iteration time N . As time progresses, the orbit gradually fills the entire chaotic component of the phase space. Typically, the stickiness phenomenon persists for considerably long yet finite periods before the orbit escapes to the chaotic region. Consequently, to gain a deeper understanding of the transitions occurring within the orbit's dynamics, it is advantageous to consider a "finite-time" (cf. Section 3.2), denoted as $n \ll N$. Thus, we calculate the RTE throughout the evolution of a single chaotic orbit, dividing it into windows of size n

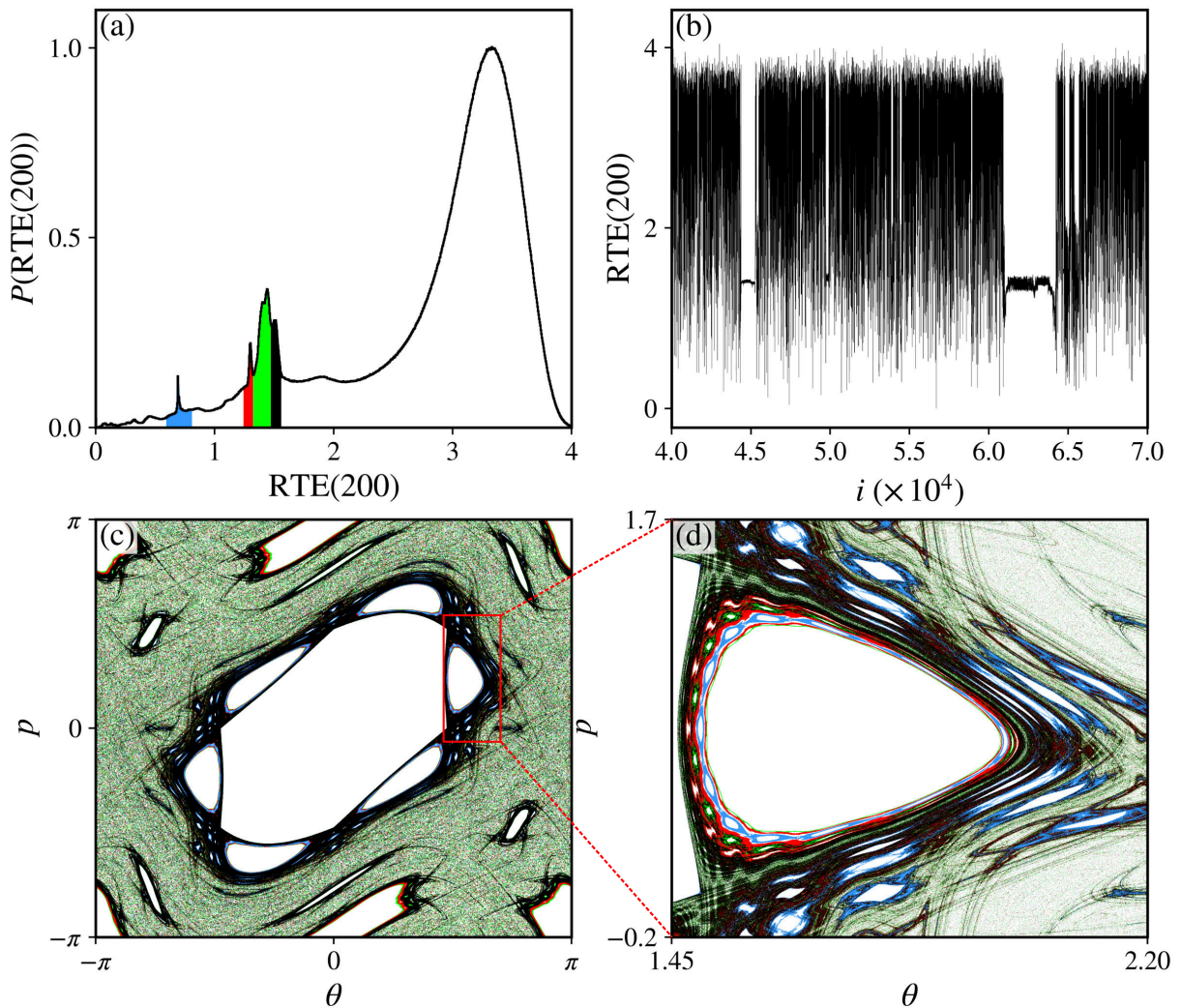
denoted as $\{\text{RTE}^{(i)}(n)\}_{i=1,2,\dots,M}$, where $M = N/n$. Furthermore, we define the probability distribution of the RTE over finite-time intervals, $P(\text{RTE}(n))$, by generating a frequency histogram of $\text{RTE}^{(i)}(n)$. An example of such a histogram is depicted in Figure 5.6(a) [cf. Figure 3.5(b)] for $N = 10^{10}$ and $n = 200$. Figure 5.6(b) exhibits the “time series” of the finite-time RTE, focusing on the interval ranging from $i = 4 \times 10^4$ to $i = 7 \times 10^4$. Notably, abrupt changes in the value of $\text{RTE}(200)$ are observed, indicating transitions between different regimes within the orbit’s dynamics. These fluctuations in the RTE value contribute to the emergence of multiple modes within its probability distribution. As we have previously mentioned, Szezech *et al.* (54) reported that for the specific value of k , the distribution of the finite-time Lyapunov exponent displayed a bimodal pattern [Figure 3.5(b)]. Our findings reveal that the minor peak observed in Figure 3.5(b) is, in fact, composed of multiple peaks, as suggested by Harle and Feudel (133).

The presence of multiple modes in the distribution is a consequence of the hierarchical islands-around-islands structure embedded in the phase space. When the orbit lies within the chaotic sea, the time- n RTE is high, corresponding to the largest peak in the distribution. Conversely, when the orbit becomes trapped near an island, the RTE decreases, leading to smaller peaks in the distribution for lower values of $\text{RTE}(200)$. As the orbit gets trapped in the vicinity of an island, it may cross to a deeper level within the hierarchical structure, and these transitions between different levels give rise to the multi-modal distribution (133). Furthermore, the closer to zero is λ_1 , the higher the hierarchical level of the island on which neighborhood the orbit is trapped (46). Hence, multiple peaks are formed for small values of RTE.

To identify the specific areas in phase space that correspond to the peaks in the distribution, we monitor the time series of $\text{RTE}(200)$ and plot the 200 phase space positions (θ, p) using different colors based on the ranges of $\text{RTE}(200)$. The colored points, including blue, red, green, and black, represent phase space positions associated with $\text{RTE}(200)$ values within the intervals $[0.6, 0.8]$, $[1.25, 1.33]$, $(1.33, 1.48]$, and $(1.48, 1.55]$, respectively [Figures 5.6(c) and 5.6(d)]. Each peak corresponds to a distinct hierarchical level of the structure, and the RTE allows an effective differentiation between them. Furthermore, the black and green points shadow the manifolds along which the non-trapped orbits exit the sticky region (134). Although only the hierarchical levels surrounding the period-6 islands are displayed in Figure 5.6(d), the RTE distribution encompasses contributions from all island chains. For a comprehensive analysis, we also examine the phase space points responsible for generating the peak for high RTE values. Whenever $\text{RTE}(200)$ falls within the range of $[2.5, 4.0]$, we plot the corresponding 200 phase space points (θ, p) [Figure 5.7(a)]. The information conveyed by the phase space components in Figures 5.6(c) and 5.7(a) complement each other: Figure 5.7(a) depicts the chaotic sea, representing the hyperbolic component of phase space, while Figure 5.6(c) displays the nonhyperbolic one. Nonhyperbolicity can inhibit chaotic orbits from visiting some regions due to tangencies between stable and unstable manifolds (50, 135, 136).

We can also quantify the duration of each stickiness regime, referred to as the “trapping time” t , which represents the time interval between consecutive abrupt changes in the RTE. In

Figure 5.6: (a) The finite-time RTE probability distribution for a single chaotic orbit with $n = 200$, $N = 1.0 \times 10^{10}$, $k = 1.5$, and $(\theta_0, p_0) = (-3.0, 0.0)$. (b) The finite-time RTE “time series” for the interval $[40000, 70000]$. The transitions between different regimes within the orbit’s dynamics are clear. Panel (c) is the phase space points that generate the minor maxima in (a) and (d) is a magnification of one of the period-6 satellite islands of (b) indicated by the red box.



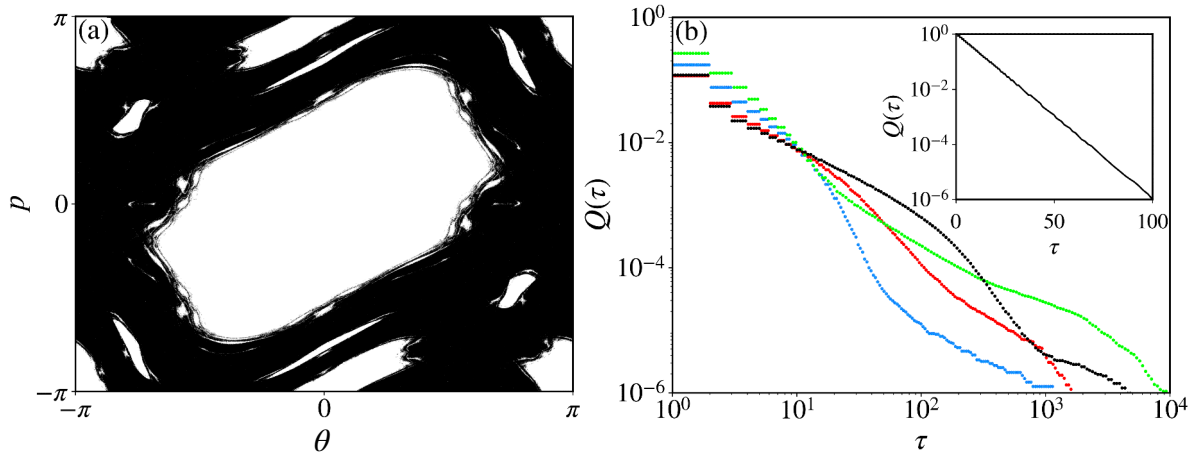
Source: the author.

Figure 5.6(b), these trapping periods are clearly visible, and we define the boundaries of each peak, indicated by the filled colors, as the limits of the stickiness regimes. By analyzing the RTE(200) time series, we obtain a collection of trapping times $\{t_j\}_{j=1,2,\dots,N_t}$ and define the probability distribution of trapping times as $P(t)$. Alternatively, we define the cumulative distribution of trapping times, denoted as $Q(\tau)$, as follows:

$$Q(\tau) = \sum_{t > \tau} P(t) = \frac{N_\tau}{N_t}, \quad (5.25)$$

where N_τ represents the number of trapping times $t > \tau$, and N_t is the total count of trapping times. Extensive research has established that fully chaotic systems exhibit an exponential decay

Figure 5.7: (a) The phase space points that generate the larger peak for high values of RTE in Figure 5.6(a) and (b) the log-log plot of the cumulative distribution of trapping times, $Q(\tau)$, for each sticky region identified in Figure 5.6(a) with $N = 10^{11}$ and $n = 200$ (colored dots). The inset is the log-lin plot of $Q(\tau)$ of the phase space points shown in (a). The colors of the dots in (b) match the colors of Figure 5.6(a).



Source: the author.

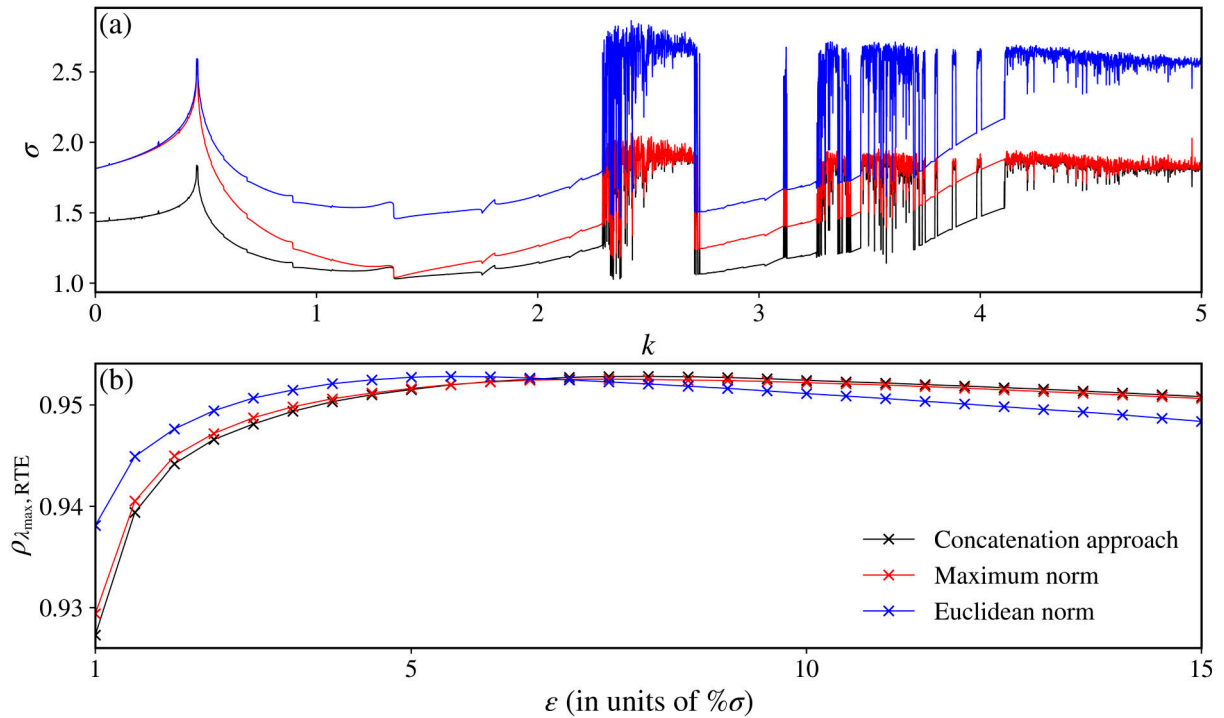
in the distribution of trapping times (including its cumulative distribution). In contrast, quasi-integrable Hamiltonian systems, which demonstrate the stickiness effect, display a power-law decay (27, 28, 39–45). By utilizing the finite-time RTE, we are able to distinguish between these two distinct behaviors present in the dynamics, specifically the hyperbolic and nonhyperbolic components. The cumulative distribution of trapping times in the hyperbolic region follows an exponential pattern [as shown in the inset of Figure 5.7(b)], whereas $Q(\tau)$ for the nonhyperbolic regions exhibits a power-law tail for large times [indicated by colored dots in Fig. 5.7(b)].

Overall, our findings indicate that the RTE is a robust and informative measure for characterizing dynamical systems, especially for distinguishing different types of chaotic behavior and identifying transitions in an orbit's evolution. The multi-modal distribution of finite-time RTE provides valuable insights into the system's complex behavior, allowing us to identify specific regions of interest and study trapping phenomena.

5.3 THE EFFECT OF THE THRESHOLD ON THE RTE

In Section 5.1.1 we made some considerations regarding the choice of the threshold ε : we chose ε to be 10% of the time series standard deviation σ , which were calculated considering a standard deviation vector, $\boldsymbol{\sigma}$, and taking its maximum norm [Eq. (5.6)]. In order to analyze the effect of ε on the previously shown results, we calculate the standard deviation using the (black) concatenation approach mentioned in Section 5.1.1 and the norm approach, considering the maximum (red) and Euclidean (blue) norms, as a function k , with the same initial condition as in Figures 5.3 with a time series of length 5000 [Figure 5.8(a)]. The concatenation and maximum norm approach yield similar standard deviations, while the Euclidean norm yields a larger value

Figure 5.8: (a) The standard deviation, σ , as a function of k for the orbit with initial condition $(\theta_0, p_0) = (1.3, 0.0)$ iterated for 5000 times, using the (black) concatenation approach and the (red and blue) norm approach, considering the maximum and Euclidean norms, respectively, and (b) the correlation coefficient between λ_1 and RTE, both evaluated in the interval $k \in [0, 5]$, as a function of the threshold ε in units of the percentage of σ .



Source: the author.

of σ . However, all methods agree that chaotic orbits have a larger standard deviation, as expected.

To determine the optimal method for calculating σ and an appropriate value of ε , we compute the correlation coefficient [Eq. (5.24)] between λ_1 and RTE as a function of ε (in units of $\% \sigma$) using the concatenation and norm approaches to calculate σ for the same interval of k and parameters as in Figure 5.3 [Figure 5.8(b)]. The three approaches yield similar correlation coefficients. Even if we choose a very small ε (e.g. 1% of σ), we still obtain a high correlation coefficient (≈ 0.93). Also, increasing ε does not affect significantly the correlation coefficient, indicating that in our case, the choice of ε is not as sensible as it would be in other cases. In fact, there is a range of values for ε in which the results are good.

6 DYNAMICAL PROPERTIES OF A BILLIARD MODEL

In this chapter we introduce another class of Hamiltonian systems: the billiard system. We introduce the Birkhoff coordinates, which are the canonical conjugate variables for this kind of system and we consider a family of billiard systems whose shape depends upon some parameter values. We present the billiard mapping and an algorithm to find the successive collisions of a particle with the billiard boundary. Next, we show the phase and configuration spaces for several parameter values and we calculate the largest Lyapunov exponent as a function of the billiard shape. Finally, we also calculate the dynamical quantity introduced in Chapter 4, dig , and the recurrence time entropy, RTE, introduced in Chapter 5.

6.1 BILLIARD DEFINITION

A billiard problem, or simply billiard, is one of the simplest dynamical systems to exhibit chaotic motion. In its simplest two-dimensional formulation, one considers a point-like particle of mass μ , or an ensemble of particles, confined in a simply connected planar region Ω delimited by hard walls. A billiard is a Hamiltonian system with potential $V(\mathbf{q}) = 0$ within the boundary and infinity on the boundary $\partial\Omega$. The particles undergo elastic collisions with the boundary $\partial\Omega$ such that only the direction of the velocity is changed and the angle of incidence equals the angle of reflection (137). Due to the relative structural simplicity of billiards, the emergence or not of chaotic behavior is fully dictated by the geometrical features of $\partial\Omega$ (137), *i.e.*, the presence of dispersing or defocusing components in the boundary $\partial\Omega$ (138). Thus, different geometries generate different dynamical behaviors, namely, (i) fully regular (*e.g.* circular and rectangular billiards (137)), in which all orbits lie on periodic or quasi-periodic *tori*, (ii) fully chaotic (*e.g.* Sinai (139) and stadium (140) billiards), in which almost every orbit fills densely the entire phase space, and lastly, (iii) mixed dynamics (*e.g.* oval (141, 142) and mushroom billiards (31, 32, 143, 144)), in which the phase space is composed of both regular and chaotic domains.

Billiard systems have been studied in the context of both classical (31, 32, 43, 44, 137–145) and quantum mechanics (146–150). Quantically, one is interested in obtaining the eigenfunctions and eigenvalues of the Helmholtz equation $(\nabla^2 + k^2)\psi_k(\mathbf{q}) = 0$ in Ω , for $k^2 = 2\mu E/\hbar^2$ (E is the particle's energy), assuming Dirichlet boundary conditions, *i.e.*, $\psi_k(\mathbf{q} \in \partial\Omega) = 0$. In this context, the statistical features of the spectrum of eigenenergies $\{E_n\}$ and the morphological aspects of the eigenstates $\psi_k^{(n)}$ depend on whether the corresponding classical billiard is or is not chaotic (151). The name “quantum chaology” has been given to this field of study, although some authors rather use “quantum chaos” (95, 152). Berry (153) argues that the latter should not be used since the idea of exponential sensitivity to initial conditions makes no sense for quantum systems. Nonetheless, this is just a matter of terminology.

On the other end of the realm of mechanics, *i.e.*, classical mechanics, one is interested in obtaining the classical trajectories in phase space. A classical billiard is a time-continuous system, called a billiard flow. The whole classical dynamics of billiards can be divided into two processes: (i) uniform motion within the billiard region Ω , since the potential is zero in this region, and (ii) specular reflection with the boundary $\partial\Omega$. As we have seen in Chapter 2, it is possible to define an appropriate Poincaré section to visualize the trajectories of time-continuous system. Billiard systems have the advantage of having a natural Poincaré section, which is the boundary of the billiard. Let s be the coordinate at the boundary $\partial\Omega$ which is equal to the distance from some point of reference at the boundary to a point where the particle gets reflected. If it is possible to parametrize the boundary of the billiard by the polar angle θ , $R(\theta)$, a convenient choice for the point of reference is the one for which $\theta = 0$. In this case, the length s is defined as

$$s(\theta) = \int_0^\theta \sqrt{R^2(\theta') + \left[\frac{dR(\theta')}{d\theta'} \right]^2} d\theta'. \quad (6.1)$$

Note that s is a cyclic coordinate, $s \in [0, \mathcal{L})$, where \mathcal{L} corresponds to the length of the whole boundary $\partial\Omega$. Another natural coordinate is the angle of reflection, *i.e.*, the angle α formed by the particle's trajectory just after the collision and the tangent line to the collision point. It is easy to see that $\alpha \in [0, \pi]$. The pair of coordinates (s, p) , where $p = \cos \alpha$, are the canonical variables for the billiard map, often called Birkhoff coordinates (154). The variable p is the momentum in the tangential direction. Under these variables, the phase space volume is preserved on the course of the dynamics, and the phase space is a cylinder $[0, \mathcal{L}) \times [-1, 1]$.

6.2 MODEL AND MAPPING

The Hamiltonian of a billiard system is

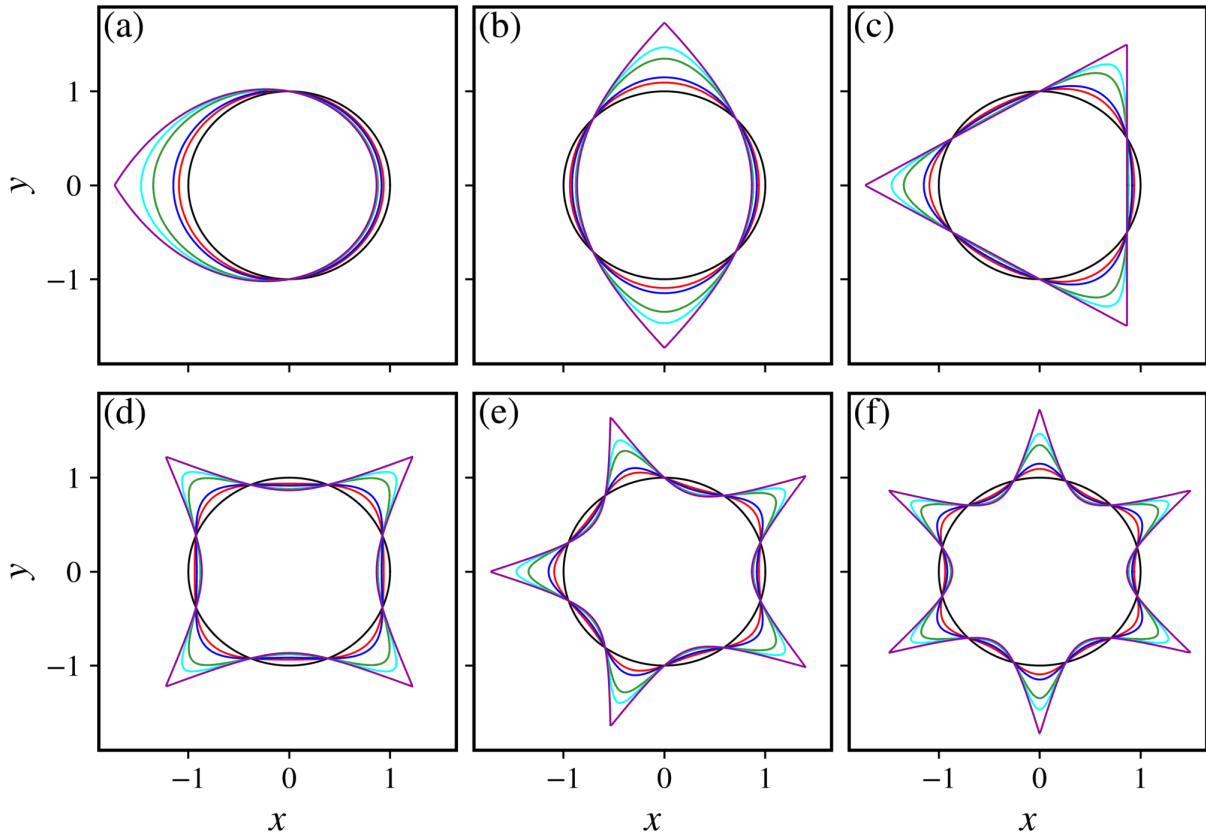
$$\mathcal{H}(\mathbf{p}, \mathbf{q}) = \frac{\mathbf{p}^2}{2\mu} + V(\mathbf{q}), \quad (6.2)$$

where \mathbf{p} is the momentum and \mathbf{q} the position. As we have previously stated, the potential energy is

$$V(\mathbf{q}) = \begin{cases} 0, & \text{for } \mathbf{q} \in \Omega, \\ \infty, & \text{otherwise.} \end{cases} \quad (6.3)$$

Because the collisions are elastic, the Hamiltonian is the total energy of the system and it is a constant of motion, $\mathcal{H} = E = \text{const}$. Let us now suppose that the potential energy also depends on some parameter $\xi \in \mathbb{R}$: $V(\mathbf{q}, \xi) = \xi W(\mathbf{q})$. This parameter may change the shape of the region Ω , for example, and we can obtain a family of billiards whose shape continuously changes as ξ changes. This problem is analogous to the problem of the robustness of integrability discussed in Section 2.3. The parameter ξ can be understood as a perturbation to the shape of a fully integrable billiard (*e.g.* circular billiard), leading to a quasi-integrable Hamiltonian system

Figure 6.1: The billiard boundary for (a) $\gamma = 1$, (b) $\gamma = 2$, (c) $\gamma = 3$, (d) $\gamma = 4$, (e) $\gamma = 5$, and (f) $\gamma = 6$ with different values of ξ , namely, (black) $\xi = 0.0$, (red) $\xi = 0.15$, (blue) $\xi = 0.30$, (green) $\xi = 0.75$, (cyan) $\xi = 0.90$, and (purple) $\xi = 0.99999$.



Source: the author.

which displays all the features discussed in Chapter 2 (mixed phase space, KAM *tori*, *cantori*, etc).

Here, we consider a family of billiards with the boundary shape, $R(\theta)$, implicitly parametrized by the equation (155)

$$R^2 + \frac{2\sqrt{3\xi}}{9} \frac{R^3}{R_0} \cos(\gamma\theta) = R_0^2, \quad (6.4)$$

where γ is an integer, $\xi \in [0, 1)$ controls the shape of the boundary, and $\xi = 0$ yields a circular shape. We consider $R_0 = 1$. Figure 6.1 displays different boundary shapes for different values of γ and ξ . For each γ we choose six values of ξ . For $\gamma = 3$ and $\gamma = 4$ we obtain an equilateral triangle and a square-like shape, respectively. We notice that the number of edges is related to γ . The case $\gamma = 3$ is particularly interesting because both $\xi = 0$ and $\xi \rightarrow 1$ yield fully integrable billiards.

The billiard map is a two-dimensional nonlinear mapping $\mathbb{M} : \mathbb{R}^2 \rightarrow \mathbb{R}^2$, such that

$$(s_{n+1}, p_{n+1}) = \mathbb{M}(s_n, p_n) = \mathbb{M}^n(s_0, p_0).$$

Considering a particle initially at s_0 , or equivalently, at θ_0 , with a initial tangential momentum p_0 , or initial angle α_0 , it starts its motion from the initial position (x_0, y_0) given by, in Cartesian coordinates,

$$\begin{aligned} x_0 &= x(\theta_0) = R(\theta_0) \cos \theta_0, \\ y_0 &= y(\theta_0) = R(\theta_0) \sin \theta_0. \end{aligned} \quad (6.5)$$

The angle the tangent line to the point (x_0, y_0) makes with the horizontal axis, measured counterclockwise, is

$$\phi_0 = \arctan \left[\frac{y'(\theta_0)}{x'(\theta_0)} \right] \mod 2\pi, \quad (6.6)$$

where the prime indicates the derivative with respect to θ . In this way, the direction of the particle's velocity, measured from the horizontal axis counterclockwise is

$$\mu_0 = \alpha_0 + \phi_0 \mod 2\pi. \quad (6.7)$$

Between two subsequent collisions, the particle executes a uniform motion described by the following equations:

$$\begin{aligned} x_1 &= x_0 + v_0 \cos(\mu_0) \Delta t, \\ y_1 &= y_0 + v_0 \sin(\mu_0) \Delta t, \end{aligned} \quad (6.8)$$

with $v_0 = 1$ and considering Δt to be the time interval between two collisions. Thus, the particle's trajectory is

$$y(\theta_1) - y(\theta_0) = \tan(\mu_0) [x(\theta_1) - x(\theta_0)]. \quad (6.9)$$

The slope of the particle's trajectory after the collision is given by

$$\alpha_1 = \phi_1 - \mu_0 \mod \pi. \quad (6.10)$$

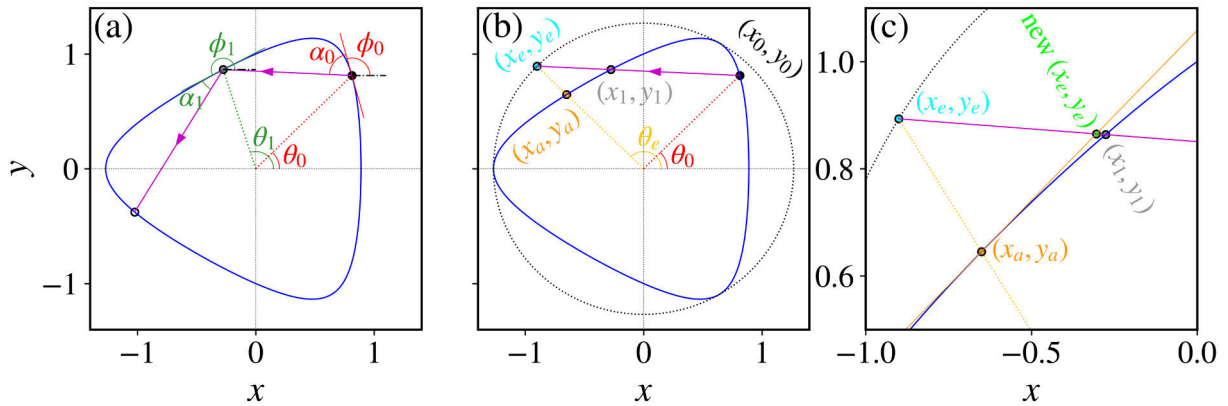
Therefore, the final form of the mapping is given by

$$\mathbb{M} : \begin{cases} F(\theta_{n+1}) &= y(\theta_{n+1}) - y(\theta_n) - \tan(\mu_n) [x(\theta_{n+1}) - x(\theta_n)], \\ \alpha_{n+1} &= \phi_{n+1} - \mu_n \mod \pi. \end{cases} \quad (6.11)$$

Figure 6.2(a) illustrates two successive collisions and the aforementioned angles. The next collision point, θ_{n+1} , is obtained numerically from $F(\theta_{n+1}) = 0$ using a bisection method, for example. However, in our case, there is a more efficient algorithm to calculate θ_{n+1} , which we will outline in the following. First, we consider a circle with radius $R_{\max} = R(\pi/\gamma)$, which is external to the billiard boundary [dotted black line in Figure 6.2(b) and 6.2(c)]. Next, we calculate the time it takes for the particle to reach the interception point between the particle's trajectory [Eq. (6.8)] and the outer circle as $x_p^2 + y_p^2 = R_{\max}^2$ [cyan dot in Figure 6.2(b)]. Thus, we obtain the quadratic equation

$$(\Delta t)^2 + 2[x_0 \cos \mu_0 + y_0 \sin \mu_0] \Delta t + x_0^2 + y_0^2 - R_{\max}^2 = 0,$$

Figure 6.2: (a) Illustration of two collisions on the billiard boundary and the angles used in the billiard map. Panels (b) and (c) illustrate the algorithm for finding the next collision point, discussed in the text.



Source: the author.

with solution

$$\Delta t_e = \frac{-b + \sqrt{b^2 - 4c}}{2}, \quad (6.12)$$

where

$$b = 2[x_0 \cos \mu_0 + y_0 \sin \mu_0],$$

$$c = x_0^2 + y_0^2 - R_{\max}^2.$$

Hence, the position of the interception point in Cartesian coordinates and its angular position are, respectively

$$x_e = x_0 + \cos(\mu_0) \Delta t_e,$$

$$y_e = y_0 + \sin(\mu_0) \Delta t_e, \quad (6.13)$$

$$\theta_e = \arctan\left(\frac{y_e}{x_e}\right) \bmod 2\pi.$$

After that, we find the position on the billiard boundary for the respective angle $\theta_e \equiv \theta_a$ as [orange dot in Figures 6.2(b) and 6.2(c)]

$$x_a = R(\theta_e) \cos \theta_e,$$

$$y_a = R(\theta_e) \sin \theta_e. \quad (6.14)$$

The tangent line that passes through (x_a, y_a) is given by [orange line in Figure 6.2(c)]

$$y_t(x) = y_a + \frac{y'(\theta_e)}{x'(\theta_e)}(x - x_a). \quad (6.15)$$

We now calculate the interception of this tangent line and the particle's trajectory [lime green

dot in Figure 6.2(c)] as $y_p = y_t(x_p)$:

$$y_0 + \sin(\mu_0)\Delta t_e^{\text{new}} = y_a + \frac{y'(\theta_e)}{x'(\theta_e)}[x_0 + \cos(\mu_0)\Delta t_e^{\text{new}} - x_a].$$

Isolating Δt_e^{new} , we obtain

$$\Delta t_e^{\text{new}} = \frac{y_a - y_0 + \frac{y'(\theta_e)}{x'(\theta_e)}(x_0 - x_a)}{\sin \mu_0 - \frac{y'(\theta_e)}{x'(\theta_e)} \cos \mu_0}, \quad (6.16)$$

and the new interception point $(x_e^{\text{new}}, y_e^{\text{new}})$ [lime green dot in Figure 6.2(c)] and its angular position are given by, respectively,

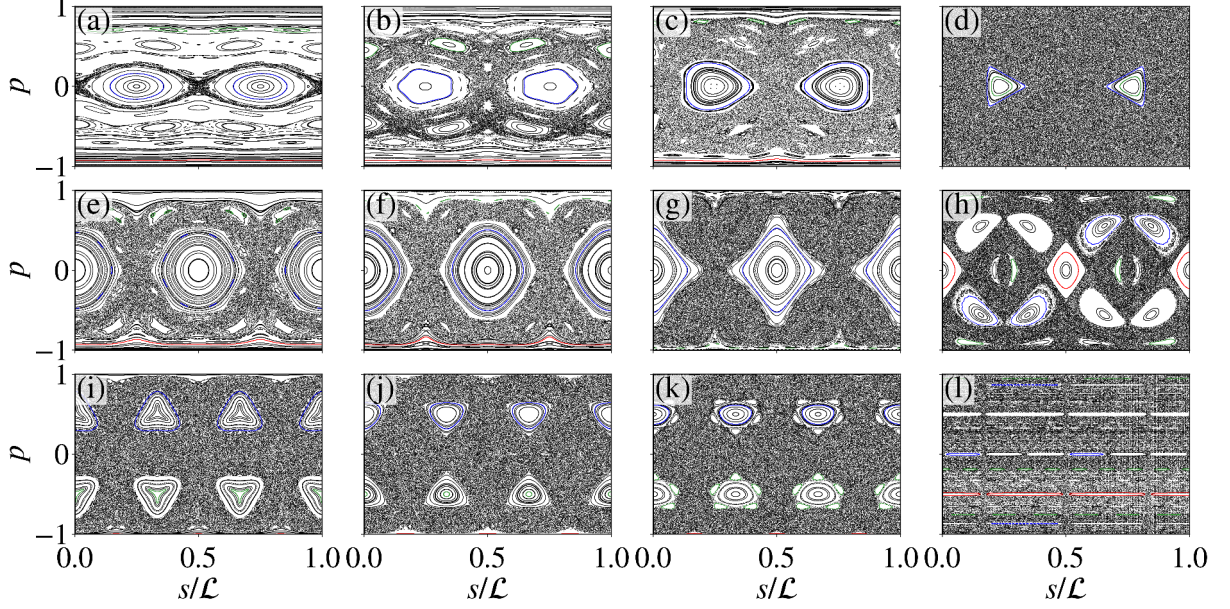
$$\begin{aligned} x_e^{\text{new}} &= x_0 + \cos(\mu_0)\Delta t_e, \\ y_e^{\text{new}} &= y_0 + \sin(\mu_0)\Delta t_e, \\ \theta_e^{\text{new}} &= \arctan\left(\frac{y_e}{x_e}\right). \end{aligned} \quad (6.17)$$

If $|\theta_e^{\text{new}} - \theta_a| < \text{TOL}$, $|x_e^{\text{new}} - x_a| < \text{TOL}$ and $|y_e^{\text{new}} - y_a| < \text{TOL}$, with $\text{TOL} = 10^{-11}$, we consider θ_e^{new} as the angular position of the particle's collision with the billiard boundary, *i.e.*, $\theta_1 = \theta_e^{\text{new}}$. If not, we repeat this procedure until the tolerance is satisfied. This is an efficient algorithm, however, it does not work when the boundary has convex components. Thus, we limit our analysis to $\gamma \leq 3$.

6.3 NUMERICAL RESULTS

Therefore, we use the mapping (6.11) and the just described algorithm to find the successive collisions with the boundary for $\gamma = 1, 2, 3$ with different values of ξ . Figure 6.3 shows the phase space for 75 randomly chosen initial conditions iterated for $N = 3.0 \times 10^3$ times for $\xi = 0.4, 0.6, 0.8, 0.99999$, where each line corresponds to a different value of γ . The colored curves (blue, red, and green) correspond to the regular orbits shown in Figure 6.4. The black orbit corresponds to a chaotic orbit. For $\gamma = 1$ and $\xi = 0.4$ [Figure 6.3(a)] we see a small chaotic region around $p = 0$ surrounding a period-2 island. The elliptical fixed points are located at $s/\mathcal{L} = 0.25, 0.75$, and $p = 0$. Since there are two elliptical points, there must exist two hyperbolic points (Poincaré-Birkhoff theorem). Indeed, they are located at $s/\mathcal{L} = 0.5, 1$ and $p = 0$. For higher (lower) values of p there exist other islands of stability which are surrounded by smaller chaotic regions. These chaotic components, however, are not connected to the chosen parameter values, similar to the phase space of the standard map [Eq. (3.3)] for $k < k_c$. Near the border of the phase space ($p \approx \pm 1$), some curves spread along the entire s -axis. These curves correspond to quasi-periodic orbits in which the perturbation slightly deforms their shape. They are called invariant spanning curves and these orbits are called whispering gallery orbits. As

Figure 6.3: The phase space of the billiard map (6.11) with the boundary implicitly defined by Eq. (6.4) for 75 randomly chosen initial conditions iterated for $N = 3.0 \times 10^3$ times with (a)-(d) $\gamma = 1$, (e)-(h) $\gamma = 2$, and (i)-(l) $\gamma = 3$. Each column corresponds to different values of ξ , namely, (a), (e), (i) $\xi = 0.4$, (b)(f)(j) $\xi = 0.6$, (c)(g)(k) $\xi = 0.8$, and (d)(h)(l) $\xi = 0.99999$.



Source: the author.

ξ increases, the chaotic domain spreads along the p -axis due to the destruction of the invariant quasi-periodic *tori*, and the connection of distinct chaotic domains. In the limiting case $\xi \rightarrow 1$ [Figure 6.3(d)], there are no spanning curves and almost all islands have been destroyed, except for the period-2 island around $p = 0$.

For $\gamma = 2, 3$, the corresponding chaotic component in phase space is larger than when $\gamma = 1$ for the same value of ξ . Also, as ξ approaches 1, several islands of stability reappear in the chaotic sea, and for $\gamma = 3$ the billiard boundary assumes the shape of an equilateral triangle, in which all orbits are regular. However, several chaotic regions are still present in the phase space even for $\xi = 0.99999$.

To quantify the dynamical behavior of the billiard model for different parameter values, we calculate the largest Lyapunov exponent, λ_1 . In order to do so, we need the Jacobian matrix [Eq. (3.4)] of the mapping:

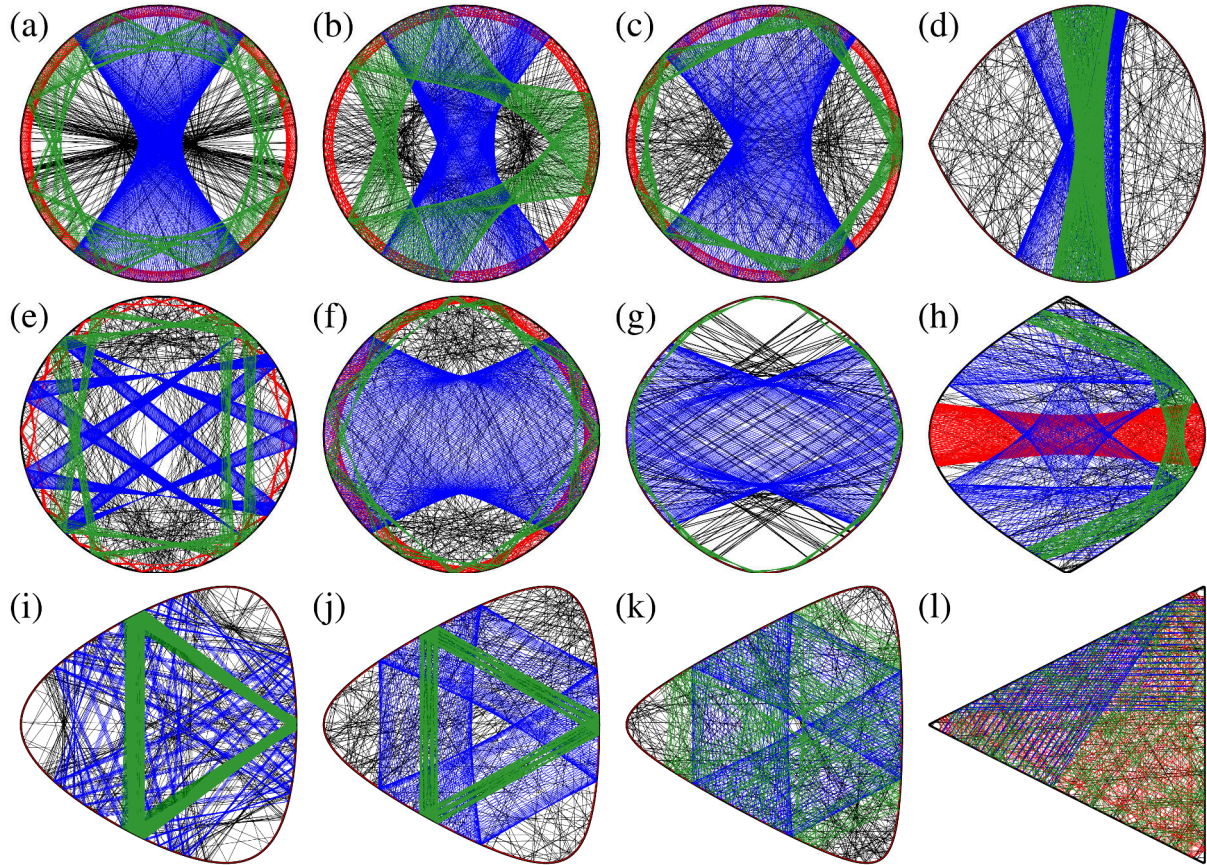
$$J = \begin{pmatrix} \frac{\partial \theta_{n+1}}{\partial \theta_n} & \frac{\partial \theta_{n+1}}{\partial \alpha_n} \\ \frac{\partial \alpha_{n+1}}{\partial \theta_n} & \frac{\partial \alpha_{n+1}}{\partial \alpha_n} \end{pmatrix}. \quad (6.18)$$

Derivating (6.9) with respect to θ_n and α_n ($\theta_0 = \theta_n$ and $\theta_1 = \theta_{n+1}$), we obtain, respectively

$$\frac{\partial \theta_{n+1}}{\partial \theta_n} = \frac{(1 + \tan^2 \mu_n) \frac{\partial \phi_n}{\partial \theta_n} \Delta x + y'(\theta_n) - x'(\theta_n) \tan \mu_n}{y'(\theta_{n+1}) - x'(\theta_{n+1}) \tan \mu_n}, \quad (6.19)$$

$$\frac{\partial \theta_{n+1}}{\partial \alpha_n} = \frac{(1 + \tan^2 \mu_n) \Delta x}{y'(\theta_{n+1}) - x'(\theta_{n+1}) \tan \mu_n}, \quad (6.20)$$

Figure 6.4: The configuration space of the billiard map for four different initial conditions with (a)-(d) $\gamma = 1$, (e)-(h) $\gamma = 2$, and (i)-(l) $\gamma = 3$. Each column corresponds to different values of ξ , namely, (a), (e), (i) $\xi = 0.4$, (b)(f)(j) $\xi = 0.6$, (c)(g)(k) $\xi = 0.8$, and (d)(h)(l) $\xi = 0.99999$. The respective orbit in phase space is shown as colored lines in Figure 6.3.



Source: the author.

where

$$\begin{aligned} \Delta x &= x(\theta_{n+1}) - x(\theta_n), \\ \frac{\partial \phi_n}{\partial \theta_n} &= \frac{x'(\theta_n)y''(\theta_n) - x''(\theta_n)y'(\theta_n)}{x'^2(\theta_n) + y'^2(\theta_n)}, \\ x'(\theta) &= \frac{dx}{d\theta} = \frac{dR(\theta)}{d\theta} \cos \theta - R(\theta) \sin \theta, \\ y'(\theta) &= \frac{dy}{d\theta} = \frac{dR(\theta)}{d\theta} \sin \theta + R(\theta) \cos \theta, \\ x''(\theta) &= \frac{d^2x}{d\theta^2} = \frac{d^2R(\theta)}{d\theta^2} \cos \theta - 2\frac{dR(\theta)}{d\theta} \sin \theta - R(\theta) \cos \theta, \\ y''(\theta) &= \frac{d^2y}{d\theta^2} = \frac{d^2R(\theta)}{d\theta^2} \sin \theta + 2\frac{dR(\theta)}{d\theta} \cos \theta - R(\theta) \sin \theta, \\ R'(\theta) &= \frac{dR(\theta)}{d\theta} = \frac{a\gamma R^2 \sin(\gamma\theta)}{2R_0 + 3aR \cos(\gamma\theta)}, \end{aligned}$$

$$R''(\theta) = \frac{d^2 R(\theta)}{d\theta^2} = a\gamma R \left\{ [2R' \sin(\gamma\theta) + \gamma R \cos(\gamma\theta)] [2R_0 + 3aR \cos(\gamma\theta)] - \frac{2R\sqrt{3\xi}}{3} \sin(\gamma\theta) [R' \cos(\gamma\theta) + \gamma R \sin(\gamma\theta)] \right\} \times [2R_0 + 3aR \cos(\gamma\theta)]^{-2}.$$

To obtain the remaining two elements of the Jacobian matrix, we calculate the derivative of (6.10) with respect to both θ_n and α_n . We get

$$\frac{\partial \alpha_{n+1}}{\partial \theta_n} = \frac{\partial \phi_{n+1}}{\partial \theta_{n+1}} \frac{\partial \theta_{n+1}}{\partial \theta_n} - \frac{\partial \phi_n}{\partial \theta_n}, \quad (6.21)$$

$$\frac{\partial \alpha_{n+1}}{\partial \alpha_n} = \frac{\partial \phi_{n+1}}{\partial \theta_{n+1}} \frac{\partial \theta_{n+1}}{\partial \alpha_n} - 1. \quad (6.22)$$

As we have seen in Chapter 3, for volume-preserving maps, the determinant of the Jacobian matrix, $|J|$, is equal to unity. However, by writing the Jacobian matrix in terms of the angles (θ, α) , this condition is not satisfied (black curve in Figure 6.5). Indeed,

$$\begin{aligned} |J| &= \frac{\partial \theta_{n+1}}{\partial \theta_n} \frac{\partial \alpha_{n+1}}{\partial \alpha_n} - \frac{\partial \theta_{n+1}}{\partial \alpha_n} \frac{\partial \alpha_{n+1}}{\partial \theta_n}, \\ &= \frac{\partial \theta_{n+1}}{\partial \theta_n} \left(\frac{\partial \phi_{n+1}}{\partial \theta_{n+1}} \frac{\partial \theta_{n+1}}{\partial \alpha_n} - 1 \right) - \frac{\partial \theta_{n+1}}{\partial \alpha_n} \left(\frac{\partial \phi_{n+1}}{\partial \theta_{n+1}} \frac{\partial \theta_{n+1}}{\partial \theta_n} - \frac{\partial \phi_n}{\partial \theta_n} \right), \\ &= -\frac{\partial \theta_{n+1}}{\partial \theta_n} + \frac{\partial \phi_n}{\partial \theta_n} \frac{\partial \theta_{n+1}}{\partial \alpha_n}, \\ &= -\frac{(1 + \tan^2 \mu_n) \frac{\partial \phi_n}{\partial \theta_n} \Delta x + y'(\theta_n) - x'(\theta_n) \tan \mu_n}{y'(\theta_{n+1}) - x'(\theta_{n+1}) \tan \mu_n} + \frac{\partial \phi_n}{\partial \theta_n} \frac{(1 + \tan^2 \mu_n) \Delta x}{y'(\theta_{n+1}) - x'(\theta_{n+1}) \tan \mu_n}, \\ &= -\frac{y'(\theta_n) - x'(\theta_n) \tan \mu_n}{y'(\theta_{n+1}) - x'(\theta_{n+1}) \tan \mu_n}. \end{aligned}$$

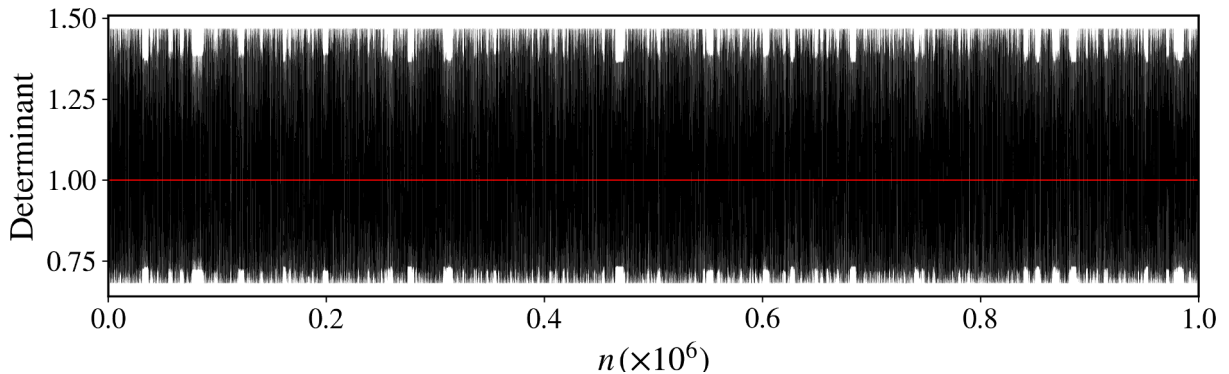
This outcome could be surprising, considering that billiard systems belong to the class of Hamiltonian systems and are expected to be area-preserving. However, this becomes clear when we recall that the variables (θ, α) are not the canonical conjugate variables of the problem (156). If we write the Jacobian matrix in terms of the Birkhoff coordinates (s, p) (154) as

$$\mathcal{J} = \begin{pmatrix} \frac{\partial s_{n+1}}{\partial s_n} & \frac{\partial s_{n+1}}{\partial p_n} \\ \frac{\partial p_{n+1}}{\partial s_n} & \frac{\partial p_{n+1}}{\partial p_n} \end{pmatrix} \quad (6.23)$$

with its elements given by

$$\begin{aligned} \frac{\partial s_{n+1}}{\partial s_n} &= \sqrt{\frac{R^2(\theta_{n+1}) + R'^2(\theta_{n+1})}{R^2(\theta_n) + R'^2(\theta_n)}} \frac{\partial \theta_{n+1}}{\partial \theta_n}, \\ \frac{\partial s_{n+1}}{\partial p_n} &= -\frac{\sqrt{R^2(\theta_{n+1}) + R'^2(\theta_{n+1})}}{\sin \alpha_n} \frac{\partial \theta_{n+1}}{\partial \alpha_n}, \end{aligned}$$

Figure 6.5: The determinant of the Jacobian matrix in terms of (black) (θ, α) and in terms of (red) the Birkhoff coordinates (s, p) for $\gamma = 1$ and $\xi = 0.6$ with $(\theta_0, \alpha_0) = (\pi, \pi/2)$.



Source: the author.

$$\frac{\partial p_{n+1}}{\partial s_n} = -\frac{\sin \alpha_{n+1}}{\sqrt{R^2(\theta_n) + R'^2(\theta_n)}} \frac{\partial \alpha_{n+1}}{\partial \theta_n},$$

$$\frac{\partial p_{n+1}}{\partial p_n} = \frac{\sin \alpha_{n+1}}{\sin \alpha_n} \frac{\partial \alpha_{n+1}}{\partial \alpha_n},$$

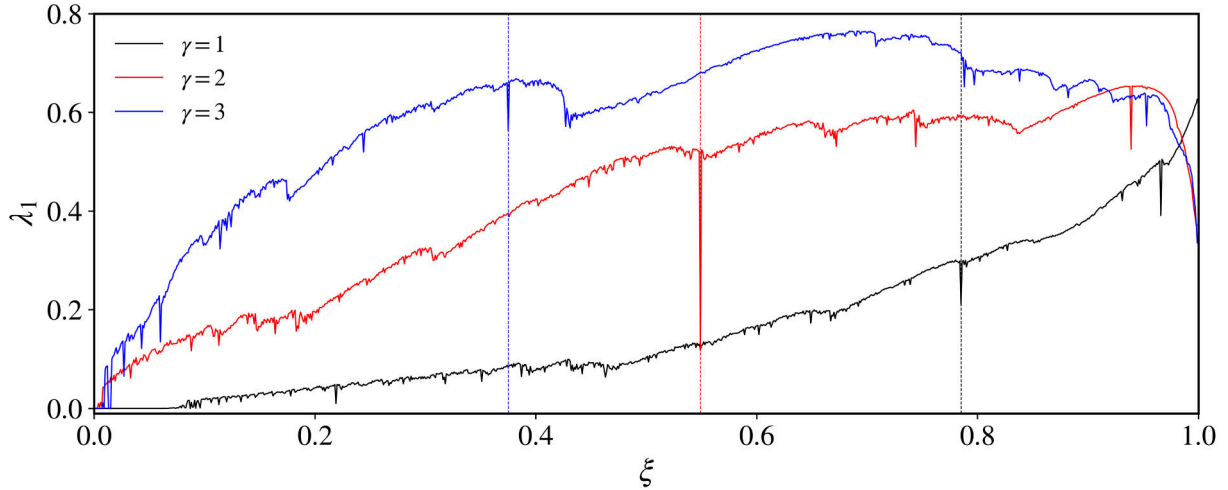
we obtain $|\mathcal{J}| = 1$ (red curve in Figure 6.5), as expected. It is important to mention that the results do not depend on which coordinates one uses. Both (θ, α) and (s, p) yield the same dynamical behavior and the same Lyapunov exponents. The only difference is that the phase space is slightly deformed when using (θ, α) (156).

Figure 6.6 presents the behavior of λ_1 as a function of $\xi \in [0, 1)$, with $\Delta\xi = 0.001$, for three different values of γ : 1, 2, and 3. For each value of ξ we consider $N = 10^8$ collisions. For the case of $\gamma = 1$ (black curve), we observe that as ξ increases, the average value of λ_1 also increases. This behavior aligns with our previous findings where we discussed the increase in the area of the chaotic component with ξ [Figures 6.3(a)-6.3(d)]. Similarly, for $\gamma = 2$ and $\gamma = 3$, we note a similar trend of increasing λ_1 with ξ , although there are a few exceptions where λ_1 decreases for specific values of ξ .

The most noticeable difference between $\gamma = 1$ and $\gamma = 2, 3$ emerges when $\xi \rightarrow 1$. In the case of $\gamma = 3$, the billiard takes the shape of an equilateral triangle, which exclusively exhibits periodic and quasi-periodic orbits, leading to $\lambda_1 \rightarrow 0$. On the other hand, for $\gamma = 2$, the phase space still exhibits both chaotic and regular regions. However, as $\xi \rightarrow 1$, the area of the chaotic component decreases [Figures 6.3(e)-6.3(h)], consequently resulting in a decrease in λ_1 .

Throughout all three cases, there are several values of ξ where λ_1 undergoes sharp falls. It is important to remember that the infinite-time Lyapunov exponent [Eq. (3.7)] is independent of the initial condition. However, for numerical computations, we evaluate the finite-time Lyapunov exponent, and as a result, the values of ξ corresponding to these sharp falls may vary with different initial conditions. These abrupt drops in λ_1 can be attributed to the stickiness effect: for specific parameter values and initial conditions, the chaotic orbits get trapped in the

Figure 6.6: The largest Lyapunov exponent as a function of the parameter ξ for $\Delta\xi = 0.001$ with (black) $\gamma = 1$ and $(\theta_0, \alpha_0) = (\pi, \pi/2)$, (red) $\gamma = 2$ and $(\theta_0, \alpha_0) = (\pi/2, \pi/2)$, and (blue) $\gamma = 3$ and $(\theta_0, \alpha_0) = (\pi, 1.08)$. For each value of ξ , we consider $N = 1.0 \times 10^8$ collisions. The vertical dashed lines indicates the values of ξ of Figure 6.7.



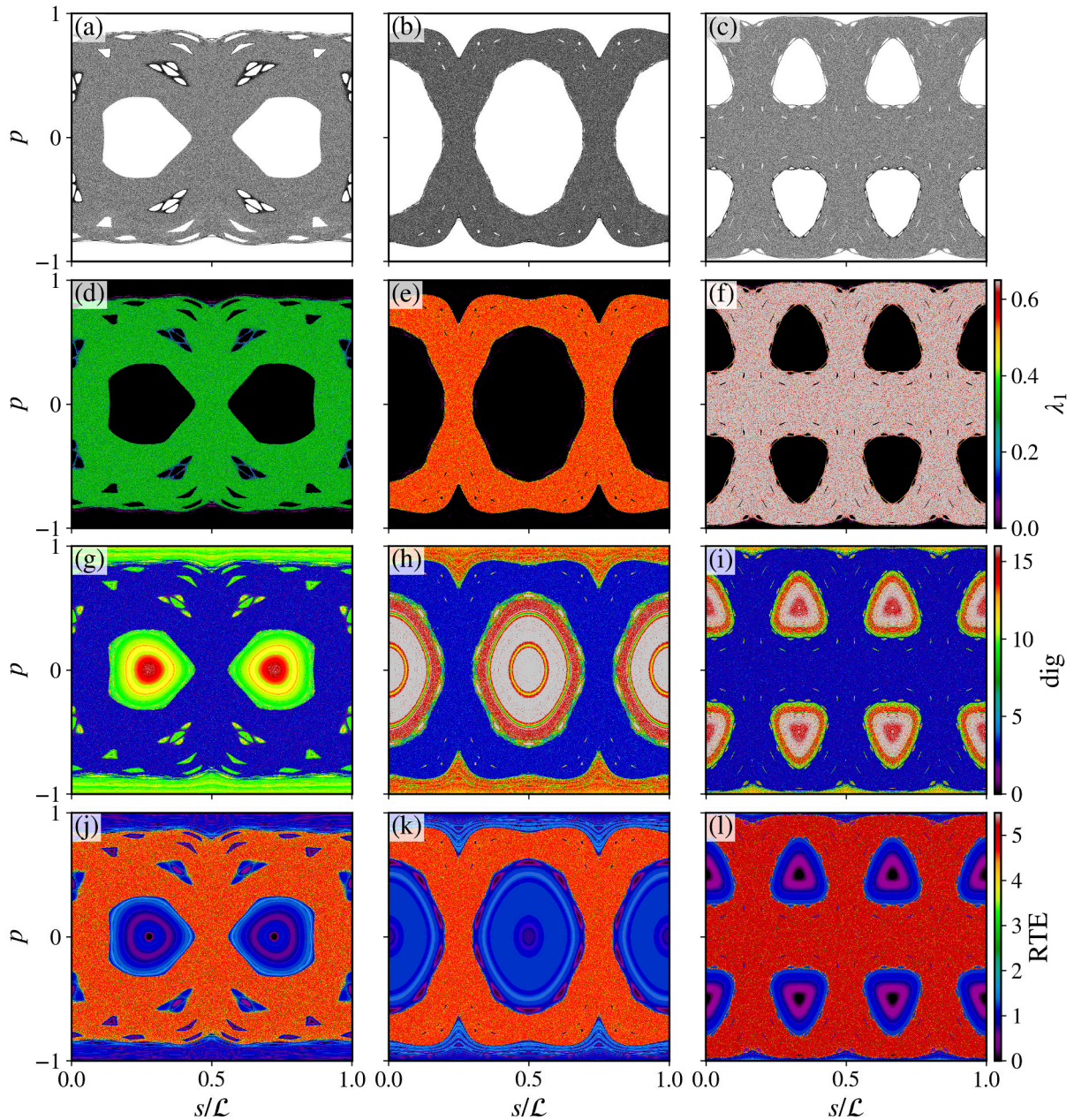
Source: the author.

vicinity of sticky regions [Figures 6.7(a)-6.7(c)], leading to smaller values of λ_1 . These trapping phenomena become more evident when examining Figures 6.7(a) and 6.7(c).

Therefore, λ_1 characterizes well the dynamical behavior of a single initial condition as ξ changes. It is also useful to consider a grid of initial conditions distributed in the entire phase space to analyze the effect of different initial conditions [Figures 6.7(d)-6.7(f)]. For $\gamma = 1$ and $\xi = 0.785$ [Figure 6.7(d)], a sticky region can clearly be seen around the chain of four periodic islands (green to blue). Also, in the border of the chaotic component, we observe that another small chaotic component arises with a very small area, and hence very small λ_1 . As ξ increases, this small chaotic domain will increase and merge with the large chaotic sea (green). For $\gamma = 2, 3$ [Figures 6.7(e) and 6.7(f)] there are no sticky regions as evident as in the previous case.

The dynamical quantity introduced in Chapter 4 as the number of zeros after the decimal point of the convergence of the weighted Birkhoff average, dig [Eq. (4.5)], can also be used to characterize the dynamics of billiard systems [Figures 6.7(g)-6.7(i)]. Analogously to what we have done in Chapter 4, we consider the function $h = \cos \theta$, as θ is also a cyclic coordinate with period 2π such as the coordinate variable in the standard map. For each initial condition, we consider a total number of collisions of $2N = 2 \times 10^4$. For $\gamma = 2, 3$, the islands exhibit a large value of dig , however, some of the orbits within the islands exhibit a small value of dig (green). These orbits correspond to the orbits whose rotation number approximates a rational number, thus breaking one of the assumptions (Diophantine condition) of Theorems 1.1 and 3.1 of Ref. (64) and decreasing the convergence of the weighted Birkhoff average. For $\gamma = 1$, the orbits around the elliptic point have a large value of dig , however, the farther from this point, the smaller the value of dig (red to green). Nevertheless, in all three cases, all chaotic orbits exhibit a small value of dig (blue) and even though the islands and the spanning invariant curves

Figure 6.7: (a)-(c) The phase space of a single chaotic orbit with initial conditions (a) $(\theta_0, \alpha_0) = (\pi, \pi/2)$, (b) $(\theta_0, \alpha_0) = (\pi/2, \pi/2)$, and (c) $(\theta_0, \alpha_0) = (\pi, 1.08)$ for $N = 2 \times 10^6$ collisions. (d)-(f) The largest Lyapunov exponent, λ_1 [Eq. (3.20)], (g)-(i) dig quantity [Eq. (4.5)], and (j)-(l) the recurrence time entropy, RTE [Eq. (5.23)], for 1000×1000 initial conditions uniformly distributed in a grid on the entire phase space. Each column corresponds to specific values of γ and ξ [dashed vertical lines in Figure 6.6]: (left column) $\gamma = 1$ and $\xi = 0.785$, (middle column) $\gamma = 2$ and $\xi = 0.549$, and (right column) $\gamma = 3$ and $\xi = 0.375$.



Source: the author.

show a relatively small value of dig (≈ 10), it is still possible to distinguish between regular and chaotic orbits using this measure. Also, it is worth mentioning that the length of the orbits used to generate Figures 6.7(g)-6.7(i) is considerably smaller than the length used for the standard map [Figure 4.1]. By increasing the length of the orbits, we expect a much better convergence rate for the weighted Birkhoff average, *i.e.*, a larger value of dig for the regular orbits.

Finally, the recurrence time entropy, RTE [Eq. (5.23)], can also be an alternative measure for distinguishing regular and chaotic behavior in billiard systems. Slater's theorem has been used to detect quasi-periodic orbits for billiard systems (157), and as a consequence of the validity of the theorem for billiard systems, the RTE yields similar results as it does for the standard map [Figures 6.7(j)-6.7(l)]. We consider $N = 5000$ collisions and we use the Birkhoff coordinates as our state variables to construct the recurrence matrix using the maximum norm. We consider the threshold to be 10% of the time series standard deviation, which is calculated using the maximum norm approach discussed in Chapter 5.

The orbits around the elliptic point yield zero RTE (black) as only one return time has been found for the given time series length and the chaotic sea exhibits a large value of RTE. For $\gamma = 1$ and $\xi = 0.725$ [Figure 6.7(j)], around the sticky region, observed in both Figures 6.7(a) and 6.7(d), there is a decrease in the RTE, indicating the trapped orbits. Lastly, the invariant spanning curves also yield a small value of RTE.

Therefore, all three dynamical quantities analyzed in this Chapter provide good results for the distinction of regular and chaotic behavior for billiard systems. The largest Lyapunov exponent and the recurrence time entropy can also be used to detect sticky orbits. The latter, together with the dig quantity, has the advantage of not needing the Jacobian matrix of the system. For systems where we know explicitly the equations of motion (or the equations of the mapping), the Jacobian matrix can be easily obtained. However, for systems where there are no such explicit equations, as in the case of billiard systems, obtaining the expressions for the matrix can be a difficult, and sometimes impossible, task.

7 FINAL REMARKS

In this thesis we have analyzed the dynamics of Hamiltonian systems by means of two relative new and non-standard dynamical quantities. The development of efficient and accurate mathematical tools to categorize orbits with respect to their dynamical behavior (chaotic or regular) is of major importance, specially when dealing with two-dimensional Hamiltonian systems, in which chaotic and regular regions are disconnected domains.

Initially, we made a brief survey on the features of the standard map, which is a paradigmatic model in the field of Hamiltonian chaos. We have shown (as several other authors have as well) that in spite its mathematical simplicity, this model encompasses all features of quasi-integrable Hamiltonian systems discussed in Chapter 2 such as mixed phase space and sticky regions due to *cantori*. We also introduced the Lyapunov exponents (LEs) which are the most widespread diagnostic for the detection of chaotic behavior and they hold in their definition the most important feature of chaotic motion: the sensitivity to the initial conditions, *i.e.*, they are a measure of the average exponential rate of divergence or convergence of nearby orbits in phase space. However, due to numerical limitations, it is impossible to reach the infinite-time definition of the LEs, and we have shown that the presence of sticky regions in phase space makes the LEs not the optimal choice to detect whether quasi-integrable Hamiltonian systems exhibit chaotic behavior or not.

We also reviewed Zaslavsky's derivation of the Fokker-Plank-Kolmogorov (FPK) equation (27, 47, 82, 86–88), which results in normal transport, and showed that for several values of the nonlinearity parameter, k , of the standard map, this theoretical prediction fails, and the system exhibits anomalous diffusion. Furthermore, we presented the generalization of the diffusion process and introduced the diffusion exponent, which characterizes the anomalous diffusion.

Anomalous diffusion is related to the existence of accelerator mode islands and a particular value of k , namely, $k = 6.908745$, yields an accelerator mode of period 1 with a self-similar hierarchical structure of islands-around-islands (88). We have analyzed the escape time and the island's boundary dimension for different levels in this self-similar structure. We used the uncertainty fraction method (101–103) to obtain the box-counting dimension of the boundary, and to define the final state of an orbit, *i.e.*, whether it is regular or chaotic, we considered a relative new dynamical quantity, *dig*, based on a weighted Birkhoff average. We considered this methodology given the aforementioned convergence issues of the LEs discussed in Chapter 3, and we have shown that using *dig*, we can accurately distinguish between regular and chaotic orbits. We have also shown that the smaller the scale, the longer it takes for the orbits to escape and the larger the dimension of boundary. Also, at different scales, the system exhibits different effective fractal dimension, which differs from the asymptotic value obtained when the scale goes to zero. Therefore, as we can relate the uncertainty in the initial conditions to the resolution of a measuring device, at realistic length scales, the uncertainty of the measurement is determined

by the effective fractal dimension, rather than by the fractal dimension's asymptotic value.

Next, we focused on exploring a powerful mathematical tool for characterizing dynamical systems: recurrence plots (RPs). We briefly reviewed some essential characteristics and features of RPs, demonstrating that the graphical representation of RPs for different dynamical processes is fundamentally distinct. We then defined the most commonly used measures based on the diagonal and vertical lines to quantify RPs, which is called recurrence quantification analysis (RQA). In addition to these measures, we introduced a less known but valuable measure based on the recurrences of an orbit, originally defined independently of RPs (68). The white vertical lines in an RP, *i.e.*, the vertical “gaps” between diagonal lines, provide an estimate of an orbit's return times. Measures based on the distribution of these return times, particularly the recurrence time entropy (RTE) (68, 70), are noteworthy due to Slater's theorem. According to this theorem, quasiperiodic orbits can have at most three return times, which makes the RTE a promising measure for the dynamical characterization of nonlinear systems.

We have calculated the RQA measures, including the RTE for the standard map as a function of the nonlinearity parameter k and have shown that most of the measures capture the dynamical transition from regularity to chaos and vice-versa, however two of them stand out: the determinism (DET) and the RTE. Both of them yield a high correlation coefficient (either positive or negative) with the largest Lyapunov exponent, and it has been shown that DET detects the transitions along the orbit's evolution (*e.g.* dynamical trappings) (127). Therefore, as we sought a measure based on the intrinsic property of dynamical systems that quasiperiodic orbits can have at most three return times, we chose the RTE as our RP-based measure for the dynamical characterization of the standard map.

Our analysis has revealed that the RTE yields remarkably good results even considering relatively short time series (5000 data points). It successfully distinguishes periodicity, weak chaos (sticky orbits), and strong chaos. To identify the transitions a chaotic orbit experiences, we calculated the finite-time RTE throughout the orbit's evolution in windows of size $n \ll N$, $\{\text{RTE}^{(j)}(n)\}_{j=1,2,\dots,M}$, where N is the total length of the orbit and $M = N/n$. Interestingly, we have found the finite-time RTE distribution to be multi-modal, in contrast to the finite-time LE distribution [Figure 3.5(b)], which only displays two modes (54). Furthermore, we have identified the specific areas in phase space that correspond to the modes in the distribution, and calculated the trapping time in each one of these regions. We have shown that the cumulative distribution of trapping times exhibits a power law decay for the trapping in the sticky regions, and an exponential decay for when the orbit wanders in the bulk of the chaotic sea.

Finally, we introduced another class of Hamiltonian systems: the billiard system. It is one of the simplest dynamical systems to exhibit chaotic motion, and the manifestation of chaotic behavior within this system depends on the intricate geometric properties of its boundary. We have concentrated on a specific family of billiards characterized by two parameters: $\gamma \in \mathbb{Z}$ and $\xi > 0$. By changing these parameters, we have demonstrated the capability to transition from fully integrable billiards (the circle, with $\xi = 0$ for all γ and the triangle, with $\xi \rightarrow 1$,

and $\gamma = 3$) to billiards with mixed phase space (intermediate values of ξ). Next, we explored the quantification of chaotic behavior in this system using the dynamical measures we have applied to the standard map, namely, the largest Lyapunov exponent, λ_1 , the dig measure, and the RTE. Our findings indicate that λ_1 increases, on average, with ξ for all the analyzed values of γ . However, distinct behavior arises as ξ approaches 1, wherein λ_1 decreases due to the emergence of several islands of stability in phase space for $\gamma = 2$ and $\gamma = 3$. In this limiting case, for $\gamma = 2$, coexistence of islands and chaotic sea still persists, and the system exhibits a smaller yet positive value of λ_1 . Conversely, for $\gamma = 3$, the billiard takes the shape of an equilateral triangle featuring only periodic and quasiperiodic orbits, thereby causing λ_1 to approach 0.

To better comprehend the correspondence between λ_1 , the standard measure for quantifying chaotic motion, and the dig measure and RTE for the billiard system, we computed all three quantities for a grid of initial conditions in phase space. As with the standard map, both the dig measure and RTE stand as robust alternatives for detecting chaotic motion in phase space. The dig measure exhibits sometimes smaller values for regular solutions than it does for the standard map, however, by increasing the number of collisions, *i.e.*, the iteration time, it is expected that dig will converge for larger values in the regular regions. Nevertheless, even with the used number of collisions (2.0×10^4), it is still possible to distinguish regular and chaotic orbits with this measure as the chaotic orbits exhibit small values of dig. Lastly, the RTE remarkably distinguishes regular and chaotic behavior for this system considering relatively short time series (5000 data points) as it does for the standard map. Notably, these two metrics sidestep potential challenges associated with evaluating the Jacobian matrix, as their computation does not rely on it, and obtaining an analytical expression for the Jacobian matrix can at times be challenging and, in certain cases, even impossible.

The source code to reproduce the results presented in this thesis is freely available in the Zenodo archive (158) as well as in the GitHub repository (<https://github.com/mrolims/hamiltonian-systems>).

REFERENCES

- 1 ROVELLI, C. Aristotle's physics: A physicist's look. **Journal of the American Philosophical Association**, vol. 1, no. 1, p. 23–40, 2015.
- 2 DIXIT, U. S.; HAZARIKA, M.; DAVIM, J. P. **A Brief History of Mechanical Engineering**. 1st ed. Switzerland: Springer, 2017.
- 3 COXHEAD, M. A. A close examination of the pseudo-Aristotelian Mechanical Problems: The homology between mechanics and poetry as technē. **Studies in History and Philosophy of Science Part A**, vol. 43, no. 2, p. 300–306, 2012.
- 4 DUGAS, R. **A History of Mechanics**. 1st ed. New York: Dover Publications, 2011.
- 5 GOODMAN, L. E. **Avicenna**. 1st ed. New York: Routledge, 1992.
- 6 PALMIERI, P. Mental models in Galileo's early mathematization of nature. **Studies in History and Philosophy of Science Part A**, vol. 34, no. 2, p. 229–264, 2003.
- 7 GOLDSTEIN, H; POOLE, C.; SAFKO, J. **Classical Mechanics**. 3rd ed. Addison Wesley, 2002.
- 8 DE AGUIAR, M. A. M. **Tópicos de mecânica clássica**. 1st ed. São Paulo: Livraria da Física, 2011.
- 9 ARNOLD, V. I. **Mathematical methods of classical mechanics**. 1st ed. New York: Springer Science & Business Media, 2013.
- 10 LAPLACE, P. S. **Essai philosophique sur les probabilités**. 1st ed. Paris: Gauthier-Villars, 1814.
- 11 ARFKEN, G. B.; WEBER, H. J.; HARRIS, F. E. **Mathematical methods for physicists: a comprehensive guide**. 7th ed. Waltham: Academic press, 2012.
- 12 POINCARÉ, H. **Les méthodes nouvelles de la mécanique céleste**. 1st ed. Paris: Gauthier-Villars, 1899.
- 13 KOLMOGOROV, A. N. On conservation of conditionally periodic motions for a small change in Hamilton's function. **Dokl. Akad. Nauk SSSR**, vol. 98, p. 527–530, 1954.
- 14 MÖSER, J. On invariant curves of area-preserving mappings of an annulus. **Nachr. Akad. Wiss. Göttingen, II**, p. 1–20, 1962.

- 15 ARNOLD, V. I. Proof of a theorem of A. N. Kolmogorov on the invariance of quasi-periodic motions under small perturbations of the Hamiltonian. **Russian Mathematical Surveys**, vol. 18, no. 5, p. 9–36, 1963.
- 16 CORNFELD, I. P.; FOMIN, S. V.; SINAI, Y. G. **Ergodic theory**. 1st ed. New York: Springer-Verlag, 1982.
- 17 ARNOLD, V. I., Instability of dynamical systems with many degrees of freedom. **Doklady Akademii Nauk**, vol. 156, p. 9–12, 1964.
- 18 PEITGEN, H.-O.; JÜRGENS, H.; SAUPE, D. **Chaos and Fractals: New Frontiers of Science**. 2nd ed. New York: Springer-Verlag, 2004.
- 19 MACKAY, R. S.; MEISS, J. D.; PERCIVAL, I. C. Stochasticity and transport in Hamiltonian systems. **Physical Review Letters**, vol. 52, p. 697–700, 1984.
- 20 MACKAY, R. S.; MEISS, J. D.; PERCIVAL, I. C. Transport in Hamiltonian systems. **Physica D: Nonlinear Phenomena**, vol. 13, no. 1, p. 55–81, 1984.
- 21 UMBERGER, D. K.; FARMER, J. D. Fat fractals on the energy surface. **Physical Review Letters**, vol. 55, p. 661–664, 1985.
- 22 CONTOPOULOS, G. Orbits in highly perturbed dynamical systems. iii. nonperiodic orbits. **The Astronomical Journal**, vol. 76, p. 147, 1971.
- 23 KARNEY, C. F. F. Long-time correlations in the stochastic regime. **Physica D: Nonlinear Phenomena**, vol. 8, no. 3, p. 360–380, 1983.
- 24 MEISS, J. D.; CARY, J. R.; GREBOGI, C; CRAWFORD, J. D.; KAUFMAN, A. N.; ABARBANEL, H. D. Correlations of periodic, area-preserving maps. **Physica D: Nonlinear Phenomena**, vol. 6, no. 3, p. 375–384, 1983.
- 25 CHIRIKOV B. V.; SHEPELYANSKY, D. L. Correlation properties of dynamical chaos in Hamiltonian systems. **Physica D: Nonlinear Phenomena**, vol. 13, no. 3, p. 395–400, 1984.
- 26 ZASLAVSKY, G. M. Dynamical traps, **Physica D: Nonlinear Phenomena**, vol. 168-169, p. 292–304, 2002.
- 27 ZASLAVSKY, G. M. Chaos, fractional kinetics, and anomalous transport. **Physics Reports**, vol. 371, no. 6, p. 461–580, 2002.
- 28 CRISTADORO G.; KETZMERICK, R. Universality of algebraic decays in Hamiltonian systems. **Physical Review Letters**, vol. 100, p. 184101, 2008.

- 29 CONTOPOULOS G.; HARSOULA, M. Stickiness in chaos. **International Journal of Bifurcation and Chaos**, vol. 18, no. 10, p. 2929–2949, 2008.
- 30 CONTOPOULOS G.; HARSOULA, M. Stickiness effects in conservative systems. **International Journal of Bifurcation and Chaos**, vol. 20, no. 07, p. 2005–2043, 2010.
- 31 ALTMANN, E. G.; MOTTER, A. E.; KANTZ, H. Stickiness in mushroom billiards. **Chaos: An Interdisciplinary Journal of Nonlinear Science**, vol. 15, no. 3, p. 033105, 2005.
- 32 ALTMANN, E. G.; MOTTER, A. E.; KANTZ, H. Stickiness in Hamiltonian systems: From sharply divided to hierarchical phase space. **Physical Review E**, vol. 73, p. 026207, 2006.
- 33 BUNIMOVICH L. A.; VELA-AREVALO, L. V. Many faces of stickiness in Hamiltonian systems. **Chaos: An Interdisciplinary Journal of Nonlinear Science**, vol. 22, no. 2, p. 026103, 2012.
- 34 YOUNG, L.-S. Statistical properties of dynamical systems with some hyperbolicity. **Annals of Mathematics**, vol. 147, no. 3, p. 585–650, 1998.
- 35 HIRATA, M.; SAUSSOL, B.; VAIENTI, S. Statistics of return times: A general framework and new applications. **Communications in Mathematical Physics**, vol. 206, p. 33–55, Sep 1999.
- 36 COLLET, P.; ECKMANN, J.-P. **Iterated maps on the interval as dynamical systems**. 1st ed. New York: Springer Science & Business Media, 2009.
- 37 ARNOLD V. I.; AVEZ, A. **Ergodic problems of classical mechanics**. 1st ed. New York: Benjamin Inc, 1968.
- 38 VIVALDI, F.; CASATI, G.; GUARNERI, I. Origin of long-time tails in strongly chaotic systems. **Physical Review Letters**, vol. 51, p. 727–730, Aug 1983.
- 39 MEISS, J. D.; OTT, E. Markov tree model of transport in area-preserving maps. **Physica D: Nonlinear Phenomena**, vol. 20, no. 2, p. 387–402, 1986.
- 40 GRASSBERGER, P.; KANTZ, H. Universal scaling of long-time tails in Hamiltonian systems? **Physics Letters A**, vol. 113, no. 4, p. 167–171, 1985.
- 41 CHIRIKOV, B. V.; SHEPELYANSKY, D. L. Asymptotic statistics of poincaré recurrences in Hamiltonian systems with divided phase space. **Physical Review Letters**, vol. 82, p. 528–531, 1999.
- 42 WEISS, M; HUFNAGEL, L.; KETZMERICK, R. Can simple renormalization theories describe the trapping of chaotic trajectories in mixed systems? **Physical Review E**, vol. 67, p. 046209, 2003.

- 43 LOZEJ, Č.; ROBNIK, M. Structure, size, and statistical properties of chaotic components in a mixed-type Hamiltonian system. **Physical Review E**, vol. 98, p. 022220, 2018.
- 44 LOZEJ, Č. Stickiness in generic low-dimensional Hamiltonian systems: A recurrence-time statistics approach. **Physical Review E**, vol. 101, p. 052204, 2020.
- 45 LOZEJ, Č. **Transport and Localization in Classical and Quantum Billiards**. PhD thesis, Univerza v Mariboru (Slovenia), 2021.
- 46 ZASLAVSKY, G. M.; STEVENS, D.; WEITZNER, H. Self-similar transport in incomplete chaos. **Physical Review E**, vol. 48, p. 1683–1694, 1993.
- 47 ZASLAVSKY, G. M. Renormalization group theory of anomalous transport in systems with Hamiltonian chaos. **Chaos: An Interdisciplinary Journal of Nonlinear Science**, vol. 4, no. 1, p. 25–33, 1994.
- 48 ISHIZAKI, R.; HORITA, T.; KOBAYASHI, T.; MORI, H. Anomalous Diffusion Due to Accelerator Modes in the Standard Map. **Progress of Theoretical Physics**, vol. 85, no. 5, p. 1013–1022, 1991.
- 49 MANOS, T.; ROBNIK, M. Survey on the role of accelerator modes for anomalous diffusion: The case of the standard map. **Physical Review E**, vol. 89, p. 022905, 2014.
- 50 LOPES, S. R.; SZEZECH, J. D.; PEREIRA, R. F.; BERTOLAZZO, A. A.; VIANA, R. L. Anomalous transport induced by nonhyperbolicity. **Physical Review E**, vol. 86, p. 016216, 2012.
- 51 SHIMADA, I.; NAGASHIMA, T. A Numerical Approach to Ergodic Problem of Dissipative Dynamical Systems. **Progress of Theoretical Physics**, vol. 61, no. 6, p. 1605–1616, 1979.
- 52 BENETTIN, G.; GALGANI, L.; GIORGILLI, A.; STRELCYN, J.-M. Lyapunov characteristic exponents for smooth dynamical systems and for Hamiltonian systems; a method for computing all of them. part 1: Theory. **Meccanica**, vol. 15, no. 1, p. 9–20, 1980.
- 53 WOLF, A.; SWIFT, J. B.; SWINNEY, H. L.; VASTANO, J. A. Determining Lyapunov exponents from a time series. **Physica D: Nonlinear Phenomena**, vol. 16, no. 3, p. 285–317, 1985.
- 54 SZEZECH, J. D.; LOPES, S. R.; VIANA, R. L. Finite-time Lyapunov spectrum for chaotic orbits of non-integrable Hamiltonian systems. **Physics Letters A**, vol. 335, no. 5, p. 394–401, 2005.

- 55 DA SILVA, R. M.; MANCHEIN, C.; BEIMS, M. W.; ALTMANN, E. G. Characterizing weak chaos using time series of Lyapunov exponents. **Physical Review E**, vol. 91, p. 062907, 2015.
- 56 ABUD C. V.; DE CARVALHO, R. E. Multifractality, stickiness, and recurrence-time statistics. **Physical Review E**, vol. 88, p. 042922, 2013.
- 57 SZEZECH, J. D.; SCHELIN, A. B.; CALDAS, I. L.; LOPES, S. R.; MORRISON, P. J.; VIANA, R. L. Finite-time rotation number: A fast indicator for chaotic dynamical structures. **Physics Letters A**, vol. 377, no. 6, p. 452–456, 2013.
- 58 SANTOS, M. S.; MUGNAINE, M.; SZEZECH, J. D.; BATISTA, A. M.; CALDAS, I. L.; VIANA, R. L. Using rotation number to detect sticky orbits in Hamiltonian systems. **Chaos: An Interdisciplinary Journal of Nonlinear Science**, vol. 29, no. 4, p. 043125, 2019.
- 59 CHIRIKOV, B. V. A universal instability of many-dimensional oscillator systems. **Physics Reports**, vol. 52, no. 5, p. 263–379, 1979.
- 60 LEVNAJIĆ, Z.; MEZIĆ, I. Ergodic theory and visualization. i. mesochronic plots for visualization of ergodic partition and invariant sets. **Chaos: An Interdisciplinary Journal of Nonlinear Science**, vol. 20, no. 3, p. 033114, 2010.
- 61 LEVNAJIĆ, Z.; MEZIĆ, I. Ergodic theory and visualization. ii. fourier mesochronic plots visualize (quasi)periodic sets. **Chaos: An Interdisciplinary Journal of Nonlinear Science**, vol. 25, no. 5, p. 053105, 2015.
- 62 DAS, S.; DOCK, C. B.; SAIKI, Y.; SALGADO-FLORES, M.; SANDER, E.; WU, J.; YORKE, J. A. Measuring quasiperiodicity. **Europhysics Letters**, vol. 114, no. 4, p. 40005, 2016.
- 63 DAS, S.; SAIKI, Y.; SANDER, E.; YORKE, J. A. Quantitative quasiperiodicity. **Nonlinearity**, vol. 30, no. 11, p. 4111–4140, 2017.
- 64 DAS, S.; YORKE, J. A. Super convergence of ergodic averages for quasiperiodic orbits. **Nonlinearity**, vol. 31, no. 2, p. 491–501, 2018.
- 65 SANDER, E.; MEISS, J. D. Birkhoff averages and rotational invariant circles for area-preserving maps. **Physica D: Nonlinear Phenomena**, vol. 411, p. 132569, 2020.
- 66 MEISS, J. D.; SANDER, E. Birkhoff averages and the breakdown of invariant tori in volume-preserving maps. **Physica D: Nonlinear Phenomena**, vol. 428, p. 133048, 2021.
- 67 DUIGNAN, N.; MEISS, J. D. Distinguishing between regular and chaotic orbits of flows by the weighted birkhoff average. **Physica D: Nonlinear Phenomena**, vol. 449, p. 133749, 2023.

- 68 LITTLE, M. A.; MCSHARRY, P. E.; ROBERTS, S. J.; COSTELLO, D. A.; MOROZ, I. M. Exploiting nonlinear recurrence and fractal scaling properties for voice disorder detection. **BioMedical Engineering OnLine**, vol. 6, no. 1, p. 23, 2007.
- 69 NGAMGA, E. J.; SENTHILKUMAR, D. V.; PRASAD, A.; PARMANANDA, P.; MARWAN, N.; KURTHS, J. Distinguishing dynamics using recurrence-time statistics. **Physical Review E**, vol. 85, p. 026217, 2012.
- 70 KRAEMER, K. H.; DONNER, R. V.; HEITZIG, J.; MARWAN, N. Recurrence threshold selection for obtaining robust recurrence characteristics in different embedding dimensions. **Chaos: An Interdisciplinary Journal of Nonlinear Science**, vol. 28, no. 8, p. 085720, 2018.
- 71 ECKMANN, J.-P.; KAMPHORST, S. O.; RUELLE, D. Recurrence plots of dynamical systems. **Europhysics Letters**, vol. 4, no. 9, p. 973, 1987.
- 72 MARWAN, N.; CARMEN ROMANO, M.; THIEL, M.; KURTHS, J. Recurrence plots for the analysis of complex systems. **Physics Reports**, vol. 438, no. 5, p. 237–329, 2007.
- 73 MARWAN, N.; DONGES, J. F.; ZOU, Y.; DONNER, R. V.; KURTHS, J. Complex network approach for recurrence analysis of time series. **Physics Letters A**, vol. 373, no. 46, p. 4246–4254, 2009.
- 74 DONNER, R. V.; SMALL, M.; DONGES, J. F.; MARWAN, N.; ZOU, Y.; XIANG, R.; KURTHS, J. Recurrence-based time series analysis by means of complex network methods. **International Journal of Bifurcation and Chaos**, vol. 21, no. 04, p. 1019–1046, 2011.
- 75 MARWAN, N.; WEBBER, C. L. Mathematical and Computational Foundations of Recurrence Quantifications. *In*: MARWAN, N.; WEBBER, C. L. **Recurrence Quantification Analysis**. 1st ed. Switzerland: Springer Cham, 2015, chap. 1, p. 3-43.
- 76 ZOU, Y.; DONNER, R. V.; MARWAN, N.; DONGES, J. F.; KURTHS, J. Complex network approaches to nonlinear time series analysis. **Physics Reports**, vol. 787, p. 1–97, 2019.
- 77 SLATER, N. B. The distribution of the integers n for which $\theta n < \varphi$. **Mathematical Proceedings of the Cambridge Philosophical Society**, vol. 46, no. 4, p. 525–534, 1950.
- 78 SLATER, N. B. Gaps and steps for the sequence $n\theta \bmod 1$. **Mathematical Proceedings of the Cambridge Philosophical Society**, vol. 63, no. 4, p. 1115–1123, 1967.
- 79 MAYER, D. H. On the distribution of recurrence times in nonlinear systems. **Letters in Mathematical Physics**, vol. 16, no. 2, p. 139–143, 1988.
- 80 LICHTENBERG, A. J.; LIEBERMAN, M. A. **Regular and chaotic dynamics**. 2nd ed. New York: Springer-Verlag, 1992.

- 81 OTT, E. **Chaos in Dynamical Systems**. 2nd ed. Cambridge: Cambridge University Press, 2002.
- 82 ZASLAVSKY, G. M. **Hamiltonian Chaos and Fractional Dynamics**. Oxford: Oxford University Press, 2005.
- 83 TÉL, T.; GRUIZ, M. **Chaotic Dynamics: An Introduction Based on Classical Mechanics**. 1st ed. New York: Cambridge University Press, 2006.
- 84 MONTEIRO, L. H. A. **Sistemas Dinâmicos**. 3rd ed. São Paulo: Editora Livraria da Física, 2011.
- 85 ECKMANN, J. P.; RUELLE, D. Ergodic theory of chaos and strange attractors. **Reviews of Modern Physics**, vol. 57, p. 617–656, 1985.
- 86 ZASLAVSKIĬ, G. M.; CHIRIKOV, B. V. Stochastic instability of non-linear oscillations. **Soviet Physics Uspekhi**, vol. 14, no. 5, p. 549, 1972.
- 87 ZASLAVSKY, G. M. Fractional kinetic equation for Hamiltonian chaos. **Physica D: Non-linear Phenomena**, vol. 76, no. 1, p. 110–122, 1994.
- 88 ZASLAVSKY, G. M.; EDELMAN, M.; NIYAZOV, B. A. Self-similarity, renormalization, and phase space nonuniformity of Hamiltonian chaotic dynamics. **Chaos: An Interdisciplinary Journal of Nonlinear Science**, vol. 7, no. 1, p. 159–181, 1997.
- 89 GREENE, J. M. A method for determining a stochastic transition. **Journal of Mathematical Physics**, vol. 20, no. 6, p. 1183–1201, 1979.
- 90 GREENE, J. M. Two-Dimensional Measure-Preserving Mappings. **Journal of Mathematical Physics**, vol. 9, no. 5, p. 760–768, 1968.
- 91 HARSOULA, M.; KARAMANOS, K.; CONTOPOULOS, G. Characteristic times in the standard map. **Physical Review E**, vol. 99, p. 032203, 2019.
- 92 MANCHEIN, C.; BEIMS, M. W. Conservative generalized bifurcation diagrams. **Physics Letters A**, vol. 377, no. 10, p. 789–793, 2013.
- 93 KOLMOGOROV, A. N. On the analytic methods of probability theory. **Uspekhi Mat. Nauk**, no. 5, p. 5–41, 1938.
- 94 RISKEN, H. **The Fokker-Planck Equation – Methods of Solution and Applications**. 2nd ed. Heidelberg: Springer Berlin, 1996.
- 95 IZRAILEV, F. M. Simple models of quantum chaos: Spectrum and eigenfunctions. **Physics Reports**, vol. 196, no. 5, p. 299–392, 1990.

- 96 VENEGEROLES, R. Calculation of superdiffusion for the Chirikov-Taylor model. **Physical Review Letters**, vol. 101, p. 054102, 2008.
- 97 HARSOULA, M.; CONTOPOULOS, G. Global and local diffusion in the standard map. **Physical Review E**, vol. 97, p. 022215, 2018.
- 98 CONTOPOULOS, G.; HARSOULA, M.; DVORAK, R.; FREISTETTER, F. Recurrence of order in chaos. **International Journal of Bifurcation and Chaos**, vol. 15, no. 09, p. 2865–2882, 2005.
- 99 BENKADDA, S.; KASSIBRAKIS, S.; WHITE, R. B.; ZASLAVSKY, G. M. Self-similarity and transport in the standard map. **Physical Review E**, vol. 55, p. 4909–4917, 1997.
- 100 SILVERMAN, L. On the notion of summability for the limit of a function of a continuous variable. **Transactions of the American Mathematical Society**, vol. 17, no. 3, p. 284–294, 1916.
- 101 GREBOGI, C.; MCDONALD, S. W.; OTT, E.; YORKE, J. A. Final state sensitivity: An obstruction to predictability. **Physics Letters A**, vol. 99, no. 9, p. 415–418, 1983.
- 102 MCDONALD, S. W.; GREBOGI, C.; OTT, E.; YORKE, J. A. Fractal basin boundaries. **Physica D: Nonlinear Phenomena**, vol. 17, no. 2, p. 125–153, 1985.
- 103 GREBOGI, C.; OTT, E.; YORKE, J. A. Chaos, strange attractors, and fractal basin boundaries in nonlinear dynamics. **Science**, vol. 238, no. 4827, p. 632–638, 1987.
- 104 GREBOGI, C.; OTT, E.; YORKE, J. A. Basin boundary metamorphoses: Changes in accessible boundary orbits. **Physica D: Nonlinear Phenomena**, vol. 24, no. 1, p. 243–262, 1987.
- 105 BLEHER, S.; GREBOGI, C.; OTT, E.; BROWN, R. Fractal boundaries for exit in Hamiltonian dynamics. **Physical Review A**, vol. 38, p. 930–938, 1988.
- 106 AGUIRRE, J.; VALLEJO, J. C.; SANJUÁN, M. A. F. Wada basins and chaotic invariant sets in the Hénon-Heiles system. **Physical Review E**, vol. 64, p. 066208, 2001.
- 107 MUGNAINE, M.; MATHIAS, A. C.; SANTOS, M. S.; BATISTA, A. M.; SZEZECH, J. D.; VIANA, R. L. Dynamical characterization of transport barriers in nontwist Hamiltonian systems. **Physical Review E**, vol. 97, p. 012214, 2018.
- 108 MATHIAS, A. C.; MUGNAINE, M.; SANTOS, M. S.; SZEZECH, J. D.; CALDAS, I. L.; VIANA, R. L.; Fractal structures in the parameter space of nontwist area-preserving maps. **Physical Review E**, vol. 100, p. 052207, 2019.

- 109 AGUIRRE, J.; VIANA, R. L.; SANJUÁN, M. A. F. Fractal structures in nonlinear dynamics. **Reviews of Modern Physics**, vol. 81, p. 333–386, 2009.
- 110 MEISS, J. D. Class renormalization: Islands around islands. **Physical Review A**, vol. 34, p. 2375–2383, 1986.
- 111 DE MOURA, A. P. S.; GREBOGI, C. Reactions in flows with nonhyperbolic dynamics. **Physical Review E**, vol. 70, p. 036216, 2004.
- 112 MOTTER, A. E.; DE MOURA, A. P. S.; GREBOGI, C.; KANTZ, H. Effective dynamics in Hamiltonian systems with mixed phase space. **Physical Review E**, vol. 71, p. 036215, 2005.
- 113 AREF, H.; BLAKE, J. R.; BUDIŠIĆ, M.; CARDOSO, S. S. S.; CARTWRIGHT, J. H. E.; CLERCX, H. J. H.; EL OMARI, K.; FEUDEL, U.; GOLESTANIAN, R.; GOUILLART, E.; VAN HEIJST, G. F.; KRASNOPOLSKAYA, T. S.; LE GUER, Y.; MACKAY, R. S.; MELESHKO, V. V.; METCALFE, G.; MEZIĆ, I.; DE MOURA, A. P. S.; PIRO, O.; SPEETJENS, M. F. M.; STURMAN, R.; THIFFEAULT, J.-L.; TUVAL, I. Frontiers of chaotic advection. **Reviews of Modern Physics**, vol. 89, p. 025007, 2017.
- 114 OTT, E.; SOMMERER, J. C. Blowout bifurcations: the occurrence of riddled basins and on-off intermittency. **Physics Letters A**, vol. 188, no. 1, p. 39–47, 1994.
- 115 THIEL, M.; ROMANO, M.; KURTHS, J.; MEUCCI, R.; ALLARIA, E.; ARECCHI, F. Influence of observational noise on the recurrence quantification analysis. **Physica D: Nonlinear Phenomena**, vol. 171, no. 3, p. 138–152, 2002.
- 116 MINDLIN, G. M.; GILMORE, R. Topological analysis and synthesis of chaotic time series. **Physica D: Nonlinear Phenomena**, vol. 58, no. 1, p. 229–242, 1992.
- 117 ZBILUT, J. P.; WEBBER, C. L. Embeddings and delays as derived from quantification of recurrence plots. **Physics Letters A**, vol. 171, no. 3, p. 199–203, 1992.
- 118 ZBILUT, J. P.; ZALDIVAR-COMENEGES, J.-M.; STROZZI, F. Recurrence quantification based Liapunov exponents for monitoring divergence in experimental data. **Physics Letters A**, vol. 297, no. 3, p. 173–181, 2002.
- 119 MEDRANO, J.; KHEDDAR, A.; LESNE, A.; RAMDANI, S. Radius selection using kernel density estimation for the computation of nonlinear measures. **Chaos: An Interdisciplinary Journal of Nonlinear Science**, vol. 31, no. 8, p. 083131, 2021.
- 120 MARWAN, N.; WESSEL, N.; MEYERFELDT, U.; SCHIRDEWAN, A.; KURTHS, J. Recurrence-plot-based measures of complexity and their application to heart-rate-variability data. **Physical Review E**, vol. 66, p. 026702, 2002.

- 121 GAO, J.; CAI, H. On the structures and quantification of recurrence plots. **Physics Letters A**, vol. 270, no. 1, p. 75–87, 2000.
- 122 ZOU, Y.; PAZÓ, D.; ROMANO, M. C.; THIEL, M.; KURTHS, J. Distinguishing quasiperiodic dynamics from chaos in short-time series. **Physical Review E**, vol. 76, p. 016210, 2007.
- 123 HARRIS, C. R.; MILLMAN, K. J.; VAN DER WALT, S. J.; GOMMERS, R.; VIRTANEN, P.; COUNAPEAU, D.; WIESER, E.; TAYLOR, J.; BERG, S.; SMITH, N. J.; KERN, R.; PICUS, M.; HOYER, S.; VAN KERKWIJK, M. H.; BRETT, M.; HALDANE, A.; DEL RÍO, J. F.; WIEBE, M.; PETERSON, P.; GÉRARD-MARCHANT, P.; SHEPPARD, K.; REDDY, T.; WECKESSER, W.; ABBASI, H.; GOHLKE, C.; OLIPHANT, T. E. Array programming with numpy. **Nature**, vol. 585, no. 7825, p. 357–362, 2020.
- 124 WEBBER, C. L.; ZBILUT, J. P. Dynamical assessment of physiological systems and states using recurrence plot strategies. **Journal of Applied Physiology**, vol. 76, no. 2, p. 965–973, 1994.
- 125 ZBILUT, J. P.; WEBBER, C. L. Recurrence quantification analysis: Introduction and historical context. **International Journal of Bifurcation and Chaos**, vol. 17, no. 10, p. 3477–3481, 2007.
- 126 ZOU, Y. **Exploring recurrences in quasiperiodic dynamical systems**. PhD thesis, Universität Potsdam, 2007.
- 127 ZOU, Y.; THIEL, M.; ROMANO, M. C.; KURTHS, J. Characterization of stickiness by means of recurrence. **Chaos: An Interdisciplinary Journal of Nonlinear Science**, vol. 17, no. 4, p. 043101, 2007.
- 128 MUGNAINE, M.; SALES, M. R.; SZEZECH, J. D.; VIANA, R. L. Dynamics, multistability, and crisis analysis of a sine-circle nontwist map. **Physical Review E**, vol. 106, p. 034203, 2022.
- 129 BAPTISTA, M.; NGAMGA, E.; PINTO, P. R.; BRITO, M.; KURTHS, J. Kolmogorov–sinai entropy from recurrence times. **Physics Letters A**, vol. 374, no. 9, p. 1135–1140, 2010.
- 130 SHIOZAWA, K.; UEMURA, T.; TOKUDA, I. T. Detecting the dynamical instability of complex time series via partitioned entropy. **Physical Review E**, vol. 107, p. 014207, 2023.
- 131 KRAEMER, K. H.; MARWAN, N. Border effect corrections for diagonal line based recurrence quantification analysis measures. **Physics Letters A**, vol. 383, no. 34, p. 125977, 2019.

- 132 PALMERO, M. S.; CALDAS, I. L.; SOKOLOV, I. M. Finite-time recurrence analysis of chaotic trajectories in Hamiltonian systems. **Chaos: An Interdisciplinary Journal of Nonlinear Science**, vol. 32, no. 11, p. 113144, 2022.
- 133 HARLE, M.; FEUDEL, U. Hierarchy of islands in conservative systems yields multimodal distributions of ftles. **Chaos, Solitons & Fractals**, vol. 31, no. 1, p. 130–137, 2007.
- 134 KRÜGER, T. S.; GALUZIO, P. P.; PRADO, T. D. L.; VIANA, R. L.; SZEZECH, J. D.; LOPES, S. R. Mechanism for stickiness suppression during extreme events in Hamiltonian systems. **Physical Review E**, vol. 91, p. 062903, 2015.
- 135 LAI, Y. C.; GREBOGI, C.; YORKE, J. A.; KAN, I. How often are chaotic saddles nonhyperbolic? **Nonlinearity**, vol. 6, no. 5, p. 779, 1993.
- 136 ANISHCHENKO, V.; KOPEIKIN, A.; KURTHS, J.; VADIVASOVA, T.; STRELKOVA, G. Studying hyperbolicity in chaotic systems. **Physics Letters A**, vol. 270, no. 6, p. 301–307, 2000.
- 137 TABACHNIKOV, S. **Geometry and billiards**. 1st ed. Providence: American Mathematical Society, 2005.
- 138 BUNIMOVICH, L. A. Mechanisms of chaos in billiards: dispersing, defocusing and nothing else. **Nonlinearity**, vol. 31, no. 2, p. R78, 2018.
- 139 SINAI, Y. G. Dynamical systems with elastic reflections. **Russian Mathematical Surveys**, vol. 25, no. 2, p. 137, 1970.
- 140 BUNIMOVICH, L. A. On ergodic properties of certain billiards. **Functional Analysis and Its Applications**, vol. 8, no. 3, p. 254–255, 1974.
- 141 HANSEN, M.; DA COSTA, D. R.; CALDAS, I. L.; LEONEL, E. D. Statistical properties for an open oval billiard: An investigation of the escaping basins. **Chaos, Solitons & Fractals**, vol. 106, p. 355–362, 2018.
- 142 DA COSTA, D. R.; FUJITA, A.; BATISTA, A. M.; SALES, M. R.; SZEZECH JR, J. D. Conservative generalized bifurcation diagrams and phase space properties for oval-like billiards. **Chaos, Solitons & Fractals**, vol. 155, p. 111707, 2022.
- 143 BUNIMOVICH, L. A. Mushrooms and other billiards with divided phase space. **Chaos: An Interdisciplinary Journal of Nonlinear Science**, vol. 11, no. 4, p. 802–808, 2001.
- 144 DA COSTA, D. R.; PALMERO, M. S.; MÉNDEZ-BERMÚDEZ, J.; IAROSZ, K. C.; SZEZECH JR, J. D.; BATISTA, A. M. Tilted-hat mushroom billiards: Web-like hierarchical mixed phase space. **Communications in Nonlinear Science and Numerical Simulation**, vol. 91, p. 105440, 2020.

- 145 CUSTÓDIO, M. S.; BEIMS, M. W. Intrinsic stickiness and chaos in open integrable billiards: Tiny border effects. **Physical Review E**, vol. 83, p. 056201, 2011.
- 146 BARNETT, A. H.; BETCKE, T. Quantum mushroom billiards. **Chaos: An Interdisciplinary Journal of Nonlinear Science**, vol. 17, no. 4, p. 043125, 2007.
- 147 DE MENEZES, D. D.; JAR E SILVA, M.; DE AGUIAR, F. M. Numerical experiments on quantum chaotic billiards. **Chaos: An Interdisciplinary Journal of Nonlinear Science**, vol. 17, no. 2, p. 023116, 2007.
- 148 ZANETTI, F. M.; VICENTINI, E.; DA LUZ, M. Eigenstates and scattering solutions for billiard problems: A boundary wall approach. **Annals of Physics**, vol. 323, no. 7, p. 1644–1676, 2008.
- 149 ZANETTI, F. M.; LYRA, M. L.; DE MOURA, F. A. B. F.; DA LUZ, M. G. E. Resonant scattering states in 2d nanostructured waveguides: a boundary wall approach. **Journal of Physics B: Atomic, Molecular and Optical Physics**, vol. 42, no. 2, p. 025402, 2008.
- 150 SALES, M. R.; AZEVEDO, A. L.; TESTON, F.; DA LUZ, M. G. E.; ZANETTI, F. M. Soliton-like structures in the spectrum and the corresponding eigenstates morphology for the quantum desymmetrized Sinai billiard. **Chaos: An Interdisciplinary Journal of Nonlinear Science**, vol. 31, no. 11, p. 113122, 2021.
- 151 CASATI, G.; PROSEN, T. The quantum mechanics of chaotic billiards. **Physica D: Nonlinear Phenomena**, vol. 131, no. 1, p. 293–310, 1999. Classical Chaos and its Quantum Manifestations.
- 152 JENSEN, R. V. Quantum chaos. **Nature**, vol. 355, no. 6358, p. 311–318, 1992.
- 153 BERRY, M. Quantum chaology, not quantum chaos. **Physica Scripta**, vol. 40, p. 335, 1989.
- 154 BERRY, M. V. Regularity and chaos in classical mechanics, illustrated by three deformations of a circular 'billiard'. **European Journal of Physics**, vol. 2, no. 2, p. 91, 1981.
- 155 ARITA, K.-I.; BRACK, M. Anomalous shell effect in the transition from a circular to a triangular billiard. **Physical Review E**, vol. 77, p. 056211, 2008.
- 156 FRANCISCO, M. H. **Propriedades Estatísticas e Termodinâmicas de Bilhares Clássicos**. PhD thesis, Universidade de São Paulo, 2019.
- 157 SIMILE BARONI, R.; EGYDIO DE CARVALHO, R.; CASTALDI, B.; FURLANETTO, B. Time recurrence analysis of a near singular billiard. **Mathematical and Computational Applications**, vol. 24, no. 2, 2019.
- 158 SALES, M. R. mrolims/hamiltonian-systems: v1.1. Zenodo, Aug. 29, 2023. doi: 10.5281/zenodo.8298663.

APPENDIX A – PUBLISHED PAPERS

During my doctoral period, I participated in several scientific publications, both developed by myself and by other students and researchers. The scientific papers as first author are:

1. **M. R. Sales**, A. L. Azevedo, F. Teston, M. G. E. da Luz, and F. M. Zanetti, “Soliton-like structures in the spectrum and the corresponding eigenstates morphology for the quantum desymmetrized Sinai billiard,” *Chaos: An Interdisciplinary Journal of Nonlinear Science*, vol. 31, no. 11, p. 113122, 2021.


Chaos
ARTICLE
scitation.org/journal/cha

Soliton-like structures in the spectrum and the corresponding eigenstates morphology for the quantum desymmetrized Sinai billiard

Cite as: Chaos 31, 113122 (2021); doi: 10.1063/5.0063628

Submitted: 15 July 2021 · Accepted: 19 October 2021 ·

Published Online: 9 November 2021



M. R. Sales,^a A. L. Azevedo, F. Teston, M. G. E. da Luz,^b and F. M. Zanetti

AFFILIATIONS

Departamento de Física, Universidade Federal do Paraná, Curitiba, PR 81531-980, Brazil

^a Present address: Departamento de Física, Universidade Estadual de Ponta Grossa, Ponta Grossa, PR 84030-900, Brazil.


^b Author to whom correspondence should be addressed: luz@fisica.ufpr.br

ABSTRACT

By continuously varying certain geometric parameters γ of the totally desymmetrized quantum Sinai billiard, we study the formation of the so-called soliton-like structures in the spectra of the resulting family of systems. We present a detailed characterization of the eigenstate ψ_n morphologies along such structures. Usually, scarring and bouncing ball mode states are expected to fully explain the solitons. However, we show that they do not exhaust all the possibilities. States with strong resemblance to very particular solutions of the associated integrable case (45°–45° right triangle) also account for the ψ_n 's. We argue that for the emergence of the solitons, in fact, there must be an interplay between the spatial localization properties of the soliton-related ψ_n 's and the rescaling properties of the billiards with γ . This is illustrated, e.g., by comparing the behavior of the eigenwavelengths along the solitons and the billiard size dependence on γ . Considerations on how these findings could extend to other type of billiards are also briefly addressed.

Published under an exclusive license by AIP Publishing. <https://doi.org/10.1063/5.0063628>


2. **M. R. Sales**, M. Mugnaine, R. L. Viana, I. L. Caldas, and J. D. Szezech, “Unpredictability in Hamiltonian systems with a hierarchical phase space,” *Physics Letters A*, vol. 431, p. 127991, 2022.



Contents lists available at ScienceDirect

Physics Letters A

www.elsevier.com/locate/pla



Unpredictability in Hamiltonian systems with a hierarchical phase space

Matheus R. Sales^a, Michele Mugnaine^b, Ricardo L. Viana^b, Iberê L. Caldas^c, José D. Szezech Jr.^{a,d,*}

^a Postgraduate Program in Physics, State University of Ponta Grossa, 84030-900, Ponta Grossa, PR, Brazil
^b Department of Physics, Federal University of Paraná, 80060-000, Curitiba, PR, Brazil
^c Institute of Physics, University of São Paulo, 05508-900, São Paulo, SP, Brazil
^d Department of Mathematics and Statistics, State University of Ponta Grossa, 84030-900, Ponta Grossa, PR, Brazil

ARTICLE INFO

Article history:

Received 22 October 2021

Received in revised form 1 February 2022

Accepted 4 February 2022

Available online 10 February 2022

Communicated by M. Perc

Keywords:

Uncertainty exponent

Stickiness

Conservative chaos

Weighted Birkhoff averages

ABSTRACT

One of the main consequences of the complex hierarchical structure of chaotic regions and stability islands in the phase space of a typical nonlinear Hamiltonian system is the phenomenon of stickiness. The chaotic orbits that approach an island are trapped in its neighborhood for arbitrarily long times, in which the orbits behave similarly as quasiperiodic orbits. In this paper, we characterize the boundary between chaos and regular motion in the phase space of the standard map for distinct parameter values. The orbits are distinguished between regular and chaotic employing a recently proposed method of weighted Birkhoff averages. We quantify the dimension of the boundaries of the islands using the uncertainty exponent. In our simulations, we show that the dimension of the island's boundary depends on the scale of the initial condition uncertainty and the level of the hierarchical structure. We also show that the trapping in the vicinity of the islands causes an obstruction in the predictability of the final state of an orbit. We present how this loss of predictability results in larger dimensions at the inner levels of the islands.

© 2022 Elsevier B.V. All rights reserved.

3. **M. R. Sales**, M. Mugnaine, J. Szezech, José D., R. L. Viana, I. L. Caldas, N. Marwan, and J. Kurths, “Stickiness and recurrence plots: An entropy-based approach,” *Chaos: An Interdisciplinary Journal of Nonlinear Science*, vol. 33, no. 3, p. 033140, 2023.

Chaos
ARTICLE
scitation.org/journal/cha

Stickiness and recurrence plots: An entropy-based approach

Cite as: *Chaos* 33, 033140 (2023); doi: 10.1063/5.0140613

Submitted: 29 December 2022 · Accepted: 3 March 2023 ·

Published Online: 22 March 2023

Matheus R. Sales,^{1,2,3,4} Michele Mugnaine,^{1,5} José D. Szezech, Jr.,^{1,6} Ricardo L. Viana,^{4,5} Iberê L. Caldas,³ Norbert Marwan,⁷ and Jürgen Kurths^{2,7*}

AFFILIATIONS

¹Graduate Program in Sciences/Physics, State University of Ponta Grossa, 84030-900 Ponta Grossa, PR, Brazil

²Potsdam Institute for Climate Impact Research, Member of the Leibniz Association, P.O. Box 6012 03, D-14412 Potsdam, Germany

³Institute of Mathematics, Humboldt University Berlin, 12489 Berlin, Germany

⁴Department of Physics, Federal University of Paraná, 80060-000 Curitiba, PR, Brazil

⁵Institute of Physics, University of São Paulo, 05508-900 São Paulo, SP, Brazil

⁶Department of Mathematics and Statistics, State University of Ponta Grossa, 84030-900 Ponta Grossa, PR, Brazil

⁷Institute of Physics, Humboldt University Berlin, 10099 Berlin, Germany

^{*}Division of Dynamics, Lodz University of Technology, Stefanowskiego 1/15, 90-924 Lodz, Poland

Author to whom correspondence should be addressed: matheusrolim95@gmail.com

ABSTRACT

The stickiness effect is a fundamental feature of quasi-integrable Hamiltonian systems. We propose the use of an entropy-based measure of the recurrence plots (RPs), namely, the entropy of the distribution of the recurrence times (estimated from the RP), to characterize the dynamics of a typical quasi-integrable Hamiltonian system with coexisting regular and chaotic regions. We show that the recurrence time entropy (RTE) is positively correlated to the largest Lyapunov exponent, with a high correlation coefficient. We obtain a multi-modal distribution of the finite-time RTE and find that each mode corresponds to the motion around islands of different hierarchical levels.

© 2023 Author(s). All article content, except where otherwise noted, is licensed under a Creative Commons Attribution (CC BY) license (<http://creativecommons.org/licenses/by/4.0/>). <https://doi.org/10.1063/5.0140613>

The remaining papers are:

4. D. R. da Costa, A. Fujita, A. M. Batista, **M. R. Sales**, and J. D. Szezech Jr, “Conservative generalized bifurcation diagrams and phase space properties for oval-like billiards,” *Chaos, Solitons & Fractals*, vol. 155, p. 111707, 2022.

Contents lists available at ScienceDirect

Chaos, Solitons and Fractals

Nonlinear Science, and Nonequilibrium and Complex Phenomena

journal homepage: www.elsevier.com/locate/chaos

Frontiers

Conservative generalized bifurcation diagrams and phase space properties for oval-like billiards

Diogo Ricardo da Costa^{a,b,*}, André Fujita^b, Antonio Marcos Batista^{c,d}, Matheus Rolim Sales^d, José Danilo Szezech Jr^{c,d}

^aDepartment of Physics, Federal University of Paraná, CEP Curitiba/PR, 80060-000, Brazil

^bDepartment of Computer Science, Institute of Mathematics and Statistics, University of São Paulo, CEP São Paulo/SP, 05508-090, Brazil

^cDepartment of Mathematics and Statistics, State University of Ponta Grossa, CEP Ponta Grossa/PR, 84030-900, Brazil

^dGraduate in Science Program - Physics, State University of Ponta Grossa, CEP Ponta Grossa/PR, 84030-900, Brazil

ARTICLE INFO

Article history:

Received 21 April 2021

Revised 1 December 2021

Accepted 2 December 2021

Available online 20 December 2021

Keywords:

Oval-like billiards

Nonlinear dynamics

Chaotic system

CGBD plot

ABSTRACT

In this paper, we study some dynamic properties for oval-like billiards. These billiards have two control parameters, named ϵ , which controls the deformation of the boundary, and p , which changes the number of inflection points. The particle's position (X, Y) uses Cartesian coordinates, and the angle μ gives us the particle's direction. Here we consider a Poincaré section, where we calculate the position X (in the horizontal axis) and angle μ every time a particle crosses $Y = 0$ (in the vertical axis). We compute the phase space and the conservative generalized bifurcation diagrams (CGBD). These diagrams are obtained when changing the initial position X and the control parameter ϵ . We plot the respective maximum Lyapunov exponent for each combination of the control parameter and initial condition, which uses a customized color palette. These diagrams show how complex billiards dynamics are, where one can find the direct and inverse parabolic bifurcations. Moreover, one can highlight periodic, quasi-periodic, and chaotic regions. We found a fractal behavior (self-similar structure), where we verified the existence of period-adding structures logical sequences (periodic orbits) in the CGBD. These sequences accumulate in different regions depending on the control parameters, following the main body's period and accumulating in different regions. When we set the control parameter p to 1, we observe that chaos dominates for a high enough value of the control parameter ϵ (which controls our billiard's deformation). We also studied some orbits embedded in stochastic layers that appear near saddle points, which obey another period-adding logical sequence. These stochastic layers play a crucial role in the dynamics of billiard systems because that chaos grows in such regions, near saddle points, after increasing the control parameter's value.

© 2021 Elsevier Ltd. All rights reserved.

5. D. R. da Costa, A. Fujita, **M. R. Sales**, J. D. Szezech Jr, and A. M. Batista, “Dynamical properties for a tunable circular to polygonal billiard,” *Brazilian Journal of Physics*, vol. 52, no. 3, p. 75, 2022.

Brazilian Journal of Physics (2022) 52: 75
<https://doi.org/10.1007/s13538-022-01075-x>



GENERAL AND APPLIED PHYSICS



Dynamical Properties for a Tunable Circular to Polygonal Billiard

Diogo Ricardo da Costa^{1,2} · André Fujita² · Matheus Rolim Sales³ · José D. Szezech Jr⁴ · Antonio Marcos Batista⁴

Received: 16 November 2021 / Accepted: 14 February 2022 / Published online: 12 March 2022
 © The Author(s) under exclusive licence to Sociedade Brasileira de Física 2022

Abstract

In this paper, we introduce a billiard whose boundary varies from a circular to a polygonal billiard. To describe the billiard boundary, we use a parametric equation, which needs to be solved numerically. We provide a detailed explanation about how to obtain the radius of the billiard boundary R for each angular position θ , where we used a tangent method to speed up the numerical simulations. We consider another tangent method to find the billiard boundary's intercept and the particle's trajectory. Furthermore, we show some trajectories' examples and describe what happens with the phase space and Lyapunov exponents when changing the deformation. We present results for different values of the control parameter related to the number of edges of our polygon and the billiard with a triangular-like boundary.

Keywords Nonlinear dynamics · Chaos · Billiard systems · Chaotic system

6. F. Teston, A. L. Azevedo, **M. R. Sales**, F. M. Zanetti, and M. G. E. da Luz, “The flexibility in choosing distinct green's functions for the boundary wall method: waveguides and billiards,” *Journal of Physics A: Mathematical and Theoretical*, vol. 55, no. 17, p. 175201, 2022.

IOP Publishing

Journal of Physics A: Mathematical and Theoretical

J. Phys. A: Math. Theor. 55 (2022) 175201 (23pp)

<https://doi.org/10.1088/1751-8121/ac5b90>

The flexibility in choosing distinct Green's functions for the boundary wall method: waveguides and billiards

F Teston^{1,3}, A L Azevedo^{1,3} , M R Sales^{1,2} ,
 F M Zanetti¹ and M G E da Luz^{1,*}

¹ Departamento de Física, Universidade Federal do Paraná, Curitiba-PR, 81531-980, Brazil

² Departamento de Física, Universidade Estadual de Ponta Grossa, Ponta Grossa-PR, 84030-900, Brazil

E-mail: luz@fisica.ufpr.br

Received 2 August 2021, revised 24 February 2022

Accepted for publication 8 March 2022

Published 4 April 2022



Abstract

The boundary wall method (BWM) is a general purpose protocol to treat boundary value problems for wave equations, specially Helmholtz's (the case addressed here). Similarly to most approaches, the BWM may be computationally demanding for large borders \mathcal{C} , at which the wave function must satisfy specified boundary conditions. Also, despite the fact the BWM is an exact procedure, usually it is not amenable to closed form solutions. The BWM relies on the Green's function G_0 of the embedding domain V of \mathcal{C} . However, in many instances—like for \mathcal{C} modeling a billiard—the specific V is not really fundamental and thus one has a certain freedom to choose distinct domains and so G_0 's. Here we consider this characteristic of the BWM and show how to obtain some analytical results and solve numerically semi-infinite waveguides by exploring proper Green's functions. As examples, we discuss rectangular, triangular and trapezoidal structures with both Dirichlet and leaking boundaries as well as scattering states within semi-infinite rectangular waveguides.

Keywords: boundary wall method, wave equation, Green's function, quantum billiards, leaking borders

7. M. Mugnaine, **M. R. Sales**, J. D. Szezech Jr, and R. L. Viana, “Dynamics, multistability, and crisis analysis of a sine-circle nontwist map,” *Physical Review E*, vol. 106, p. 034203, 2022.

PHYSICAL REVIEW E 106, 034203 (2022)


Dynamics, multistability, and crisis analysis of a sine-circle nontwist map

Michele Mugnaine 

Department of Physics, Federal University of Paraná, 80060-000 Curitiba, PR, Brazil

Matheus Rolim Sales 

Graduate Program in Science – Physics, State University of Ponta Grossa, 84030-900 Ponta Grossa, PR, Brazil

José Danilo Szezech, Jr. 

Graduate Program in Science – Physics, State University of Ponta Grossa, 84030-900 Ponta Grossa, PR, Brazil
and Department of Mathematics and Statistics, State University of Ponta Grossa, 84030-900 Ponta Grossa, PR, Brazil

Ricardo Luiz Viana 

Department of Physics, Federal University of Paraná, 80060-000 Curitiba, PR, Brazil
and Institute of Physics, University of São Paulo, 05508-900 São Paulo, SP, Brazil

 (Received 6 May 2022; accepted 3 August 2022; published 6 September 2022)

We propose a one-dimensional dynamical system, the sine-circle nontwist map, that can be considered a local approximation of the standard nontwist map and an extension of the paradigmatic sine-circle map. The map depends on three parameters, exhibiting a simple mathematical form but with a rich dynamical behavior. We identify periodic, quasiperiodic, and chaotic solutions for different parameter sets with the Lyapunov exponent and Slater’s theorem. From the bifurcation analysis, we determine two bifurcation lines, those that depend on just two of the control parameters, for which the bifurcation that occurs is of the saddle-node type. In order to investigate multistability, we analyze the bifurcation diagrams in the two directions of parameter variation and we observe some regions of hysteresis, representing the coexistence of different attractors. We also analyze different multistable scenarios, as single attractor, coexistence of periodic attractors, coexistence of chaotic and periodic attractors, chaotic behavior, and coexistence of different chaotic bands, by the Lyapunov exponent and the analysis of the domain occupied by the solutions. From the parameter spaces constructed, we observe the prevalence of single attractor and only chaotic behavior scenarios. The multistable scenario is, mostly, formed by different periodic attractors. Lastly, we analyze the crisis in chaotic attractors and we identify the interior and the boundary crisis. From our results, the boundary crisis plays a key role for the extinction of multistability.

DOI: 10.1103/PhysRevE.106.034203

8. V. dos Santos, **M. R. Sales**, S. S. Muni, J. D. Szezech Jr, A. M. Batista, S. Yanchuk, and J. Kurths, “Identification of single- and double-well coherence–incoherence patterns by the binary distance matrix,” *Communications in Nonlinear Science and Numerical Simulation*, vol. 125, p. 107390, 2023.



Research paper

Identification of single- and double-well coherence–incoherence patterns by the binary distance matrix



Vagner dos Santos ^{a,b}, Matheus Rolim Sales ^{c,d,e}, Sishu Shankar Muni ^f, José Danilo Szezech Jr. ^{a,c,g}, Antonio Marcos Batista ^{a,c}, Serhiy Yanchuk ^{d,e}, Jürgen Kurths ^{d,g,h}

^a Department of Mathematics and Statistics, State University of Ponta Grossa, 84030-900, Ponta Grossa, PR, Brazil

^b Ciências Exatas, Naturais e Engenharias, Centro Universitário UNIFATEB, 84266-010, Telêmaco Borba, PR, Brazil

^c Graduate Program in Sciences/Physics, State University of Ponta Grossa, 84030-900, Ponta Grossa, PR, Brazil

^d Potsdam Institute for Climate Impact Research, Member of the Leibniz Association, P.O. Box 6012 03, D-14412 Potsdam, Germany

^e Institute of Mathematics, Humboldt University Berlin, 12489 Berlin, Germany

^f Department of Physical Sciences, Indian Institute of Science Education and Research Kolkata, Mohanpur, West Bengal, 741246, India

^g Institute of Physics, Humboldt University Berlin, 10099 Berlin, Germany

^h Division of Dynamics, Lodz University of Technology, Stefanowskiego 1/15, 90-924 Lodz, Poland

ARTICLE INFO

Article history:
Received 27 December 2022
Received in revised form 30 April 2023
Accepted 20 June 2023
Available online 25 June 2023

Keywords:
Chua circuit
Basin of attraction
Ring-star network
Coherence–incoherence
Single- and double-well dynamics

ABSTRACT

The study of chimera states or, more generally, coherence–incoherence patterns has led to the development of several tools for their identification and characterization. In this work, we extend the eigenvalue decomposition method to distinguish between single-well (SW) and double-well (DW) patterns. By applying our method, we are able to identify the following four types of dynamical patterns in a ring of nonlocally coupled Chua circuits and nonlocally coupled cubic maps: SW cluster, SW coherence–incoherence pattern, DW cluster, and DW coherence–incoherence. In a ring-star network of Chua circuits, we investigate the influence of adding a central node on the spatio-temporal patterns. Our results show that increasing the coupling with the central node favors the occurrence of SW coherence–incoherence states. We observe that the boundaries of the attraction basins resemble fractal and riddled structures.

© 2023 Elsevier B.V. All rights reserved.

9. E. C. Gabrick, **M. R. Sales**, E. Sayari, J. Trobia, E. K. Lenzi, F. S. Borges, J. D. Szezech Jr, K. C. Iarosz, R. L. Viana, I. L. Caldas, A. M. Batista, “Fractional dynamics and recurrence analysis in cancer model,” *Brazilian Journal of Physics*, vol. 53, p. 145, 2023.

Brazilian Journal of Physics (2023) 53:145
<https://doi.org/10.1007/s13538-023-01359-w>



GENERAL AND APPLIED PHYSICS



Fractional Dynamics and Recurrence Analysis in Cancer Model

Enrique C. Gabrick¹ · Matheus R. Sales¹ · Elaheh Sayari¹ · José Trobia² · Ervin K. Lenzi^{1,3} · Fernando S. Borges⁴ · José D. Szezech Jr.^{1,2} · Kelly C. Iarosz^{1,5,6} · Ricardo L. Viana^{6,7} · Iberê L. Caldas⁷ · Antonio M. Batista^{1,2,7}

Received: 21 July 2023 / Accepted: 22 August 2023
 © The Author(s) under exclusive licence to Sociedade Brasileira de Física 2023

Abstract

In this work, we analyze the effects of fractional derivatives in the chaotic dynamics of a cancer model. We begin by studying the dynamics of a standard model, i.e., with integer derivatives. We study the dynamical behavior by means of the bifurcation diagram, Lyapunov exponents, and recurrence quantification analysis (RQA), such as the recurrence rate (RR), the determinism (DET), and the recurrence time entropy (RTE). We find a high correlation coefficient between the Lyapunov exponents and RTE. Our simulations suggest that the tumor growth parameter (ρ_1) is associated with a chaotic regime. Our results suggest a high correlation between the largest Lyapunov exponents and RTE. After understanding the dynamics of the model in the standard formulation, we extend our results by considering fractional operators. We fix the parameters in the chaotic regime and investigate the effects of the fractional order. We demonstrate how fractional dynamics can be properly characterized using RQA measures, which offer the advantage of not requiring knowledge of the fractional Jacobian matrix. We find that the chaotic motion is suppressed as α decreases, and the system becomes periodic for $\alpha \lesssim 0.9966$. We observe limit cycles for $\alpha \in (0.9966, 0.899)$ and fixed points for $\alpha < 0.899$. The fixed point is determined analytically for the considered parameters. Finally, we discover that these dynamics are separated by an exponential relationship between α and ρ_1 . Also, the transition depends on a super transient which obeys the same relationship.

Keywords Cancer model · Fractional calculus · Recurrence analysis

Items 2 and 3 correspond to the results presented in Chapters 4 and 5, respectively. Some of the results presented in Chapter 6 correspond to the results of item 5. Item 8 corresponds to my interuniversity exchange doctorate project (Programa de Doutorado Sanduíche no Exterior). Vagner and Sishu came up with the idea, and they asked for my help with the simulations. Together with Serhiy and Jürgen, both from Humboldt Universität zu Berlin and Potsdam Institute für Klimafolgenforschung, we extended the method for coherence–incoherence detection proposed by Parastesh *et al.* ([10.1209/0295-5075/130/28003](https://doi.org/10.1209/0295-5075/130/28003)), and showed that by employing this methodology we can identify different dynamical patterns in a network of coupled systems.